QUANTUM THERMODYNAMICS, SPINTRONICS AND ZERO MODE STATISTICS IN TOPOLOGICAL MATTER

by

AHMET MERT BOZKURT

Submitted to the Graduate School of Engineering and Natural Sciences
in partial fulfillment of
the requirements for the degree of
Doctor of Philosophy

Sabancı University

July 2021

QUANTUM THERMODYNAMICS, SPINTRONICS AND ZERO MODE STATISTICS IN TOPOLOGICAL MATTER

Approved by:

Date of Approval: July 1, 2021

ABSTRACT

QUANTUM THERMODYNAMICS, SPINTRONICS AND ZERO MODE STATISTICS IN TOPOLOGICAL MATTER

AHMET MERT BOZKURT

Physics Ph.D Dissertation, July 2021

Dissertation Supervisor: Prof. Dr. İnanç Adagideli

Keywords:Topological insulators and superconductors, Maxwell's demon, spintronics, Landauer's erasure principle, memristor, quantum thermodynamics, Majorana fermions, random matrix theory

The aim of this thesis is to explore the charge and spin dynamics in topological systems from the point of view of quantum thermodynamics, spintronics and quantum chaos. In particular, we propose and investigate a novel way of implementing Maxwell's demon engines by using topological systems that feature spin-momentum locking. As a memory resource for Maxwell's demon, we utilize a "spin bath" that usually includes the nuclear spins which are naturally present in the device and/or magnetic impurities introduced via doping. The significance of this Maxwell's demon implementation is its scalability of the memory size. We introduce two novel Maxwell's demon implementations on two different setups. The first setup is a quantum spin Hall insulator in the presence of nuclear spins, which we call a quantum information engine, alluding to conversion of information entropy of the Maxwell's demon memory into usable free energy. We investigate heat and charge transport in a quantum information engine and describe the protocol for memory erasure and work extraction. The second setup is a hybrid system, composed of a quantum spin Hall insulator connected to two quantum anomalous Hall insulators with different spins and chiralities. The distinctive feature of this setup is that it not only operates at the Landauer's limit, providing higher efficiency and denser energy storage capability at weak couplings, but it also provides additional functionality via its memristive response. Furthermore, we extend the discussion to three dimensional topological insulators, featuring spin-momentum locked surface states that allow dissipative nonmagnetic impurity scattering. Finally, we study the spectra of fermion-parity switches in topological superconductors that host Majorana zero modes from the perspective of spectral geometry and random matrix theory and show that these spectra depend on the geometrical shape of the topological superconductor and can distinguish chaotic shapes from integrable shapes.

ÖZET

TOPOLOJİK MALZEMELERDE KUANTUM TERMODİNAMİK VE SPİNTRONİK UYGULAMALAR VE SIFIR MOD İSTATİSTİĞİ

AHMET MERT BOZKURT

Fizik Doktora Tezi, Temmuz 2021

Tez Danışmanı: Prof. Dr. İnanç Adagideli

Anahtar Kelimeler: Topolojik yalıtkan ve süperiletkenler, Maxwell'in cini, spintronik, Landauer prensibi, memristör, kuantum termodinamiği, Majorana fermiyonu, rastlantısal matris kuramı

Bu tezin amacı, topolojik sistemlerde yük ve spin dinamiklerini, kuantum termodinamik ve spintronik uygulamalar ve kuantum kaos açısından incelemektir. Özellikle, spin-momentum kilitleme özelliğine sahip topolojik sistemleri kullanarak Maxwell'in cini temelli motor uygulamaları için yeni bir yol öneriyoruz. Maxwell'in cini için hafıza kaynağı olarak, genellikle cihazda doğal olarak bulunan nükleer spinleri ve/veya katkılama yoluyla yerleştirilebilen manyetik safsızlık spinleri içeren bir "spin sistemi" kullanıyoruz. Bu Maxwell'in cini uygulamasının önemi, hafıza boyutunun ölçeklenebilirliğidir. İki farklı sistemde iki yeni Maxwell'in cini uygulamasını tanıtıyoruz. İlk sistem, Maxwell'in cini hafızasının sahip olduğu bilgi entropisinin kullanılabilir serbest enerjiye dönüştürülmesini ima eden kuantum bilgi motoru dediğimiz, nükleer spinlerin varlığında bir kuantum spin Hall yalıtkanıdır. Kuantum bilgi motorunda ısı ve yük aktarımını araştırıyor ve hafıza silme ve iş çıkarma protokolünü açıklıyoruz. Örgülü kuantum bilgi motoru dediğimiz ikinci sistem ise, farklı spin ve kiralitelere sahip iki kuantum anormal Hall yalıtkanına bağlı bir kuantum spin Hall yalıtkanından oluşan karma bir sistemdir. Bu sistemin kendine has özelliği, yalnızca Landauer'in sınırında çalışması ve bunun sayesinde daha yüksek verimlilik ve daha yoğun enerji depolama kapasitesi sağlaması değil, aynı zamanda ideal bir memristör olarak ek işlevsellik sunmasıdır. Bundan sonra tartışmayı, manyetik olmayan safsızlık saçılmasından kaynaklı enerji kaybına yol açabilen, spin-momentum kilitli yüzey durumları içeren üç boyutlu topolojik yalıtkanlara genişletiyoruz. Son olarak, Majorana sıfır modlarını barındıran topolojik süperiletkenlerin fermiyon-parite geçişlerinin tayfını, tayfsal geometri ve rastlantısal matris kuramı açısından inceliyoruz ve bu tayfın, topolojik süperiletkenin şekline bağlı olduğunu ve yine bu tayfın, kaotik şekilleri tümlevlenebilir şekillerden ayırt edebildiğini buluyoruz.

ACKNOWLEDGEMENTS

I am deeply grateful to my advisor Prof. İnanç Adagideli, who welcomed me to his group when I decided to move back to Turkey. His guidance, support and patience encouraged me to carry on through the course of my PhD. It was my privilege to work with him.

I would like to extend my deepest gratitude to my thesis committee members, Prof. Mehmet Zafer Gedik, Prof. Burç Mısırlıoğlu, Prof. Özgür Esat Müstecaplıoğlu and Prof. Alexander Brinkman for their kind help and encouragement. Through their suggestions and recommendations, they helped me immensely in the writing of this thesis.

Special thanks to my colleague and friend Dr. Barış Pekerten with whom I enjoyed working during the course of my PhD. The insightful discussions we had and his invaluable assistance helped me greatly with the completion of this thesis. I also would like to thank my colleague Dr. Ali Asgharpour and my office mates Ali Murtaza Altıngün and Bilal Cantürk for their support and help. The discussions we had during the course of the pandemic kept me going whenever I felt tired.

Most of the work presented in this thesis had been written at the office of The Science Academy (Bilim Akademisi), Turkey. I would like to thank The Science Academy and Prof. Mehmet Ali Alpar for letting me use their facilities and for providing me a perfect working environment. I am also indebted to Defne Üçer Şaylan, Maral Yağyazan and Yaprak Özışık from Bilim Akademisi for their amazing hospitality.

I would like to declare my deep love for my family for their love and support. I am indebted to my dear wife, İrem, for standing by me through all my highs and lows. Without your love and support, I couldn't have completed this thesis.

I acknowledge financial support from the Erdal İnönü Chair and a Lockheed Martin Corporation Research Grant.

TABLE OF CONTENTS

LIST OF TABLES

LIST OF FIGURES

Chapter 1

INTRODUCTION

The purpose of this thesis is to explore charge and spin dynamics in topological systems from the point of view of quantum thermodynamics and quantum transport and quantum chaos. In particular, in the setting of quantum thermodynamics and quantum transport, we focus on the quantum coherent topological insulators in different dimensions and transport regimes as platforms for Maxwell's demon engine implementation and discuss the physics of Landauer's erasure principle in each case. In the setting of quantum chaos, we investigate the statistics of the ground state fermion parity switches in topological superconductors from the perspective of spectral geometry and random matrix theory.

This thesis is organized as follows: In Chapter 2, we briefly introduce the physics of Maxwell's demon and Landauer's erasure principle. In Chapter 3, we present a new Maxwell's demon implementation using a quantum spin Hall insulator and nuclear spins, which we call an inductive quantum information engine [1, 2]. We investigate the charging/discharging cycle of the inductive quantum information engine and derive the corresponding amount of heat dissipation/work extraction. Furthermore, we explore the inductive quantum information engine under AC and DC voltage bias. We conclude this chapter with possible candidate materials for experimental realization of our proposed model. In Chapter 4, we introduce a second Maxwell's demon implementation that is capable of operating at the Landauer's limit in a mesoscopic platform composed of quantum anomalous Hall insulators and quantum spin Hall insulators. In this model, it is possible to erase Maxwell's demon memory by a minimum amount of heat dissipation, which is set by the Landauer's principle. Moreover, we show that all the stored energy in the memory can be extracted in the form of electrical work. We also demonstrate that this second quantum information engine is an ideal memristor. In Chapter 5, we consider three dimensional topological insulators as a platform for Maxwell's demon implementations. We treat ballistic and diffusive regimes separately and derive the diffusion equation for the surface

states interacting with the nuclear spins. We then change course from the thermodynamic applications to topological superconductivity and Majorana billiards. We briefly introduce the topological superconductors in Chapter 6. In Chapter 7, we study the fermion parity crossings in arbitrarily shaped Majorana billiards within the framework of spectral geometry, semiclassical physics and random matrix theory [3]. We utilize Weyl expansion and find that the geometrical shape of the Majorana billiard is related to the average density of parity crossings. We then investigate the dynamics of Majorana billiards and show that oscillations around the average density of fermion parity crossings are associated with the periodic orbits. Moreover, we show that the statistics of the fermion parity crossing spacings in Majorana billiards is universal and the universality class depends on whether the corresponding normal state system is regular, diffusive, chaotic or localized. In Chapter 8, we make our concluding remarks on the works presented in this thesis.

Chapter 2

INTRODUCTION TO THE PHYSICS OF MAXWELL'S DEMON

In this chapter, we briefly introduce quantum heat engines from the viewpoint of information thermodynamics. In particular, we focus on quantum heat engines known as Maxwell's demon engines, that utilize the equivalence between the information entropy and thermodynamic entropy. For a more comprehensive discussion on the physics and applications of Maxwell's demon, we direct the reader to review Ref. [4] and the references within.

Originally proposed in 1871 by James Clerk Maxwell [5], Maxwell's demon is a hypothetical intelligent agent, designed to challenge the second law of thermodynamics. In Maxwell's thought experiment, a box is divided into two chambers at equal volume and at equal temperature. The barrier that divides the box into two chambers contains a small door that is controlled by the demon. The demon observes the particles and opens the door only to allow for faster particles to enter one of the chambers while the slower particles are only allowed to pass on to the other chamber. This operation leads to a temperature increase for one chamber and decrease for the other chamber, hence generating a temperature gradient that can be used to extract work. In other words, the entropy of the overall system decreases, in violation with the second law of thermodynamics.

In 1929, Leo Szilard reformulated the original setup using a single molecule in equilibrium with a thermal bath, trapped in a box [6]. In this formulation, a piston that is free to move left or right is inserted in the box in such a way that the box is divided into two parts. Then, the demon observes the position of the molecule and determines which side (left or right) it is on. Based on this information, the demon attaches a weight to the piston and using the expansion of the molecule, the demon is able to extract work with a maximum

amount of $k_B T \ln 2$.

The Szilard's engine appears to be in contradiction with the second law of thermodynamics, which forbids the extraction of positive work in a thermodynamic cycle while in contact with a single heat bath. The resolution of this apparent violation of the second law of thermodynamics came with the Landauer's erasure principle [7]. Originally introduced for the thermodynamic cost of computation, this principle states that erasing a bit of information is an irreversible process that requires heat dissipation by at least an amount of $k_B T \ln 2$ and a corresponding entropy increase by $k_B \ln 2$. Landauer's erasure principle translates into the Maxwell's demon as follows: the Maxwell's demon also represents a physical system, which requires a memory for the operation. Hence, the demon's memory also needs to be reset in order to be reused. The conclusion is that the energy that can be extracted from a system using a single bit of information can never exceed the amount energy needed to reset the memory, obeying a generalized form of the second law of thermodynamics which includes also information entropy. In the language of information thermodynamics, Szilard's engine is an example of how information entropy of the demon's memory can be converted into free energy which can be utilized to extract work.

Apart from a fundamental physics point of view [8–13], the Maxwell's demon and the Landauer's principle found application avenues in mesoscopic and nano-scale quantum devices [14–16] as an alternative way of devising quantum heat engines, with the promise of improved efficiency compared to their classical counterparts. New platforms for implementing Maxwell's demon engines in quantum systems were proposed [17–35] and various experimental demonstrations followed shortly. There is a broad range of experimental platforms on which the Maxwell's demon effect was demonstrated, such as colloidal particles [36–38], photonics and cold atom systems [39, 40], NMR systems [41, 42], single electron transistors [43–46], cavity QED with superconducting qubits [47].

In the following three chapters, we explore a complete platform, namely topological insulators, for implementing Maxwell's demon. We propose that nuclear spins and/or magnetic impurities in quantum spin Hall insulators, quantum anomalous Hall insulators and three dimensional topological insulators can be utilized as a memory resource of a Maxwell's demon setup that harvests thermal energy from the electronic environment and converts it to electrical work. The possibility of using nuclear spins as a memory resource not only allows for orders of magnitude larger memory sizes in comparison with the other platforms where the physics of Maxwell's demon was investigated, but also allows us to investigate the physics of Maxwell's demon and Landauer's erasure principle in a system where the memory size can be statistically significant. Moreover, the dramatic increase in the Maxwell's demon memory size makes these systems technologically useful and appealing for battery/engine applications that require high energy and power densities.

Chapter 3

MAXWELL'S DEMON IN A QUANTUM SPIN HALL INSULATOR: AN INDUCTIVE QUANTUM INFORMATION ENGINE

In this chapter, we propose and investigate a new Maxwell's demon implementation that is capable of converting thermal energy of the electronic environment into usable electrical work using a quantum spin Hall insulator. We mainly focus on heat and charge transport in a quantum spin Hall insulator that is in contact with a spin bath, which we utilize as the memory. Our choice of memory resource is the already available nuclear spins in the device and/or magnetic impurity spins introduced via doping. We show how to utilize the spin bath as a Maxwell's demon memory and design a heat engine/battery, which we call a *quantum information engine*. We demonstrate the charging/discharging cycle of the quantum information engine and derive the corresponding amount of heat dissipation/work extraction. We further investigate the quantum information engine as a circuit element and calculate both DC and AC behavior. Lastly, we examine the possible experimental platforms for our quantum information engine and compare available materials in terms of energy density/power density capabilities.

This chapter is organized as follows: First, we first specify the system we consider, namely a two-dimensional topological insulator in the presence of nuclear spins/magnetic impurities in Section 3.1. In Section 3.2, we describe the working principle of the quantum information engine. We derive the current-voltage characteristics and calculate the generated power and extracted work by the quantum information engine in the short edge limit. We consider the work extraction via an external load. In Section 3.3, we consider

the long edge limit and find that the generated power and extracted work are limited by their respective bounds. We obtain the current response of our inductive quantum information engine under a low-frequency AC applied voltage bias in Section 3.4. We also derive the effective inductance of the quantum information engine. We distinguish the quantum information engine implementation presented in this chapter from our second implementation presented in Chapter 4 by its AC response, hence we interchangeably call this implementation inductive quantum information engine. In Section 3.5, we investigate several candidate materials for the implementation of quantum information engine and compare their characteristic time scales and open circuit voltage values. Finally, we give a brief conclusion in Section 3.6

3.1 Quantum Information Engine

In this section, we show how to utilize the backscattering of helical edge states of the quantum spin Hall insulators from the nuclear spins and demonstrate that (i) an initial state of polarized nuclear spins (blank memory) induces a charge current in the system by converting the ambient heat in the reservoirs into extractable electrical work, reminiscent of a memory resource of a Maxwell's demon and (ii) a minimum heat dissipation is required to achieve such state of polarized nuclear spins (erasing the memory), in agreement with the second law of thermodynamics and Landauer's bound. We note that the nuclear spin subsystem is degenerate, as there is no external magnetic field. Hence, the nuclear spins constitute a non-energetic memory. As a result, no energy transfer between helical edge states and memory is required.

We further note that the size of the Maxwell's demon memory is determined by the number of nuclear spins and magnetic impurities. Each nuclear spin has a nonzero coupling to the electron spins at the edges of a quantum spin Hall insulator. Therefore, the memory capacity of our implementation can be substantially larger in contrast to the proposed Maxwell's demon implementations in the literature [17–32].

As it is beneficial to understand the working principle of the quantum information engine, we first describe the constituents of the quantum information engine, namely the quantum spin Hall insulator and the hyperfine interaction of nuclear spins. We obtain the effective Hamiltonian describing the overall Maxwell's demon effect and then present the demon protocol.

3.1.1 Quantum Spin Hall Insulator and Helical Edge States

Quantum spin Hall insulators are materials that exhibit a bulk band gap and gapless helical edge states with spin-momentum locking. Over the last decade, this unique topological state of matter was experimentally demonstrated in HgTe/CdTe semiconductor heterostructures [48, 49], in InAs/GaSb quantum wells [50, 51] and in WTe_2 monolayer structures [52, 53]. As quantum spin Hall insulators are invariant under time-reversal symmetry, backscattering of the helical edge states due to time-reversal invariant perturbations is prohibited [54]. However, this topological protection against backscattering of the helical edge states is lifted in the presence of nuclear spins or magnetic impurity spins, which break the time-reversal symmetry enjoyed by the electrons and holes in the system. Hence, the predicted quantized conductance of the ballistic helical edge states is lowered due to backscattering, which leads to an additional dissipation of energy [55–59].

We start with a model of a band insulator with two atomic orbitals with different parities and two spin species. In the inverted band regime, this Hamiltonian, namely the Bernevig-Hughes-Zhang (BHZ) Hamiltonian [49], describes the dynamics of helical edge states:

$$\mathcal{H}_{\text{BHZ}} = \epsilon_k \, \sigma_0 \tau_z + E_k \, \sigma_0 \tau_0 + A \, (k_x \, \sigma_z \tau_x - k_y \, \sigma_0 \tau_y), \tag{3.1}$$

where $\epsilon_k = M - Bk^2$, $E_k = C - Dk^2$ and M, A, B, C, D are the material parameters. The BHZ Hamiltonian above is given in orbital-spin basis: $(\psi_{+,s}, \psi_{-,s}, \psi_{+,p}, \psi_{-,p})^T$, where $\sigma = \pm$ denote the spin, $\tau = s, p$ denote the atomic orbitals with different parities, $s-$ and $p-$ orbitals. σ_α and τ_α ($i \in \{x, y, z\}$) are the Pauli matrices that operate in spin and atomic orbital degrees of freedom, respectively. (We also define the corresponding unit matrices σ_0 and τ_0.) We note that this generalized model offers a description of numerous possible quantum spin Hall insulator candidate materials. These materials differ only in their effective parameters [60], but the existence of helical edge states is unchanged.

The full wavefunction that incorporates the lattice periodic functions is necessary to define the interaction between the nuclear and electron spins [61]:

$$\Psi(\vec{r}) = \sum_{\sigma,\tau} \psi_{\sigma,\tau}(\vec{r}) u_{\sigma,\tau}(\vec{r}). \tag{3.2}$$

We now obtain the low energy excitations in the topological phase. These excitations within the bulk band gap are localized at the edges of the quantum spin Hall insulator:

$$\psi^{\rightleftharpoons}_{\sigma,\tau}(\vec{r}) = \xi(\vec{r}_\perp) \phi^{\rightleftharpoons}(x), \tag{3.3}$$

where the superscript $\rightleftharpoons$ denotes these helical edge states of different chiralities. For a

system with no spin-orbit coupling, the chiral state also defines the spin state of the edge states, hence we have $\psi^{\rightleftharpoons}_{\sigma,\tau} \propto \delta_{=,\sigma}$. (A position dependent spin axes description is used for systems with spin-orbit coupling [62].)

Using the low-energy projected edge states given in Eq. 3.3, we obtain the effective Hamiltonian for the edge states:

$$H^{\text{eff}}_{\text{bot(top)}} = \mp i\,\hbar v_F \partial_x \sigma_z, \tag{3.4}$$

where, v_F is the Fermi velocity of the helical edge states (a material-dependent parameter) and $\mp$ signs indicates the edges; + for the top edge and the - for the bottom edge (see Fig. 3.1b). For a given edge, the two counterpropagating helical edge states are time-reversal symmetric partners (Kramers pair). In our model, we assume that the z-axis of the total spin is conserved, hence two Kramers partners have opposite spin.

3.1.2 Nuclear Spins and Hyperfine Interaction

Nuclear spins and magnetic impurities in the quantum spin Hall insulators interact with the spins of the helical edge states. The interaction strength is different for electrons with $s-$ and $p-$ orbitals, with the former having a coupling stronger [63]. Thus, we only consider the interaction between the spins of the nuclei and the spins of the helical edge states is given by the Fermi contact hyperfine interaction, which is the dominant source of hyperfine interaction for the $s-$ orbital electrons:

$$H_{\text{hf}} = v_0 \sum_{i=1}^{N} A_i \delta(\vec{r} - \vec{R}_i)\vec{I}_i \cdot \vec{\sigma}, \tag{3.5}$$

where $\vec{\sigma}$ is the vector of Pauli matrices with electron spin operators, v_0 is the volume of the unit cell of a given quantum spin Hall insulator material, $\vec{I}_i$ is the nuclear spin operator at position $\vec{R}_i$ and A_i is the hyperfine interaction strength for the i^{th} nuclear spin. As the hyperfine interaction given in Eq. (3.5) is for $s-$ orbitals, the only relevant nuclear spins are along the edges of the quantum spin Hall insulator. The remaining nuclear spins in the bulk does not contribute to the Maxwell's demon memory as they do not interact with the helical edge states directly. Therefore, we find it useful to project the hyperfine interaction to the edge of the system and obtain the total effective Hamiltonian, including Eq. (3.4), describing the overall system (see Appendix B for a detailed derivation)

$$H_{\text{bot(top)}} = \big(\mp i\hbar v_F \partial_x + \lambda M_z(x) \big)\sigma_z$$

$$H_{\text{s-flip}} = \sum_{i=1}^{N} \frac{\lambda_i}{2} \delta(x - x_i)\big(I_{i+}\sigma_- + I_{i-}\sigma_+\big), \tag{3.6}$$

where x indicates projected one-dimensional position for a given edge. In practice, the the wavefunctions associated with the helical edge states spread in transverse directions, forming a cross-section, which we denote as S, in which the helical edge states interact with the available nuclear spins. Hence, the projection includes only those nuclear spins that are along the edge and within the cross-section. For ease of calculation, we assume that the site-dependent effective coupling $\lambda_i = \lambda = A_0 v_0/S$, where A_0 is the average value of A_i, is constant for all nuclear spins. This assumption does not change the operating principle of our model. In anticipation of dynamically polarized nuclear states that we consider below, also introduce, $M_z(x)$ as the Overhauser field [63], which we gauge away via gauge transformation $H_{\text{bot(top)}} \to U H_{\text{bot(top)}} U^\dagger$ with $U = \exp\left(\frac{\pm i\lambda}{\hbar v_F} \int^x M_z(x')dx'\right)$. We emphasize that this Overhauser field does not cause any gap to open in the helical edge state spectrum.

As any coupling between nuclear spins is undesirable, temperature of the system must be higher than the critical temperature T^*, below which Ruderman-Kittel-Kasuya-Yosida and other nuclear correlation effects become important [64]. This critical temperature T^* is estimated to be less than 100 mK [59]. Furthermore, the dipolar coupling between the nuclear spins may lead to loss of nuclear polarization or suppress the dynamical nuclear spin polarization. However, the Knight field induced by the helical edge states is strong enough, which ensures that the dipolar coupling is suppressed [65]. Lastly, the quadrupole interaction between nuclear spins can also be a source of decoherence, however the energy scales in which this interaction is effective is much smaller than the Fermi contact interaction between nuclear spins and electron spins [66].

3.2 Demon Protocol of the Quantum Information Engine

In this section, we illustrate the working principle of the inductive quantum information engine. We distinguish two phases of operation, namely the charging (erasure) and discharging (or work extraction) phases. As a consequence of the spin-momentum locking of the helical edge states, any spin-flip process in which the spin of one nuclear spin and the spin of the helical edge states are flipped due to $H_{\text{s-flip}}$, results in backscattering of electrons (see Fig. 3.1d).

We first describe the charging phase. Without loss of generality, we focus on the bottom edge. We consider the case where the left movers are spin down electrons and the

right movers are spin up electrons. Hence, when we apply a charge current, which we take to be flowing left, there are more spin up electrons than spin down electrons. As a result, there is more right to left backscattering due to spin-flip scattering, whilst this backscattering process flips the nuclear spins from down to up, generating a finite amount of up nuclear spin polarization. The generalization to the top edge is straightforward; a left moving charge current generates down spin polarization, opposite of the bottom edge (see Fig. 3.2b). This mechanism is known as dynamic nuclear spin polarization, where a nonequilibrium electron spin polarization is transferred to the nuclear spins and leading to alignment of the nuclear spins along the electron spin polarization [67, 68]. We show below that an applied voltage bias polarizes the nuclear spins with a target polarization that depends on the ratio of applied voltage bias and temperature [55, 57].

In the work extraction phase, we show that polarized nuclear spins/magnetic impurities induce a charge current along the edges of a quantum spin Hall insulator (see Fig. 3.2c). This current can then be utilized to extract electrical work via a load or an applied reverse bias. In other words, the information entropy of the nuclear spin subsystem is converted into useful work, in the spirit of Maxwell's demon. A polarized nuclear spin subsystem is in a lower entropy state and tends to increase its entropy via depolarization in the absence of temperature gradient or voltage bias. As we discussed above, the dominant interaction for nuclear spins is with the electron spins, so the depolarization of the nuclear spins is achieved via spin-flip interaction (Eq. (3.6)) with the helical edge states. Let us consider a nonzero nuclear spin polarization (opposite polarizations for both edges) and first we assume that there is no applied voltage bias or temperature gradient. For a given edge, a finite nuclear spin polarization mostly flips electron spins opposite to the nuclear spin polarization. To exemplify, up(down) nuclear spin polarization in the bottom(top) edge predominantly flips down(up) electron spins to up(down). This results in having more left mover charge carriers than right mover charge carriers. This is the mechanism behind the information entropy induced charge current between reservoirs of equal chemical potential and temperature: As backscattering occurs, the memory of the demon is used to record the event (see Fig. 3.2). Concurrently, this induced current can be harnessed to extract electrical work that harvests heat from the reservoirs, completing the heat engine cycle.

3.2.1 Electron Backscattering and Dynamic Nuclear Spin Polarization

We calculate the backscattering dynamics of the helical edge electrons, characterized by the electron density matrix $\rho(r, r')$. We again consider the bottom edge, with right movers

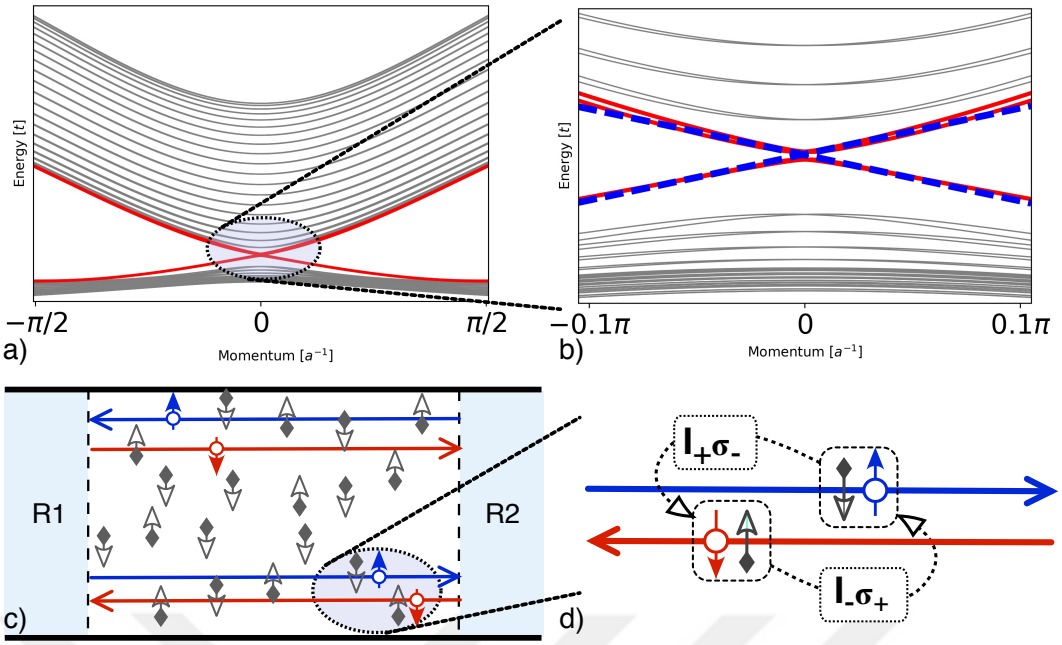

Figure 3.1: Quantum spin Hall insulator with nuclear spins and electron-nuclear spin flip interaction. (a) Dispersion relation of a generic quantum spin Hall insulator for a tight-binding version of the BHZ model. Red lines depict the gapless helical edge states. (b) Dispersion relation for the projected Hamiltonian H_{eff} on a single edge (dashed blue lines). (c) Schematic description of the quantum information engine; the edge states interacting with the nuclear spins (diamonds) in the system. (d) Generic spin-flip interaction with the helical edge states and nuclear spins.

are spin-up electrons and left movers are spin-down electrons. The generalization to the top edge case is as mentioned before. We obtain the rate of backscattering from right to left, with associated flipping of the nuclear spins, between x and $x + \Delta x$ is given by [55, 57]:

$$\Gamma_{-+}(\epsilon, x) = \frac{\gamma_0}{\hbar} N_{\downarrow}(x)\, f_{+}(\epsilon, x)\big(1 - f_{-}(\epsilon, x)\big), \tag{3.7}$$

where $N_{\downarrow}(x)$ is the total number of nuclear down spins between a coarse-grained position x and $x + \Delta x$ (including the cross-section of the helical edge states). We define $\gamma_0 \equiv \lambda^2/8\pi\hbar^2 v_F^2$ as a dimensionless interaction strength, characterizing the spin-flip process between a helical edge state and a single nuclear spin. We further define the distribution functions of the helical edge states for right movers and left movers at energy ϵ at position x is given by $f_{\pm}(\epsilon, x)$ as the Wigner transform of $\rho_{\pm}(r, r')$:

$$f_{\pm}(\epsilon, x) = \int dr \rho_{\pm}(x + r/2, x - r/2) \mathrm{e}^{\pm i\epsilon r/\hbar v_F}. \tag{3.8}$$

Nuclear polarization dynamics

We use the rate equations given in Eq. (F.2) and find the rate of change of number of up nuclear spins as:

$$\frac{dN_{\uparrow}(x)}{dt} = \int d\epsilon \big(\Gamma_{-+}(\epsilon, x) - \Gamma_{+-}(\epsilon, x)\big). \tag{3.9}$$

For ease of calculation, we define the mean polarization $m(x) \equiv \frac{N_{\uparrow}(x)-N_{\downarrow}(x)}{2(N_{\uparrow}(x)+N_{\downarrow}(x))}$ of the nuclear spin subsystem, and obtain its time rate of change as

$$\frac{dm(x)}{dt} = \gamma_0 \Gamma_B(x) - m(x)\gamma_0 \Gamma_T(x) \tag{3.10}$$

with $\hbar\,\Gamma_B(x) = \int d\epsilon \left(f_+(\epsilon, x) - f_-(\epsilon, x)\right)/2$ and $\hbar\,\Gamma_T(x) = \int d\epsilon \left(f_+(\epsilon, x) + f_-(\epsilon, x) - 2f_+(\epsilon, x)f_-(\epsilon, x)\right)$. Here, the subscripts of these terms are chosen such that B stands for the "bias" and T stands from temperature. In this section, we focus on the "short edge", where we ignore the position dependence of the distribution functions $f_{\pm}$ and the mean polarization m. In Section 3.3, we will focus on the "long edge" limit.

In the short edge limit, we approximate the mean polarization as a homogeneous distribution and drop the position dependence. Furthermore, we assume that the distribution functions of the helical edge states are given by the Fermi-Dirac distribution of the respective reservoirs; right movers are in equilibrium with the left reservoir $f_+(\epsilon, x) \approx f_L^0(\epsilon)$ and left movers are in equilibrium with the right reservoir $f_-(\epsilon, x) \approx f_R^0(\epsilon)$ (see Appendix C). Hence, we obtain

$$\begin{aligned} \hbar\Gamma_B &= (\mu_L - \mu_R)/2, \\ \hbar\Gamma_T &= (\mu_L - \mu_R)\coth\left(\frac{\mu_L - \mu_R}{2k_B T}\right), \end{aligned} \tag{3.11}$$

where μ_L and μ_R are the chemical potential of the left and right reservoirs, respectively.

We insert the bias and temperature rates given above into Eq. (3.10) and obtain the mean polarization dynamics as:

$$m(t) = (m_0 - \bar{m})\mathrm{e}^{-t/\tau_m} + \bar{m}, \tag{3.12}$$

where m_0 is the initial mean polarization. As discussed before, the ratio of the applied voltage bias and temperature yields a target mean polarization, which we find to be $\bar{m} \equiv \Gamma_B/\Gamma_T = (1/2)\tanh\left(\frac{\mu_L-\mu_R}{2k_B T}\right)$. Finally, the time scale for nuclear spin polarization/depolarization is given as $\tau_m = 1/\gamma_0\Gamma_T$. The overall nuclear spin polarization of the Maxwell's demon memory can be obtained by multiplying the mean polarization with the total number of nuclear spins.

Maxwell's demon induced current

We next calculate the electron dynamics using the Boltzmann transport equation. We find that the distribution functions obey the following equation:

$$\partial_t f_\pm = \pm\big(\Gamma_{+-}(\epsilon,x) - \Gamma_{-+}(\epsilon,x)\big)\,\nu(0)^{-1} \mp v_F \partial_x f_\pm, \tag{3.13}$$

where $\nu(0) = L/2\pi\hbar v_F$ is the density of states of the helical edge states and L is the length of the quantum information engine. In the steady state regime, in which m is changing gradually, the distribution functions of the helical edge states satisfy:

$$\begin{aligned}\partial_x f_\pm &= \big(\Gamma_{+-}(\epsilon,x) - \Gamma_{-+}(\epsilon,x)\big)\,\big(v_F\nu(0)\big)^{-1} \\ &\equiv \Gamma[f_+, f_-]\end{aligned} \tag{3.14}$$

In the short edge limit ($\Gamma[f_+, f_-]\,L \ll 1$), we replace the distribution functions of the right/left movers with the left/right reservoir Fermi-Dirac distribution functions and expand Γ given in Eq. (3.14) in gradients. We find that to the first nontrivial order, the distribution functions attain a linear dependence on position x:

$$f_\pm(\epsilon) = f^0_{L(R)}(\epsilon) + \Gamma[f^0_L(\epsilon), f^0_R(\epsilon)]\,(x \pm L/2). \tag{3.15}$$

We use these distribution functions to find the current response of a given edge of the quantum information engine (see Appendix C):

$$\begin{aligned} I_{tot} &= \frac{e}{h}\int d\epsilon (f_+(\epsilon) - f_-(\epsilon)) = \frac{e^2}{h}V - eN\gamma_0(\Gamma_B - m\Gamma_T), \\ &= \frac{e^2 V}{h}\left[\big(1 - \pi N\gamma_0\big) + 2\pi N\gamma_0 m \coth\left(\frac{eV}{2k_BT}\right)\right], \end{aligned} \tag{3.16}$$

where V is the applied voltage and T is the temperature. We distinguish two distinct contributions to the total current response of the quantum information engine, given in Eq. (3.16). Firstly, we have the ballistic current response due to the applied voltage $\frac{e^2}{h}V$, which is present irrespective of the nuclear spins. This is the expected contribution which yields quantized conductance e^2/h.

However, the remaining contribution is only present if there are nuclear spins along the edges of the quantum system. We identify this term as the Maxwell's demon induced current term, which has the following form:

$$I_{MD} = -eN\frac{dm}{dt} = -eN\gamma_0\,(\Gamma_B - m\Gamma_T). \tag{3.17}$$

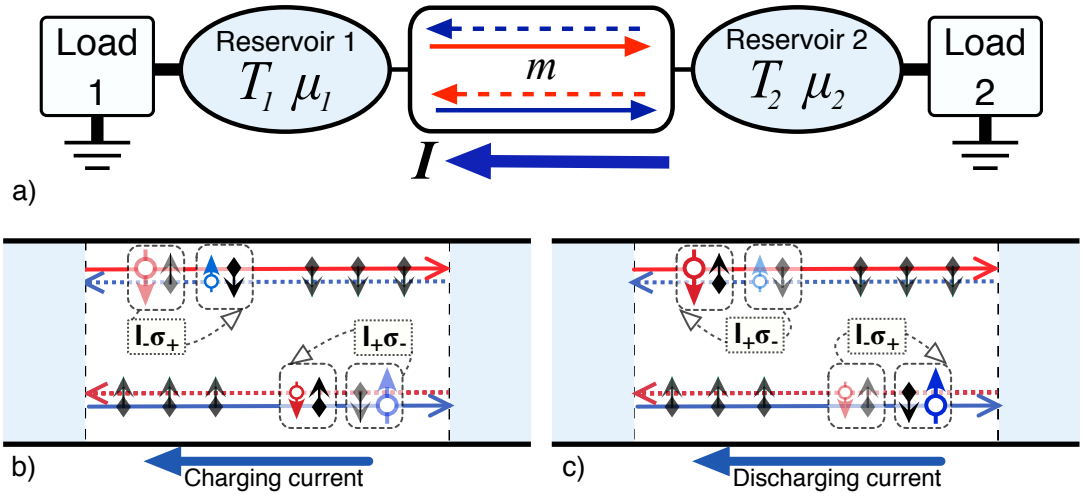

Figure 3.2: a) Quantum information engine setup with a quantum spin Hall insulator connected to two reservoirs. Graphical illustration of of b) the erasing the memory and c) the work extractions phases of the quantum information engine. The memory is erased via an applied bias current (or voltage), which creates an imbalance between the number of right movers (solid lines) and left movers (dashed lines) for both edges. The angular momentum transfer between the charge carriers and the nuclear spins result in a net mean polarization of the nuclear spins. In the work extraction case, a nonzero mean polarization causes selective backscattering, increasing the number of right movers for both edges. Thus a right flowing charge current is induced between two reservoirs.

We note that Maxwell's demon induced current is a backscattering current; hence the sign is opposite to the ballistic current term. We further emphasize that, this current is solely due to a nonzero mean polarization m and is nonvanishing even in the absence of an applied voltage bias. This is the manifestation of the Maxwell's demon effect; the information entropy of the nuclear spin subsystem induces a charge current even in the absence of a driving force such as a temperature gradient or chemical potential difference.

3.2.2 Generated Power and Extracted Work

We consider the setup shown in Fig. 3.2, where we attach electrical loads to the quantum information engine. We first focus on the case in which we represent the work extraction process under a reverse voltage bias V (opposite to current direction). We find the output power (Fig. 3.3) of the quantum information by multiplying the total current with the voltage and obtain:

$$P = \frac{eV}{h}\left(eV(1-\frac{\zeta}{2}) + \zeta\,\hbar\Gamma_T\, m\right), \tag{3.18}$$

where we define $\zeta = 2\pi N\gamma_0$ for convenience.

We find that the condition $eV < \frac{2\zeta\hbar\Gamma_T m}{(\zeta-2)}$ yields $P < 0$, signifying that the attached loads are powered by the quantum information engine. On the other hand, the opposite case in

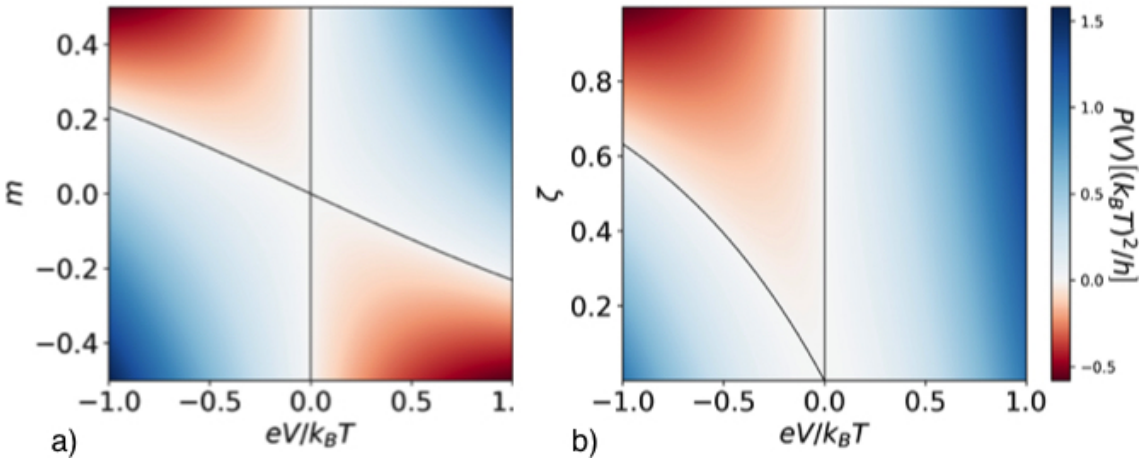

Figure 3.3: The output power of the quantum information engine, given by Eq. (3.18), with respect to voltage bias ($e > 0$) and a) with respect to mean polarization m with $\zeta = 1.0$ and b) with respecto to ζ with full polarization m = 0.5. We draw black solid lines to to separate the charging ($P > 0$) and discharging ($P < 0$) phases. Power attains negative values for $V < 0$ ($V > 0$) for a given mean polarization $m > 0$ ($m < 0$), indicating the discharging.

which $eV > \frac{2\zeta\hbar\Gamma_T m}{(\zeta-2)}$, the sign of the power is positive, indicating that the external circuit is charging the quantum information engine by polarizing the nuclear spins.

We next obtain the maximal amount of work done by the quantum information engine in the short edge limit. We find the optimal reverse voltage bias that maximizes the output power given in Eq. (3.18) and we perform the time integral up to a time when the output power vanishes:

$$W_{tot} = \beta k_B T N^2 \gamma_0, \tag{3.19}$$

where $\beta = \pi/4$ for constant reverse voltage bias (see Appendix D). The quadratic scaling of the maximum extracted work offers denser storage than conventional battery/supercapacitor counterparts with linear scaling. We note that the temperature appearing in Eq. (3.19) is limited by the quantum spin Hall insulator bulk band gap. We next demonstrate that the second law of thermodynamics is indeed satisfied by considering the general equation

$$P + k_B T \dot{S}_{\text{nuc}} \geq 0, \tag{3.20}$$

where S_{nuc} is the information entropy of the nuclear spin subsystem. As we extract work using nuclear spins as a memory resource ($P < 0$), we see that the information entropy of the nuclear spin subsystem has to increase. In the reverse process in which we erase the memory ($P > 0$), the information entropy of the nuclear spin subsystem decreases, which corresponds to the Landauer's erasure principle.

In the short edge limit, we use the output power given in Eq. (3.18) and obtain

$$\frac{P}{k_B T} + \dot{S}_{\text{nuc}} = \frac{k_B T}{h} \left[\widetilde{V}^2 + \zeta \widetilde{V}(\widetilde{V} + X)\right.$$

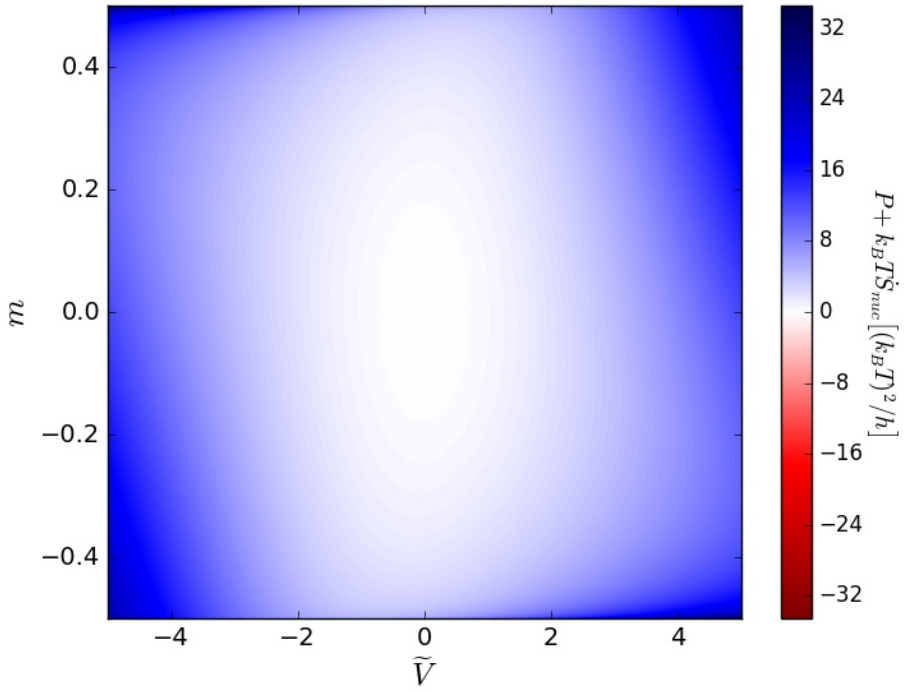

Figure 3.4: $P + k_B T \dot{S}_{\text{nuc}}$ as a function of $\widetilde{V}$ and m for $\zeta = 1$. Note that $P + k_B T \dot{S}_{\text{nuc}} \geq 0$, in agreement with the second law.

$$\times \left(m \coth \frac{\widetilde{V}}{2} - \frac{1}{2}\right)\Big] \geq 0, \tag{3.21}$$

where $\widetilde{V} \equiv eV/k_BT$ and $X = \ln\left(\frac{1+2m}{1-2m}\right)$, in agreement with the second law of thermodynamics (see Fig. 3.4).

3.2.3 Maximizing the Work Output via an External Load Resistance

In the previous section, we modeled work extraction and power generation of the quantum information engine under a constant reverse voltage bias, which we can choose to maximize power and/or work. In practice, an external load with a well-defined resistance is attached to the battery/engine in order to extract work, instead of applying a reverse voltage bias. Therefore, it is important to study the case in which the quantum information engine is connected to a load with conductance G_L, which is experimentally more relevant. The schematics of the setup we consider is shown in Fig. 3.5.

As we are interested in maximizing the extracted work for a given nuclear spin polarization, the necessary condition is that the induced voltage given in Eq. (3.16) must be negative, $V < 0$. In other words, we define a certain direction of the total current as positive for a given edge (see Fig. 3.2) and define the sign of the voltage accordingly. We

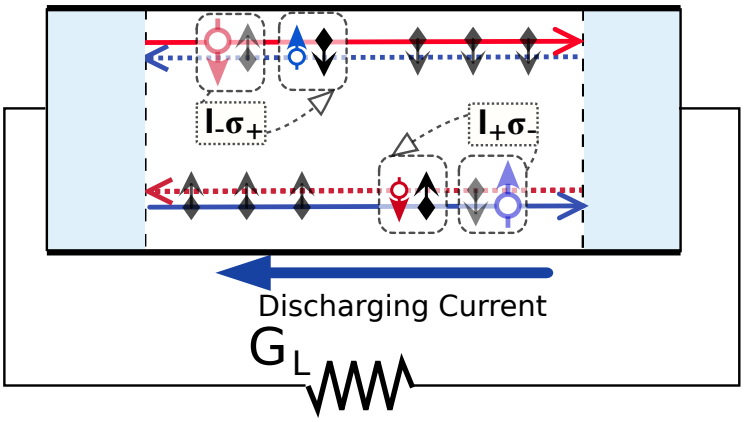

Figure 3.5: The setup for the work extraction phase. We attach the quantum information engine to an external load with conductance G_L.

now use the total current output of the quantum information engine given in Eq. (3.16) and find the induced current as:

$$I_{tot} = -G_0|V| + G_0|V|\frac{\zeta}{2} + G_0|V|m(t)\zeta \coth\left(\frac{e|V|}{2k_BT}\right). \tag{3.22}$$

where $G_0 = e^2/h$ is the conductance quantum, V is the *induced* voltage. In the remaining discussion, we drop $|V|$ notation and use $V > 0$ instead. Having this in mind, we employ the Kirchoff's Current Law and obtain the following equality:

$$G_L V = -G_{eq} V + G_0 V m(t)\zeta \coth\left(\frac{eV}{2k_BT}\right), \tag{3.23}$$

where we define $G_{eq} = G_0(1 - \zeta/2)$. Essentially, this describes the internal resistance of the quantum information engine. We now solve Eq. (3.23) for the induced voltage for a given load conductance and obtain the induced voltage as:

$$V = \frac{2k_BT}{e} \tanh^{-1}\left(\frac{m(t)\zeta}{\frac{G_L}{G_0} + (1 - \frac{\zeta}{2})}\right). \tag{3.24}$$

As anticipated, the induced voltage by the information entropy of the nuclear spins scales linearly with the temperature of the reservoirs. We further note that, for $m = 0$, there is no voltage induced by the quantum information engine, demonstrating the Maxwell's demon effect.

We now investigate two extreme cases for the external load, namely a short circuit ($G_L \to \infty$) and an open circuit ($G_L \to 0$). In the short circuit case (and short edge limit with

$\zeta \ll 1$), we obtain the induced voltage as:

$$V \approx \frac{2k_BT}{e}\frac{G_0}{G_L}m(t)\zeta. \tag{3.25}$$

We multiply Eq. (3.25) with the load conductance and obtain:

$$G_LV = I \approx \frac{2k_BT}{e}G_0m(t)\zeta. \tag{3.26}$$

We conclude that, in the short circuit case, quantum information engine operates as a current source. The magnitude of the current scales linearly with the total number of nuclear spins and mean polarization. In the open circuit case, the induced voltage is

$$\begin{aligned} V &= \frac{2k_BT}{e}\tanh^{-1}\left(\frac{m(t)\zeta}{1-\frac{\zeta}{2}}\right), \\ &\approx \frac{2k_BT}{e}m(t)\zeta, \end{aligned} \tag{3.27}$$

where in the last line we assume again short edge limit $\zeta \ll 1$. We notice that, in the open circuit case, quantum information engine operates as a voltage source.

We now consider the output power of the quantum information engine connected to the load with conductance G_L. We start with the mean polarization dynamics. We insert the voltage V given in Eq. (3.24) into Eq. (3.10) and we obtain:

$$\frac{dm}{dt} = \frac{\gamma_0k_BT}{\hbar}\tanh^{-1}\left(\alpha\, m(t)\right)\left(1-\frac{2}{\alpha}\right), \tag{3.28}$$

where we define dimensionless variable $\alpha = \frac{\zeta}{G_L/G_0+(1-\zeta/2)}$ for convenience. It is evident from Eq. (3.28) that quantum information engine reaches steady state when all nuclear spins depolarize and the nuclear spin subsystem reaches maximum entropy configuration. The power generated by the quantum information engine (for given V, hence m), and dissipated via the external load is given as

$$P = G_LV^2 = G_L\left[\frac{2k_BT}{e}\tanh^{-1}\left(\alpha\, m(t)\right)\right]^2. \tag{3.29}$$

At this point, we can choose to maximize either the generated power or the work extracted with respect to the load conductance G_L. We calculate the work extracted by quantum information engine as:

$$W = \int dtG_L\left[\frac{2k_BT}{e}\tanh^{-1}\left(\alpha\, m(t)\right)\right]^2. \tag{3.30}$$

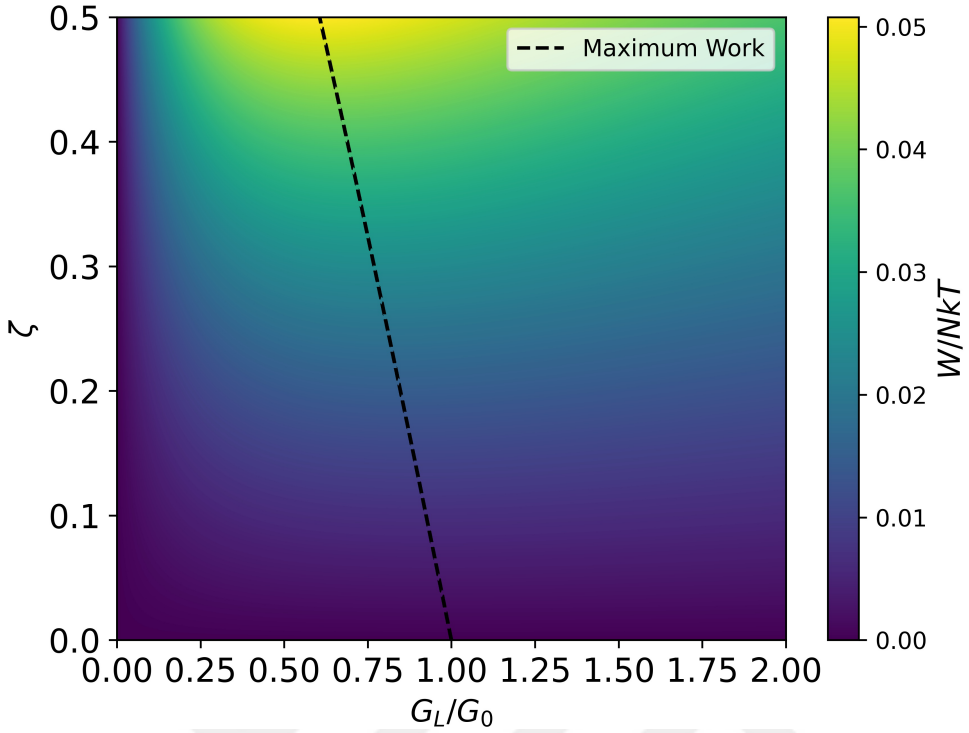

Figure 3.6: Extracted work in units of k_BT per total number of nuclear spins N for given ζ and load conductance G_L in units of conductance quantum G_0. The black dashed line shows the maximum work output for given ζ and G_L values.

It is straightforward to reexpress Eq. (3.30) and obtain:

$$W = \int dm \frac{dt}{dm} G_L \left[\frac{2k_BT}{e} \tanh^{-1}\left(\alpha\, m(t)\right) \right]^2, \tag{3.31}$$

$$= N \frac{G_L}{G_0} \frac{4k_BT}{2\pi\gamma_0} \frac{1}{\alpha - 2} \int_{\alpha/2}^{0} dy \tanh^{-1}\left(y\right), \tag{3.32}$$

where in the last line, we define $y = \alpha\, m(t)$ for convenience and make use of Eq. (3.28). We assume that initially all nuclear spins were polarized $m = 0.5$ and finally all nuclear spins depolarize as we deduced from Eq. (3.28) and set the boundary conditions accordingly. We perform the integral in Eq. (3.31) and obtain the total amount of work extracted for a given load conductance G_L as:

$$W = N \frac{G_L}{G_0} \frac{4k_BT}{2\pi\gamma_0} \frac{1}{2 - \alpha} \left(\frac{1}{2} \ln\left(1 - \frac{\alpha^2}{4}\right) + \frac{\alpha}{2} \tanh^{-1}\left(\frac{\alpha}{2}\right) \right). \tag{3.33}$$

We demonstrate Eq. (3.33) in Fig. 3.6. The maximum amount of extracted work per nuclear spin N follows the dashed line. We see that for the maximum work extraction, the value of the load conductance decreases for increasing ζ. Especially, in the short edge limit ($\zeta \ll 1$), we interpret this behavior as impedance matching: the maximum work

is obtained *almost* when $G_L = G_{eq} \equiv G_0(1-\zeta/2)$. For larger values of ζ, the load conductance in which the maximum work is obtained deviates from G_{eq}.

Finally, we investigate the scaling of work extracted with number of nuclear spins N, or equivalently, ζ. We find that the work extracted per nuclear spin for $G_L = G_{eq}$ scales linearly with N, hence the total work extracted scales quadratically with N, consistent with Eq. (3.19).

3.3 Quantum Information Engine in the Long Edge Limit

In this section, we investigate the transport properties of the quantum spin Hall insulator with nuclear spin distribution in the strong interaction regime, which we call the long edge limit. In this limit, we treat the electrons as phase coherent but nuclear spins semi-classically. As we explained in the previous section, the short edge limit is characterized by the condition $\zeta \leq 1$, indicating that the electron distribution functions of left and right reservoirs do not change significantly inside the quantum spin Hall insulator. However, in the long edge limit, we take the position dependence of the distribution functions into consideration, hence we relax the constraint on the total interaction strength ζ. We solve for the steady state Boltzmann equation given in Eq. (3.14), with the functional $\Gamma[f_+, f_-]$ is given as:

$$\Gamma[f_+, f_-] = \frac{2\pi\gamma_0}{L}\Big[N_\uparrow f_-(\epsilon,x)\big(1-f_+(\epsilon,x)\big) - N_\downarrow f_+(\epsilon,x)\big(1-f_-(\epsilon,x)\big)\Big], \quad (3.34)$$

where we ignore the position dependence of the nuclear spin subsystem.

We invoke the current conservation condition, $\partial_x(f_+ - f_-) = 0$, and make use of the ansatz $f_\pm(\epsilon,x) = g(\epsilon,x) \pm c(\epsilon)$. We insert this ansatz in Eq. (3.34) and get:

$$\begin{aligned}\partial_x g &= \frac{2\pi\gamma_0}{L}\Big(N_\uparrow(g-c)(1-g-c) - N_\downarrow(g+c)(1-g+c)\Big) \\ &= \frac{4\pi N\gamma_0}{L}\Big(m(g-g^2+c^2) - \frac{c}{2}\Big). \end{aligned} \quad (3.35)$$

We introduce $\xi = \frac{4\pi m N\gamma_0 x}{L}$ and obtain a dimensionless form of the differential equation given in Eq. (3.35) as $\frac{\partial g}{\partial \xi} = c^2 - \frac{c}{2m} - g^2 + g$. We rearrange the terms and obtain the integral form:

$$\int_{\tilde{g}}^{g} \frac{dg'}{\left(\frac{\chi}{2}\right)^2 - \left(g'-1/2\right)^2} = \int_{\xi_0}^{\xi} d\xi', \quad (3.36)$$

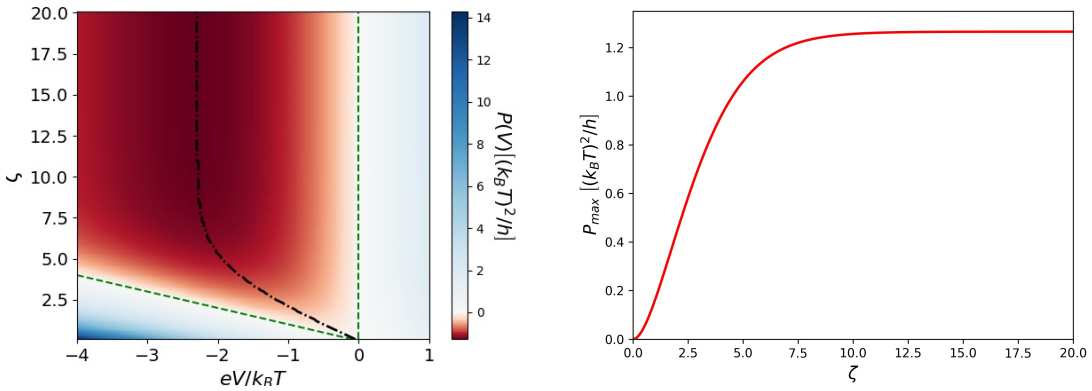

Figure 3.7: a)The power output of the quantum information engine, extended to the long edge limit $\zeta \gg 1$. The black dashed-line is the maximum power output generated. b) The maximum power output generated with respect to the total interaction strength ζ.

where we introduce $\chi = \sqrt{4c^2 - \frac{2c}{m} + 1}$ and $\tilde{g} \equiv g\big(\xi_0\big) = 0$. We perform the integral and obtain the distribution functions $f_{\pm}$:

$$f_{\pm}\left(\epsilon, \xi\right) = \frac{1}{2}\left(1 + \chi \tanh(\frac{\chi}{2}\left(\xi - \xi_0\right))\right) \pm c\left(\epsilon\right). \tag{3.37}$$

We impose the boundary conditions $f_{+}\left(x = -L/2\right) \equiv f_L^0$ and $f_{-}\left(x = L/2\right) \equiv f_R^0$, and numerically solve for the distribution functions. After obtaining the distribution functions $f_{\pm}$, we use Eq. (3.10) and Eq. (3.16) in order to obtain the nuclear spin polarization dynamics and total current in the long edge limit, respectively. Similar to Section 3.2, we obtain the output power and extracted work for a given interaction strength ζ and voltage bias V.

In Fig. 3.7, we show the power output of the quantum information engine in the long edge limit. We observe that after the power output reaches a threshold value of ζ, increasing the number of nuclear spins. The simplest way to achieve this is by making the device longer, but this approach does not yield more power output. This is consistent with the quantum bound on the maximum power output that can be drawn from a reservoir with a single quantum channel [69]. Hence, we argue that, instead of increasing the length of the quantum information engine, having a set of quantum information engines connected in parallel (similar to having multichannel quantum system) is more efficient.

We finally obtain the amount of work extracted from the quantum information engine in the long edge limit. We visualize our results in Fig. 3.8. First of all, we note that our results for the long edge limit and short edge limit overlap for $\zeta \ll 1$. However, as ζ increases, the quadratic scaling of the total work extracted turns into a linear behavior. We demonstrate this in Fig. 3.8 where we plot the work extraction per nuclear spin and observe the linear scaling behavior. We note that this linearization is anticipated, because

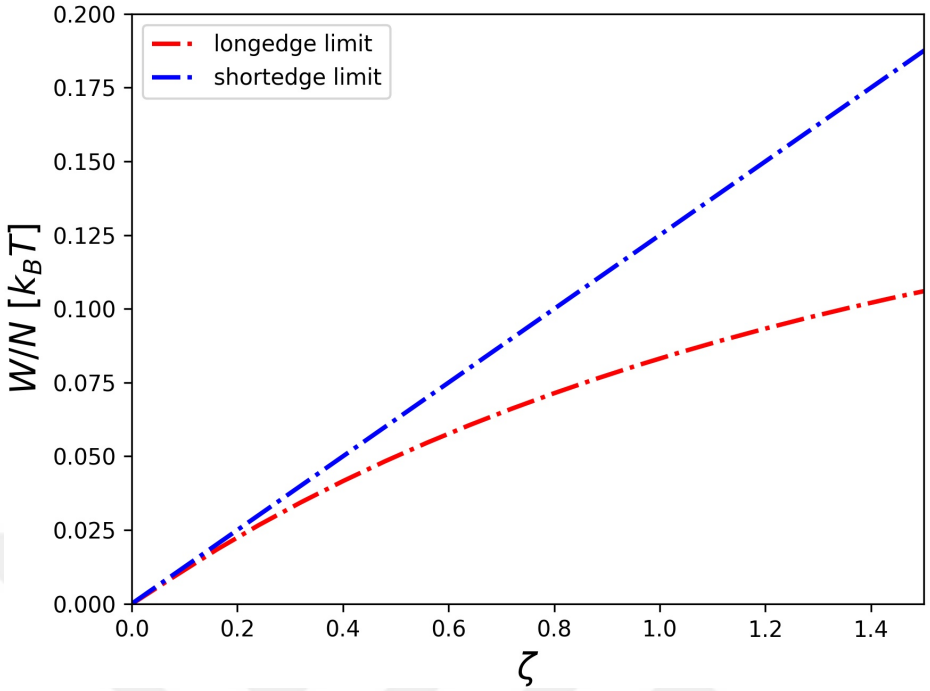

Figure 3.8: The extracted work from the quantum information engine, in units of k_BT per nuclear spin. The blue line is the short edge approximation, which fails for higher values of ζ. The red line is the solution in the long edge limit. We see that the quadratic scaling obtained in the short edge limit is linearized as ζ increases obeying the Landauer's bound.

the maximum work extraction is bounded by the Landauer's limit, which scales linearly with the memory size N.

3.4 Low Frequency AC-driven Quantum Information Engine

In this section, we investigate the current response of the quantum information engine when a low frequency AC voltage bias is applied. The main motivation behind investigating this AC case is based on an experimental measurement technique, lock-in measurement, in which a low frequency sinusoidal input signal is applied to the system and the same frequency response of the output signal is singled out. This technique is employed mainly to examine the DC characteristics of the system under consideration while attenuating the undesirable noise at other frequencies.

Without loss of generality, we consider a sinusoidal voltage, applied to the quantum information engine, $V(t) = V_0 \sin(\Omega t)$, where Ω is the reference frequency and V_0 is the

signal amplitude. We insert this AC voltage bias into Eq. (3.10) and obtain:

$$\frac{dm(t)}{dt} = \frac{\gamma_0}{\hbar}\left[\frac{eV_0}{2}\sin(\Omega t) - m(t)eV_0\sin(\Omega t)\coth\left(\frac{eV_0\sin(\Omega t)}{2k_BT}\right)\right]. \tag{3.38}$$

We consider the limit of low temperature, $k_BT \ll eV_0$, which is relevant for transport measurements. Hence, we approximate the term linear in m given in Eq. (3.38), ($\hbar\Gamma_T \approx \gamma_0 eV_0\,|\sin(\Omega t)|$), and obtain the differential equation for the mean polarization as:

$$\frac{dm(t)}{dt} = \frac{\gamma_0}{\hbar}eV_0\left(\frac{1}{2}\sin(\Omega t) - m(t)\,|\sin(\Omega t)|\right). \tag{3.39}$$

There is no closed form solution of this differential equation given in Eq. (3.39), therefore we reformulate the problem using Fourier analysis and numerically solve for the Fourier coefficients (see Appendix E) Subsequently, we reconstruct the mean polarization and plot its dynamics in Fig. 3.9.

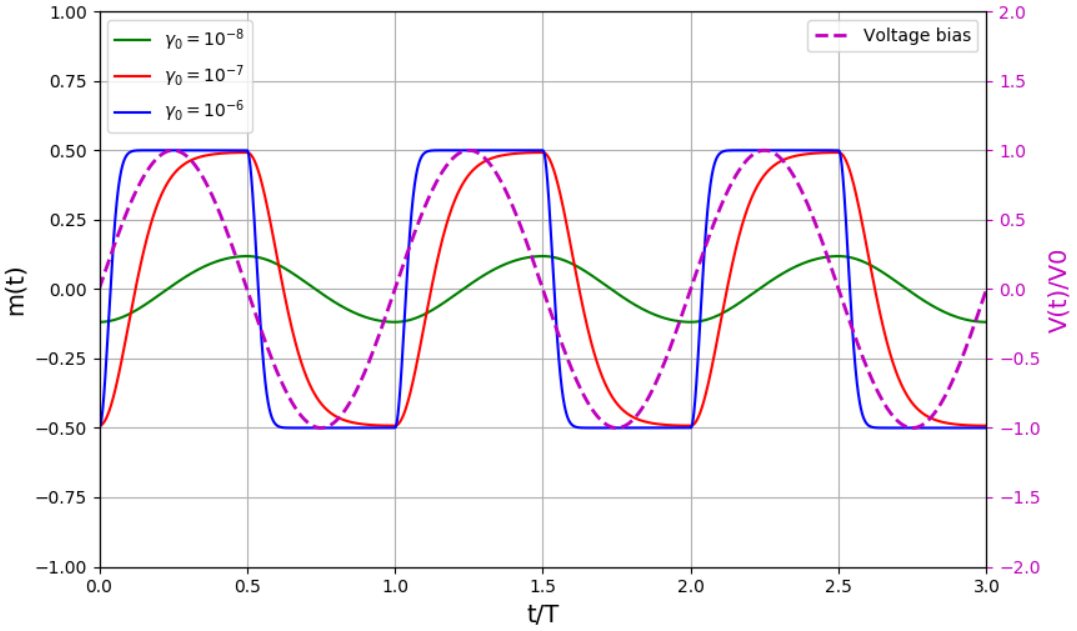

Figure 3.9: Mean polarization dynamics of quantum information engine under an AC voltage bias for three different γ_0 values. The sharp rises and falls of the mean polarization clearly indicate the presence of higher harmonics. We assume that temperature is zero, hence discharging is not visible.

In Fig. 3.9, we show that as γ_0 decreases, the maximum achievable mean polarization decreases as well. This is because the mean polarization characteristics time scale τ_m is inversely proportional to γ_0. Therefore, we conclude that in the high voltage bias limit, the ratio τ_m/T determines whether it is possible to erase the memory fully.

3.4.1 Lock-in Measurement Current Response

The Maxwell's demon induced current term included in the total current response of the quantum information engine depends on the time rate of change of the mean polarization (see Eq. (3.17)). We find the total current response under an AC bias as

$$I_{tot}(t) = I_{bias}(t) + I_{demon}(t) = \frac{e^2}{h} V_0 \sin(\Omega t) - eN \sum_{n=-\infty}^{\infty} in\Omega m_n e^{in\Omega t}. \tag{3.40}$$

As we noted earlier, in transport experiments, the DC characteristic response of a system is measured via lock-in measurement, in which a low frequency input signal is applied and the output signal is convoluted with the input signal in order to obtain the response of interest. However, the form of Eq. (3.40) suggests that higher harmonics (see Fig. E.1) also contribute to the mean polarization and consequently, to the induced current due to Maxwell's demon effect. We obtain the mathematical form of the current response of quantum information engine under such operation as follows:

$$\begin{aligned} I_{lock-in} &= \int dt I_{tot}(t) \times \sin(\Omega t) \\ &= \frac{e^2 V_0}{2h} - eN\Omega \,\mathrm{Re}[m_1]. \end{aligned} \tag{3.41}$$

We see that, lock-in measurements filter out the higher harmonics response of the quantum information engine. Furthermore, we note that the presence of nuclear spins and Maxwell's demon action give rise to a resistive behavior by reducing the total current below the ballistic limit. This resistance scales with the number of nuclear spins, hence with the length of the device.

3.4.2 General AC Current Response and Admittance of Quantum Information Engine

We now explore the general AC current response of the quantum information engine in the discharging phase ($k_B T \gg eV$). First, we take the Fourier transform of Eq. (3.10) and obtain:

$$m(\omega) = \frac{\gamma_0}{2\hbar} \frac{\tau_m}{1 + i\omega\tau_m} eV(\omega), \tag{3.42}$$

where ω is the angular frequency. We insert the Fourier coefficient of the mean polarization into the Fourier transform of Eq. (3.16) and obtain :

$$I(\omega) = \left[1 - \frac{\zeta}{2}\left(\frac{i\omega\tau_m}{i\omega\tau_m + 1}\right)\right] G_0 V(\omega). \tag{3.43}$$

We distinguish two contributions to the complex admittance $Y(\omega) = G(\omega) + iB(\omega)$ of the quantum information engine, where $G(\omega)$ is the conductance and $B(\omega)$ is the susceptance. We obtain the conductance and susceptance of the quantum information engine as:

$$G(\omega) = G_0\left(1 - \frac{\zeta}{2}\frac{\omega^2\tau_m^2}{1 + \omega^2\tau_m^2}\right), \tag{3.44}$$

$$B(\omega) = -G_0\frac{\zeta}{2}\left(\frac{\omega\tau_m}{1 + \omega^2\tau_m^2}\right). \tag{3.45}$$

We note that the form of the susceptance $B(\omega)$ indicates that the current-voltage characteristics of the discharging phase of the quantum information engine includes an inductive response. We find that the inductance of the quantum information engine is:

$$\begin{aligned} L_{\mathrm{QIE}} &= \frac{2\tau_m}{G_0\zeta} \\ &= \frac{\hbar^2}{e^2\gamma_0^2}\left(Nk_BT\right)^{-1}. \end{aligned} \tag{3.46}$$

We argue that the inductive response of the quantum information engine can be interpreted as an "emergent inductance", proposed by Ref. [70] for spiral magnets. We note that the inductance given in Eq. (3.46) is inversely proportional to the temperature and the number of nuclear spins. This peculiar feature of the inductance of quantum information engine can be utilized for applications that demand high inductance in mesoscopic and nanoscale systems.

3.5 Physical Implementation and Candidate Materials

We finally examine practicability of Maxwell's demon implementation in quantum spin Hall insulators. First and foremost, topological insulators with spin-momentum locked helical edge states are experimentally accessible for several materials [71, 72]. Materials featuring larger inverted bulk band gaps are not only desirable for experimental demonstration purposes, but also for increasing the operation temperature (and energy density) of quantum information engine.

We distinguish two separate functionalities of the quantum information engine based on the system parameters: (i) as a spin-supercapacitor/engine or (ii) a spin-battery. We establish that materials with high nuclear spin density with large hyperfine interaction strength yields higher energy and power densities. Furthermore, lower Fermi velocity of the helical edge states provides larger γ_0 which in return increases energy and power densities. On the other hand, smaller γ_0 values are favored for spin battery implementations. The reason is that the memory/spin retention times scale with the characteristics time scale for the mean polarization, which is inversely proportional to γ_0. This limit can be achieved by using materials with high Fermi velocity and/or reduced hyperfine interaction strength or via band engineering.

In Table. 3.1, we show the list of the most promising candidate materials, as of the time of writing, for quantum information engine implementation together with relevant material parameters and estimated values. For the rest of this section, we estimate the characteristic time scales for each material based on the reported parameters in the literature.

Candidate Materials for Quantum Information Engine

Material	Gap [meV]	T[K]	$A_0[\mu eV]$	$V_{\text{open}}[\mu V]$	$\gamma_0\,[10^{-11}]$	$\tau_m[s]$
WTe_2	55	100	0.6-6	0.02-2	$4-400$	$10^{-3}-10^{-5}$
InAs/GaSb	5	10	50	2.4-24	$1-10$	$1-10$
Bismuthene	800	300	5-(50)	3-(300)	$5-(500)$	$10^{-3}-(10^{-5})$
Bi_2Te_2Se	300	100	5-50	$0.1-10$	$10^{-2}-1$	$10^{-2}-1$

Table 3.1: Candidate materials for the implementation of quantum information engine. We take $L = 10\,\mu m$ for each device. The operation temperature is given by T in units of Kelvin.

WTe_2 monolayers

$1T'$ phase of epitaxially grown monolayer WTe_2 is theoretically predicted to exhibit quantum spin Hall insulator phase with a large bulk band gap [73]. Several experiments confirm that the bulk band gap is on the order of $10\ meV$ and it is one of the highest among all the candidates, allowing quantum information engine to be operated at high temperatures. ARPES measurements [74] show that the bands are inverted and a $55\ meV$ bulk band gap is opened. Indirect measurements of the band gap based on the transport mea-

surements at different temperatures yield insulating bulk and helical edge conduction up to 100 K [52, 53].

Unlike other candidates, transport measurements on WTe_2 yield quantum of conductance quantization [53]. Moreover, the saturation of the edge conduction for an applied magnetic field (breaking time-reversal symmetry) is observed for this material. The mechanism responsible for the band inversion is the spin-orbit coupling that hybridizes $5d_{xz}$ and $5d_{z^2}$ orbitals, giving rise to the helical edge states. Therefore, the electronic structure of the helical edge states alters the effective hyperfine interaction strength. The decay length of the helical edge states is approximately $1.8nm$ [74]. As a result of the monolayer structure of the material, helical edge states are confined within a relatively small region which increases the effective coupling strength γ_0. There is no reported measurement on the Fermi velocity v_F for the helical edge states of WTe_2, to this end, we extract the value for the Fermi velocity $v_F \approx 10^5$ from the band structure figure given in the Ref. [74]

The unit cell of WTe_2 is composed of 4 Te and 2 W atoms with the lattice constants 6.27Å and 3.48 Å. W has $\%14$ abundant nuclear spin $1/2$ and Te has $\%8$ abundant nuclear spin $1/2$. On average, WTe_2 is $\%10$ spinful. The low density of nuclear spins limits the work and energy densities of quantum information engine. This apparent disadvantage can be overcome by magnetic impurity doping and/or isotope selective epitaxy. The hyperfine interaction strengths for the free atoms of W and Te are given in the literature as $A_{\mathrm{W}} \approx 0.64\mu eV$ and $A_{\mathrm{Te}} \approx 8.3\mu eV$ [75], respectively. Hence, we take the average hyperfine constant as $A_0 \approx 6\mu eV$. On the other hand, the DFT calculations yield that the $p-$orbital contribution for the conduction electrons are negligible, hence the the hyperfine interaction is predominantly due to Tungsten atoms, i.e. $A_0 \approx A_{\mathrm{W}} \approx 0.64\mu eV$. Since there is no experimental confirmation on the orbital nature of the edge states and the hyperfine interaction strength in WTe_2 monolayers, we calculate the relevant system parameters for both cases.

We calculate the effective coupling strength between the helical edge states of WTe_2 and the nuclear spins:

$$\gamma_0 = \frac{A_0^2 a_x^2 a_y^2 a_z^2}{l_z^2 l_y^2} \frac{1}{8\pi\hbar^2 v_F^2} \approx 4 \times 10^{-9}. \tag{3.47}$$

We use Eq. (3.27) and estimate the open circuit voltage as:

$$\begin{aligned} V_{\mathrm{open}} &= 4\pi N \gamma_0 \frac{k_B T}{e} m, \\ &= 2 \times 10^{-9} \times \big(T[K]\big) \times \big(L[\mu m]\big), \end{aligned} \tag{3.48}$$

for fully polarized nuclear spins. For a system with length $\mathcal{O}(10\,\mu m)$ and temperature $\mathcal{O}(100\,K)$, we obtain the open circuit voltage $V_{\text{open}} \sim 2\,\mu V$. Correspondingly, we obtain the characteristic time scales for the dynamical nuclear polarization $\tau_m \approx 10^{-5} s$.

InAs/GaSb double quantum wells

We next consider InAs/GaSb heterostructures, predicted to be tuned in quantum spin Hall insulator phase via double gating (top- and bottom-gates). Apart from the experimental difficulties, InAs/GaSb double quantum well is the most promising candidate for experimental verification of quantum information engine proposal. The experiments show quantized conductance up to temperature $4\,K$, although the mentioned bulk band gap value is around $40 - 60K$ [51]. On the other hand, several other groups raised concerns over the origin of the quantized conductance, claiming that the edge states are trivial in nature [76].

We perform our calculations based on the system parameters provided in Ref. [51]. The thickness of the quantum wells are $12.5\,nm$ for InAs and $10\,nm$ for GaSb. The interface between these two layers was doped with Si atoms in order to reduce the residual bulk conductivity. The band inversion is achieved by the hybridization of the $s-$like conduction bands $p-$like heavy hole bands of the two layers, hence the resulting edge states are mainly $s-$like. The Fermi velocity is very low ($v_F \approx 4.6 \times 10^4 m/s$) [59] compared to other candidate systems, yielding larger dimensionless interaction strength γ_0, and consequently leading to higher power and work densities. The decay length of the helical edge states is approximately $\hbar v_F/\Delta \approx 10nm$ and the whole thickness of the double quantum well bounds the edge states in the growth direction.

One of the main advantages of InAs/GaSb is that all nuclei is spinful and their spins are larger compared to other candidates ($I_{\text{In}} = 9/2, I_{\text{As}} = 3/2, I_{\text{Ga}} = 7/2, \%43\, I_{\text{Sb}^{123}} = 7/2$ and $\%57\, I_{\text{Sb}^{121}} = 5/2$). Therefore, the value $N\gamma_0$ in InAs/GaSb quantum wells are larger and hence InAs/GaSb is expected to yield higher energy and power densities. The average hyperfine constant is $A_0 \approx 50\mu eV$ [59]. The unit cell for both InAs and GaSb is of zinc-blende type with 4 atoms of In (Ga) and 4 atoms of As (Sb) present. The average lattice constant is $a_0 \approx 6.1$ Å.

We then calculate the effective coupling strength between the nuclear spins and the helical edge electrons:

$$\gamma_0 = \frac{A_0^2 a_0^6}{S^2} \frac{1}{8\pi\hbar^2 v_F^2} \approx 10^{-11} - 10^{-12}, \tag{3.49}$$

where $S \approx 500 a_0^2$ is the cross-section at right angles to propagation direction. We see that,

although the hyperfine interaction is larger compared to WTe_2 and the Fermi velocity is smaller, the effective coupling strength is orders of magnitude smaller for the InAs/GaSb case due to larger cross-section. Subsequently, we obtain the open circuit voltage as:

$$\begin{aligned} V_{\text{open}} &= 4\pi N \gamma_0 \frac{k_B T}{e} m, \\ &\approx 2.4 \times 10^{-7(-8)} \times \big(T[K]\big) \times \big(L[\mu m]\big)\, V, \end{aligned} \tag{3.50}$$

for fully polarized nuclear spins. For a system with length $\mathcal{O}\big(10\,\mu m\big)$ and temperature $\mathcal{O}\big(10\,K\big)$, we obtain the open circuit voltage $V_{\text{open}} \sim 2.4 - 24\,\mu V$. We argue that for better localization for the helical edge states in the transverse direction, the open circuit voltage can be enhanced significantly. Finally, we obtain the characteristic time scales for the dynamical nuclear polarization $\tau_m \approx 1 - 10s$.

Bismuthene monolayers on Silicon Carbide (SiC)

Epitaxially grown Bismuth honeycomb monolayer (Bismuthene) on the insulating silicon carbide (SiC) substrate is predicted to be in quantum spin Hall insulator phase with a large bulk band gap, based on the pivotal role of the large on-site spin-orbit coupling induced by the substrate. These predictions were partially confirmed by the observation of edge states and insulating behavior of the bulk of monolayer Bismuthene, from the experimental results [77]. Scanning tunneling spectroscopy (STS) and ARPES measurements for Bismuthene yield bulk band gap values around $0.8eV$, and the Fermi energy E_F is in the bulk band gap. However, the topological nature of the observed edge states in this experiment is still unknown; transport characteristics and behavior under the magnetic field is yet to be seen as the time of writing this thesis.

The lattice constant of Bismuthene is found to be 5.35 Å [77]. Similar to InAs/GaSb, all nuclei for Bismuthene is spinful with $I_{Bi} = 9/2$, with a reported Fermi contact interaction hyperfine constant around $50\mu eV$.On the other hand, the DFT calculations show that the helical edge states are predominantly of $p-$like (p_x and p_y to be specific), although there is a nonnegligible s-orbital contribution, around $\%10$. Hence, we obtain an average hyperfine constant based on the edge state orbital decomposition and the nuclei in question and find $A_0 \approx 5\mu eV$.

The flake sizes reported in Ref. [77] are around $a_0 \approx 25\,nm$ due to phase slip boundaries, but the size of the flakes is expected to be increased by advanced epitaxial growth techniques. The differential conductance measurements show that the edge states decay within a length of approximately one unit cell, 4 ± 1 Å. There is no reported experimental value for the Fermi velocity for Bismuthene, but we can estimate a lower bound by

simply assuming that the edge states cover the entire Brillouin zone within the band gap, hence we have $v_F \approx \Delta a_0/\hbar 2\pi = 4 \times 10^4 m/s$. But, the band structures shown in the literature allow us to extract information from the slope of the dispersion relation, and we find $v_F \approx 10^5 m/s$. We stress that this value is based on theoretical estimation, hence further experimental demonstration is needed. For the sake of argument, we make use of this value throughout the calculations.

In this case,we obtain the effective coupling strength between the nuclear spins and the helical edge electrons as:

$$\gamma_0 = \frac{A_0^2 a_0^6}{S^2} \frac{1}{8\pi\hbar^2 v_F^2} \approx 5 \times 10^{-11} \tag{3.51}$$

where the $S \approx a_0^2$ for Bismuthene, hence the edge states display better localization at the edges. This effect of the extremely small cross-section increases the effective coupling strength, similar to WTe_2 case. This γ_0 is subjected to change once the Fermi velocity v_F and the hyperfine coupling constant A_0 values in the literature are experimentally demonstrated. The corresponding open circuit voltage is given as:

$$\begin{aligned} V_{\text{open}} &= 4\pi N \gamma_0 \frac{k_B T}{e} m, \\ &\approx 10^{-9} \times \big(T[K]\big) \times \big(L[\mu m]\big)\, v, \end{aligned} \tag{3.52}$$

for fully polarized nuclear spins. Although the Bismuthene flakes in Ref. [77] are around $25\,nm$ in size, we estimate the open circuit voltage for a system with length $\mathcal{O}\big(10\,\mu m\big)$ and room temperature $300\,K$, and obtain $V_{\text{open}} \sim 3\,\mu V$. We emphasize that this open circuit voltage is achieved with smaller number of nuclear spins (since it is a monolayer system) compared to InAs/GaSb double quantum well structures , hence the energy and power densities are expected to be larger for Bismuthene. The characteristic time scales for the dynamical nuclear polarization $\tau_m \approx 1\,ms$ at the room temperature. This value is significantly shorter than any other candidates, demonstrating that Bismuthene is a better choice for engine applications.

Bi_2Te_2Se 3D Topological Insulator

Another candidate for quantum information engine is exfoliated Bi_2Te_2Se (BTS221) thin flakes. Unlike other candidates, BTS221 is a 3D topological insulator with topological surface states. This makes BTS221 by itself a completely different system than its quantum spin Hall insulator counterparts. However, these surface states still feature spin-momentum locking, hence it is possible to utilize them to polarize the nuclear spins. Even

though we investigate the 3D topological insulators from the perspective of Maxwell's demon implementations in Chapter 5, we examine BTS221 as a candidate for quantum information engine for the sake of completeness. We note that, for the rest of the calculations, we obtain the relevant results for BTS221 based on the 2D topological insulator model.

Recent experiments demonstrated that thin flakes of BTS221 feature long polarization-retention times [78]. The main reason is that BTS221 topological insulator has a large Fermi velocity ($v_F \approx 3 - 5 \times 10^5 m/s$) [79], which leads to lower electron spin-nuclear spin-flip interaction strength. As a result, the memory retention times are much longer, as well as larger amounts of current is needed to reset the memory. Furthermore, the bulk band gap values reported in the literature are quite large, $300meV$, which makes it possible to operate quantum information engine in higher temperatures ($\Delta > 100K$).

Nuclear spin abundance in BTS221 is not as high as InAs/GaSb double quantum well but still high enough to be considered as a suitable candidate for spin battery applications. $\%100$ abundant Bismuth has $I_{Bi} = 9/2$, $\%8$ abundant Tellurium has $I_{Te} = 1/2$ and $\%7.6$ abundant Selenium has $I_{Se} = 1/2$. Fermi contact interaction constant for free Bismuth is around $50\mu eV$. Similar to the Bismuthene case, surface states are predominantly of $p-$like (p_x and p_y to be specific), although there is a nonnegligible s-orbital contribution, around $\%10$. This may decrease the average hyperfine constant for BTS221, leading to two orders of magnitude uncertainty for γ_0 (see Table 3.1).

The lattice constant of BTS221 is $a_0 \approx 0.63nm$ and the average mass of a single nuclei is approximately $150u$ in units of atomic mass. The effective coupling strength between the nuclear spins and the helical edge electrons is given as:

$$\gamma_0 = \frac{A_0^2 a_0^6}{S^2} \frac{1}{8\pi\hbar^2 v_F^2} \approx 10^{-11} - 10^{-13}. \tag{3.53}$$

We note that equation above is obtained based on the 2D topological insulator model, hence *the cross-section of the surface states* is actually not defined. However, we take $S \approx 100\, a_0^2$ for BTS221, comparable to the InAs/GaSb double quantum wells. We stress that the calculations that take 3D topological insulator properties into account would alter the γ_0 value.

$$\begin{aligned} V_{\text{open}} &= 4\pi N \gamma_0 \frac{k_B T}{e} m, \\ &\approx 10^{-8} - 10^{-10} \times \big(T[K]\big) \times \big(L[\mu m]\big)\, V, \end{aligned} \tag{3.54}$$

for fully polarized nuclear spins. We estimate the open circuit voltage for a system with length $\mathcal{O}\big(10\,\mu m\big)$ and temperature $100\,K$, and obtain $V_{\text{open}} \sim 0.1 - 10\,\mu V$. The char-

acteristic time scales for the dynamical nuclear polarization τ_m (at $100\,K$ temperature) is given by

$$\tau_m = \frac{\hbar}{2k_B T\gamma_0} \approx 10^{-2} - 1s.$$

3.6 Conclusion

In summary, we proposed and investigated a novel Maxwell's demon implementation using quantum spin Hall insulators and nuclear spins and/or magnetic impurity spins. Upon describing the working principle of our model, we demonstrated the thermodynamic cycle of the quantum information engine and derived the equations for the power output and equivalent energy storage capacity. We investigated the current-voltage characteristics of the quantum information engine under DC and AC voltage bias. Furthermore, we considered the quantum information engine as a circuit element and investigated the case where an external load is attached to it. We also established that the quantum information engine exhibits inductive response and subsequently, we derived its inductance, which scales inversely proportional to the number of nuclear spins. Finally, we examined the several candidate materials for the experimental realization of the quantum information engine and compared their open circuit voltages and corresponding time scales for nuclear spin polarization.

Chapter 4

MAXWELL'S DEMON IN A QUANTUM ANOMALOUS HALL INSULATOR: A CAPACITIVE QUANTUM INFORMATION ENGINE

Heat dissipation in electronic devices is one of the main problems in modern technological applications. In addition to this problem, the need for high efficiency devices with low-power consumption has increased dramatically. Therefore, the study of systems where the ambient heat can be converted into electrical work attracted attention. The advent of quantum thermodynamics offers a way to realize such devices that operate at the nanoscale, allowing for remarkable control over the individual particles [80]. Various novel proposals on such quantum heat engines, some of which are based on thermoelectric and photovoltaic devices.

Alternative methods of energy storage were also proposed among which the Maxwell's demon offers an interesting solution (see, for example, Ref. [4] for a review). As we discussed in Chapter 3, Maxwell's demon implementations allow for heat-to-work conversion, where one bit of information can be utilized to extract work by an amount $k_B T \ln 2$ from the environment. The ultimate bound on the heat dissipation of such Maxwell's demon implementations is given by the Landauer's limit, $Q \geq N k_B T \ln 2$, where N is the size of the memory. One of the ultimate goals of quantum thermodynamics is to reach Landauer's limit in a scalable quantum system.

In this chapter, we propose and investigate a second novel Maxwell's demon implementation that is capable of operating at the Landauer's limit in a mesoscopic platform. In

Chapter 3, we introduced a Maxwell's demon implementation in a quantum spin Hall insulator in which the present nuclear spins/magnetic impurities are utilized as a nonvolatile memory via dynamical nuclear spin polarization [1]. However, in this chapter, we focus on a setup that is composed of a hybrid system containing two quantum anomalous Hall insulators (also known as Chern insulators) with opposite spins and chirality and either (i) a quantum spin Hall insulator which contain nuclear spins/magnetic impurities in a single edge (Fig. 4.1) or (ii) a junction that contains nuclear spins/magnetic impurities (Fig. 4.2). This new implementation also relies on the backscattering mechanism of the helical edge states of the quantum spin Hall insulator, similar to the quantum information engine. Accordingly, the nuclear spins/magnetic impurities constitute a nonvolatile memory. However, as opposed to quantum information engine, it is possible to erase Maxwell's demon memory by a minimum amount of heat dissipation, which is set by the Landauer's principle. Moreover, we show that it is possible to extract all the stored energy in the memory in the form of electrical work. This is achieved by connecting the device to an external load, with the method of impedance matching.

This chapter is organized as follows: In Sec. 4.1, we present the implementation of this second quantum information engine for which we coin the name capacitive quantum information engine. In Sec. 4.2, we explain the demon protocol of our model and derive the formulas for the charging and discharhing phases of the capacitive quantum information engine. We then investigate the possible procedures in order to charge/discharge more efficiently. In Sec. 4.3, we demonstrate that the capacitive quantum information engine is an ideal memristor and we calculate its memristance. We give a summary in Sec. 4.4.

4.1 Capacitive Quantum Information Engine

In this section, we show how to realize a more efficient Maxwell's demon implementation as a result of specific leads. In particular, we demonstrate that the quantum information engine that we described in Chapter 3 can be significantly improved by replacing the metallic leads that host both spin species with two quantum anomalous Hall insulators with different spins and chiralities. The idea behind this observation is that, during the erasure phase of the quantum information engine, the Joule heating occurs when there is no change in the nuclear spin polarization. In other words, the ballistic conduction of the helical edge states during the charging phase leads to heat dissipation, while there is no change in the state of the memory. This allows for another dissipation channel for the quantum information engine, which may reduce the overall efficiency.

One way to discard this additional dissipation mechanism is to design an overall setup that

only allows heat dissipation when there is a spin-flip scattering. As we show below, in order to realize this setup, specialized leads with different spins and chiralities are required. We consider the case in which these specialized leads are quantum anomalous Hall insulators with opposite spin and chirality (see Fig. 4.1). Characterized by chiral edge states and insulating bulk due to nontrivial topological band structure, quantum anomalous Hall insulators require no external magnetic field, as opposed to the quantum Hall insulators. The absence of the external magnetic field is essential for our proposal, in order to not break the degeneracy of the nuclear spin subsystem. Incorporating these leads into the quantum information engine, we come up with a new design which we call capacitive quantum information engine due to its capacitive response, as opposed to the inductive response of the quantum information engine described in Chapter 3.

As it is customary in any Maxwell's demon implementation, we illustrate the charging/discharging cycle of the capacitive quantum information engine. We show that the capacitive quantum information operates at the Landauer's limit during the erasure (charging) phase. In return, Maxwell's demon harvests maximum amount of thermal energy, set by the Landauer's limit, and convert into useful work that can extracted electrically via an external load.

Since most of the constituents of the capacitive quantum information engine is the same as the quantum information engine, we recommend the reader to review Chapter 3 for a description of quantum spin Hall insulators and dynamical nuclear spin polarization.

4.2 Demon Protocol

In this section, we describe the demon protocol of the capacitive quantum information engine. Without loss of generality, we choose that the left lead has chiral edge states with spin up propagating counter-clockwise direction, whereas the right lead has chiral edge states with spin down propagating clockwise direction, as shown in Fig. 4.1. The nuclear spins/magnetic impurities are located at the bottom edge of the device (see Fig. 4.1) with quantum spin Hall insulator and at the junction for the second setup (see Fig. 4.2). We stress that the second setup is more realistic as having nuclear spins only located at the bottom edge of the device shown in Fig. 4.2 is experimentally challenging. We note that, in the absence of any mechanism that can flip the spins of the edge electrons, the conductance vanishes because there are no available states for the edge electrons in the other lead. Therefore, the only way to transmit an electron through the device is to flip its spin via nuclear spins. In this way, any time a spin-flip occurs, one bit of information is erased (by polarizing nuclear spins) and an electron is transmitted from one lead to the

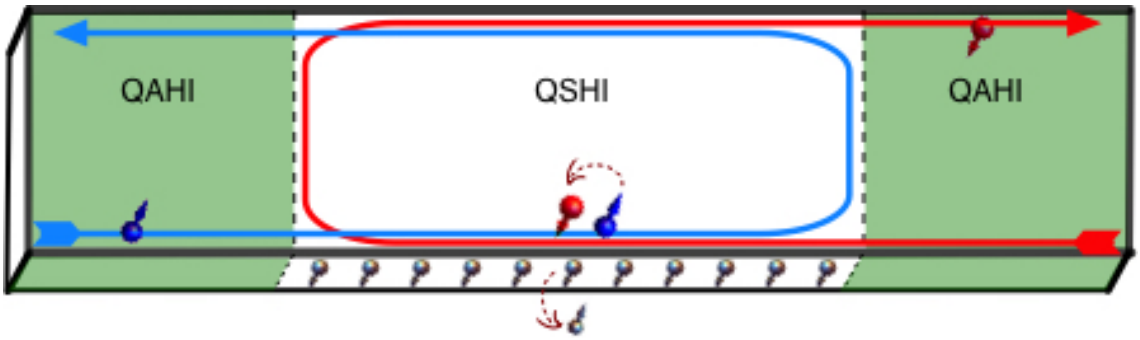

Figure 4.1: Capacitive quantum information engine version 1. The left lead is a quantum anomalous Hall insulator with spin-up electrons propagating in counter-clockwise direction, while the right lead is another quantum anomalous Hall insulator with spin-down electrons propagating in clockwise direction along the edge. The quantum spin Hall insulator contains nuclear spins and/or magnetic impurities that allow spin-flip processes.

other. The transmission of electrons leads to Joule heating, in the spirit of Landauer's erasure principle. Conversely, we show that polarized nuclear spins/magnetic impurities can be utilized to extract thermal energy from the reservoirs in the form of electrical power output.

4.2.1 Magnetization Dynamics and Induced Current

We now quantify our model. Similar to quantum information engine, we define a mean polarization of the nuclear spins/magnetic impurities in the system, $m = (N_\uparrow - N_\downarrow)/2N$, where $N_{\uparrow(\downarrow)}$ is the total number of up(down) nuclear spins and $N = N_\uparrow + N_\downarrow$ is the total number of nuclear spins in the system. In the presence of a constant applied voltage bias V, the rate of change of mean polarization dynamics is given by [1]:

$$\frac{dm}{dt} = \frac{\gamma_0}{\hbar}\left[\frac{eV}{2} - m(t)eV\coth\left(\frac{eV}{2k_BT}\right)\right], \tag{4.1}$$

where γ_0 is dimensionless interaction strength for a single nuclear spin and T is the temperature of the system. For a nuclear spin interacting with the helical edge states in a quantum spin Hall insulator, $\gamma_0 = (A_0^2 a^6)/8\pi\hbar^2 v_F^2 S^2$, where A_0 is the hyperfine constant, a is the lattice constant, v_F is the Fermi velocity and S is the cross-section of the helical edge states.

Eq. (4.1) shows that the demon memory that is characterized by the mean polarization m of the nuclear spins/magnetic impurities can be erased by applying a voltage bias to the system. We first consider the case of a DC voltage bias and obtain the time evolution of the mean polarization as:

$$m(t) = (m_0 - \bar{m})\mathrm{e}^{-t/\tau_m} + \bar{m}, \tag{4.2}$$

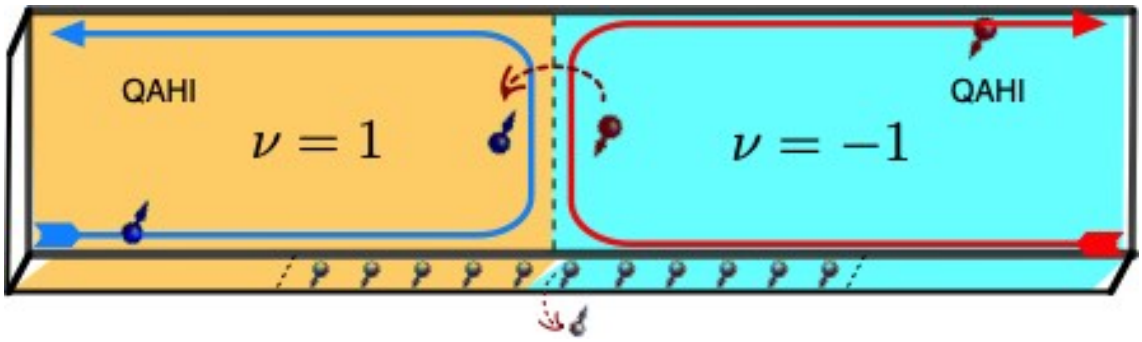

Figure 4.2: Capacitive quantum information engine version 2. The leads are the same as in version 1, but in this case, there is no quantum spin Hall insulator in between.

where m_0 is the initial mean polarization and $\bar{m} = (1/2)\tanh(eV/2k_BT)$ is defined to be the target mean polarization and $\tau_m = (\gamma_0 eV/\hbar)^{-1}\tanh(eV/2k_BT)$ is the characteristic time scale. We observe that mean polarization dynamics of the capacitive quantum information engine is the same as the one in quantum information engine.

The essential difference between the capacitive quantum information engine and the quantum information engine is manifested in the charge current response of the system. We obtain the total charge current (see Appendix F for the derivation):

$$I_{tot} = eN\frac{dm}{dt}. \tag{4.3}$$

We notice from Eq. (4.3) that the system generates a charge current response only when there is a change in the mean polarization of the nuclear spins that can be only achieved via the spin-flip scattering. In other words, there can be no electron transmitted through the system without an associated nuclear spin-flip taking place. We demonstrate this by considering an applied DC voltage bias, and obtain the current-voltage characteristics of the system as:

$$I_{tot} = G_0 V\zeta\left(\frac{1}{2} - m(t)\coth\left(\frac{eV}{2k_BT}\right)\right), \tag{4.4}$$

where $G_0 = e^2/h$ is the quantum of conductance, $\zeta = 2\pi N\gamma_0$ is the effective interaction strength of the capacitive quantum information engine. It is evident that, even in the absence of voltage bias or a temperature gradient, finite mean polarization yields finite charge current. This demonstrates the demon effect of the capacitive quantum information engine that can be utilized as an engine that is capable of converting the thermal energy into electrical energy.

4.2.2 Memory Erasure Phase

We now show how to erase the memory of the capacitive quantum information. Since the memory is formed by the nuclear spins/magnetic impurity spins, memory erasure process corresponds to dynamical nuclear spin polarization. The Landauer's erasure principle dictates that there is minimum amount of heat dissipation required in order to erase the memory. In our model, we find that an erasure process using a DC voltage bias produces heat dissipation above the Landauer's limit, even though one can minimize the heat dissipation with a proper choice of voltage bias (see Appendix G).

On the other hand, achieving the Landauer's limit is possible for an adiabatic erasure process. This is very similar to the Carnot cycle of a classical thermodynamic engine. In our model, this idea translates into adiabatically changing the applied voltage bias in such a way that the amount power required is minimized. We find that this amounts to having a voltage profile that satisfies the condition $\dot{m} = 0$. Using Eq. (4.1), we obtain the required voltage to be:

$$V(m(t)) = \frac{2k_BT}{e} \tanh^{-1}(2m(t)). \tag{4.5}$$

The amount of heat dissipated during the erasure process is given by the integral of electrical power, $P = IV$, over time. We use the voltage profile given in Eq. (4.5) and the corresponding charge current given in Eq. (4.3) and obtain the amount of heat dissipated in the system as:

$$\begin{aligned} Q &= N \int_0^{1/2} dm\, eV(m), \\ &= 2Nk_BT \int_0^{1/2} dm\, \tanh^{-1}(2m), \\ &= Nk_BT\big(\frac{1}{2}\ln(1-4m^2) + 2m\tanh^{-1}(2m)\big)\Big|_0^{1/2}, \\ &= Nk_BT \ln 2. \end{aligned} \tag{4.6}$$

We observe that the amount of heat dissipated in the process of adiabatic erasing of the memory of the capacitive quantum information scales with the number of nuclear spins and/or magnetic impurities and satisfies the Landauer's bound. It is also worthwhile to note that we assume that the memory was completely used before the erasure procedure ($m = 0$) and we choose to erase the memory completely ($m = \pm 1/2$), as the limits of the integral in Eq. (4.6) suggests. In the case of partial erasure, the amount of total heat dissipation may differ.

4.2.3 Work Extraction Phase

We now demonstrate how to utilize the blank memory of the capacitive quantum information engine for work extraction. A blank memory ($m = \pm 1/2$) leads to an imbalance between spin up electrons and spin down electrons by transferring spin angular momentum from the nuclear spin subsystem to electron subsystem. As the left and right reservoirs have opposite spins and chiralities, this imbalance induces a charge current, which then can be extracted by applying a reverse voltage bias or attaching the capacitive quantum information engine to an external electrical load. In this way, Maxwell's Demon harvests available heat energy from the reservoirs and power the load.

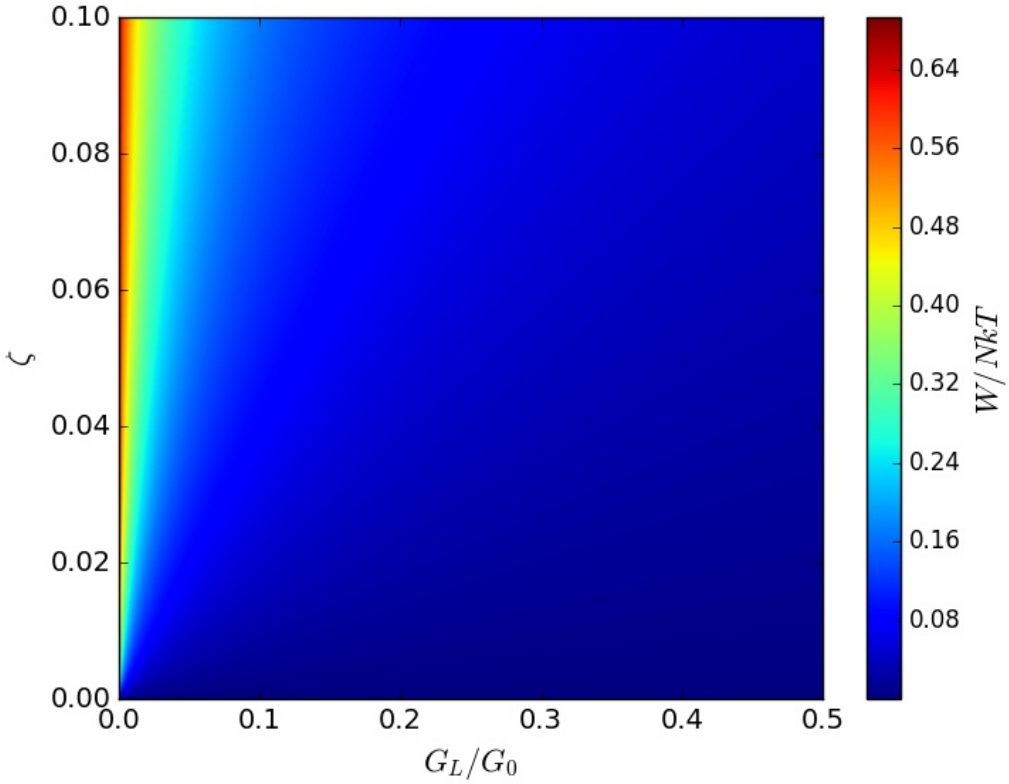

Figure 4.3: Work extracted per N in units of k_BT for capacitive quantum information engine for given ζ and load conductance G_L in units of conductance quantum G_0.

We consider the case where an external load is attached to the capacitive quantum information engine with a blank memory. As the current induced by the capacitive quantum information engine flows in the opposite direction to the voltage (signaling power generation), when we match the total current given in Eq. (4.4) with the current on the load, we need to have an additional minus sign. We make use of the Kirchoff's current law and

obtain

$$G_L V = -G_0 V \zeta \left[\frac{1}{2} - m(t) \coth \left(\frac{e|V|}{2k_B T} \right) \right], \tag{4.7}$$

where G_L is the conductance of the external load. We solve for the induced voltage for a given load conductance and obtain

$$V = \frac{2k_B T}{e} \tanh^{-1} \left(\alpha m(t) \right). \tag{4.8}$$

where $\alpha = \zeta/(G_L/G_0 + \zeta/2)$. We notice that the induced voltage given in Eq. (4.8) is of the same form as the applied voltage in the charging phase, given in Eq. (4.5). The only difference is the multiplicative factor in front of m, where the former has the factor α and the latter has the factor 2. In the limit of vanishing load conductance and hence vanishing power (this corresponds to a reversible process), we have $\alpha = 2$. Using the voltage given in Eq. (4.8), we obtain the amount of work extracted from fully polarized nuclear spins (see Appendix G):

$$W = N \frac{G_L}{G_0} \frac{2k_B T}{\zeta} \frac{1}{2 - \alpha} \left(\ln \left(1 - \frac{\alpha^2}{4} \right) + \alpha \tanh^{-1} \left(\frac{\alpha}{2} \right) \right), \tag{4.9}$$

and display it in Fig. 4.3. We observe that in the limit of high load resistance, $G_L \ll G_0$, the amount of work given in Eq. (4.9) is limited by the Landauer's limit, as expected. We interpret this as the impedance matching condition, where the maximum work extraction is possible only when the resistance of the external load matches with the internal resistance of the capacitive quantum information engine.

We further show that the scaling behavior of the work extracted by capacitive quantum information engine with respect to ζ. Landauer's erasure principle tells us that the quadratic behavior of the total work extracted has to turn into a linear behavior. Stated in another way, the work extracted per nuclear spin is bounded above by $k_B T \ln 2$. As shown in Fig. 4.4, the amount of extracted work per bit approaches $k_B T \ln 2$ for increasing values of load resistance.

4.2.4 AC Response of the Capacitive Quantum Information Engine

In this subsection, we investigate the general AC current response of the capacitive quantum information engine in the discharging phase ($k_B T \gg eV$). As the name suggests, we find that the response is equivalent to an RC circuit. We demonstrate this by taking the

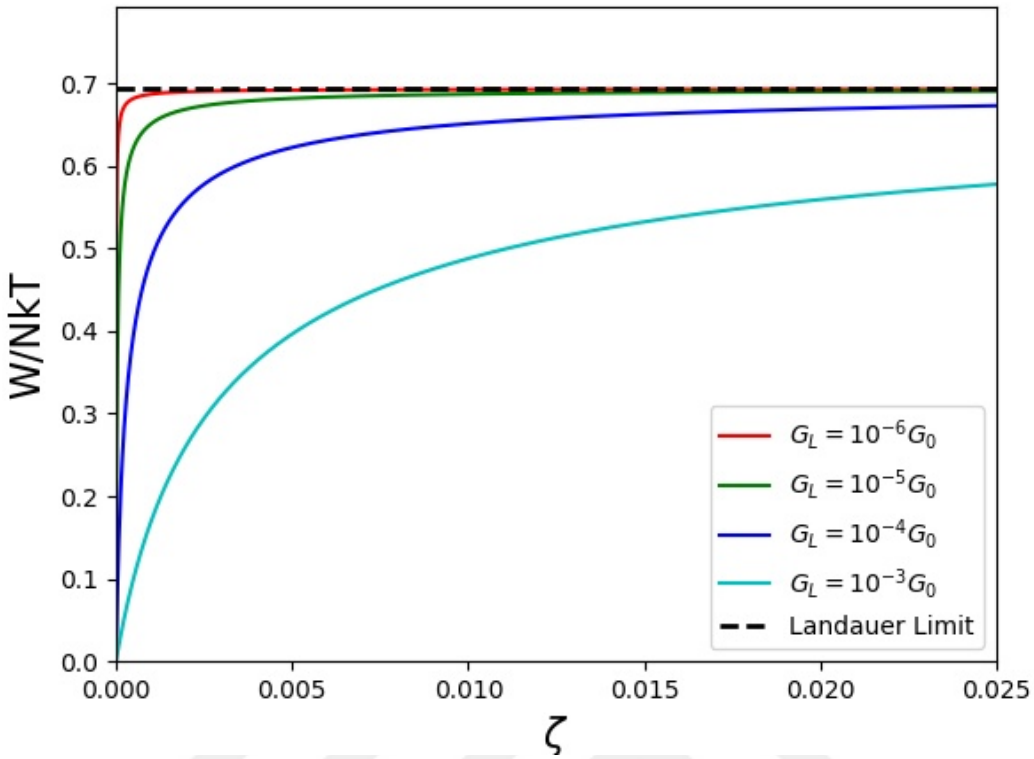

Figure 4.4: Work extracted per N in units of $k_B T$ for the capacitive quantum information engine vs. ζ with load conductance G_L in units of conductance quantum G_0. The dashed line represents the Landauer's bound on the extracted work.

Fourier transform of Eq. (4.1) and Eq. (4.3), and we obtain:

$$I(\omega) = G_0 \frac{\zeta}{2} \left(\frac{i\omega\tau_m}{i\omega\tau_m + 1} \right) V(\omega). \tag{4.10}$$

We observe that in the limit of $\omega\tau_m$
$l1$, the AC response is of capacitor type. We find the equivalent capacitance of this quantum information engine to be:

$$C_{\text{QIE}} = \frac{e^2 N}{4 k_B T}. \tag{4.11}$$

We see that the capacitance of the quantum information engine scales with the number of nuclear spins N. This result is anticipated as each polarized nuclear spin can "store" an electric charge. In other words, a total of N polarized nuclear spins can store an amount of eN electric charge.

4.3 Ideal Memristor

Memristor is an electronic circuit component where the resistance depends on the amount of charge that has flowed through it, predicted by L. O. Chua as “the missing circuit element" [81]. In 2008, the first experimental realization of the memristor in a two-terminal device which is composed of TiO_2 between two platinum sheets was performed [82]. Spintronic systems are regarded as promising candidates for memristor applications [83], among other platforms that were proposed and experimentally demonstrated [84–86] . There have been several theoretical proposals [87] and experimental demonstrations [88] of memristive behavior in spintronic systems.

In this section, we illustrate another interesting prominent feature of the capacitive quantum information engine; it can be utilized as an ideal memristor. In general, any system that shows resistance with a memory can be considered as a memristive system. As opposed to other memristive system, the resistance of an ideal memristor depends only on the amount of charge that has flowed through it and no other additional parameters [89]. We find that the current-voltage characteristics of the capacitive quantum information engine satisfies this definition.

In general, memristive systems satisfy the following current-voltage characteristics [90]

$$I(t) = M^{-1}(x(t))V(t), \tag{4.12}$$

with x being an internal state variable of the system, obeying the following relation:

$$\frac{dx}{dt} = f(x, V), \tag{4.13}$$

where M is the memristance and f is a function of the internal state variable x and voltage V. On the other hand, as opposed to other memristive system, the resistance of an ideal memristor depends only on the amount of charge that has flowed through it and no other additional parameters. In other words, a memristor is defined as an ideal memristor, if the internal state variable x corresponds to the charge q.

Having this in mind, we argue that in our setup, the internal state variable x corresponds to the mean polarization of the nuclear spins, m. Correspondingly, the rate of change of mean polarization given in Eq. (4.1), satisfies Eq. (4.13). However, considering only the rate of change of mean polarization is not enough to conclude that the capacitive quantum information engine is an ideal memristor.

However, as Eq. (4.3) suggests, there is a one to one correspondence between the current

flowing through the capacitive quantum information engine and the rate of change of mean polarization in our system. Hence, the amount of charge flowing through the device can be tracked via the change in polarization of the nuclear spins:

$$\frac{dq}{dt} = -eN\frac{dm}{dt}. \tag{4.14}$$

We see that the total amount of charge flowing through the device is found to be as $N\int_0^t dm = N(m(t) - m_0) \equiv N\Delta m(t)$. As the resistance of the system depends on the polarization of the memory, we conclude that the capacitive quantum information engine is an ideal memristor.

We now calculate the memristance of the capacitive quantum information engine. We focus on the charging phase where we apply a voltage bias with the condition $eV \gg k_B T$. Then, Eq. (4.1) reduces to:

$$\frac{dm}{dt} = \frac{\gamma_0 eV}{\hbar}\left(\frac{1}{2} - m\right). \tag{4.15}$$

In order to proceed, we need to define the corresponding magnetic flux. We achieve this by integrating both sides of Eq. (4.15) and we obtain:

$$\varphi = -\frac{\hbar}{e\gamma_0}\ln\big(1 - 2m\big), \tag{4.16}$$

where $\varphi = \int dtV$ is the magnetic flux. As we discussed above, there is a one-to-one correspondence between the mean polarization and the charge. We obtain this relation between charge q and polarization m as:

$$m(t) = \frac{q(t)}{eN} + m_0, \tag{4.17}$$

where we assume $m(t = 0) = m_0$ and $q(t = 0) = 0$. We interpret this equation in the following way: The state of the nuclear spin subsystem that is characterized by the mean polarization uniquely specifies the amount of charge flowing through the system. We insert this back into Eq. (4.16), we obtain the relation between the flux and the charge:

$$\varphi = -\frac{\hbar}{e\gamma_0}\ln\left(1 - 2\left(\frac{q(t)}{eN} + m_0\right)\right). \tag{4.18}$$

This is the fundamental relation for our memristor, linking the magnetic flux and charge. One note of caution is in order here. The magnetic flux defined in this system is not the "real magnetic flux" but an analogous magnetic flux.

Finally, we find that the memristance of the capacitive quantum information engine in this

limit is given as:

$$M(q) = \left[G_0 \zeta \left(\frac{1}{2} - m_0 - \frac{q}{eN} \right) \right]^{-1}. \tag{4.19}$$

We notice that, in the case of initially nonpolarized nuclear spin subsystem, the memristance of the capacitive quantum information engine only depends on the amount of charge flowing through the system. On a side note, the total amount of charge that can flow through the system is limited by the number of nuclear spins and the initial mean polarization, as the memristance given in Eq. (4.19) cannot assume negative values.

4.4 Conclusion

In conclusion, we proposed and investigated a novel Maxwell's demon implementation with a scalable memory. The trademark of the capacitive quantum information is that the amount of heat dissipation during the memory erasure process can be scaled down to the Landauer's limit. The overall increase in efficiency in comparison to the the quantum information engine proposal described in Chapter 3 is facilitated by the quantum anomalous Hall insulators. We presented the demon protocol of the capacitive quantum information engine and derived the relevant equations for heat-to-work conversion process, as well as the memory erasure process. We found that the capacitive quantum information engine is capable of extracting all the available entropy out of the nuclear spin subsystem and utilize it by converting the thermal energy into electrical work. Moreover, we confirmed that the capacitive quantum information engine indeed requires minimum amount of heat dissipation when the memory is erased adiabatically. Finally, we demonstrated that the capacitive quantum information is also an ideal memristor that can be used in electronic circuit applications.

Chapter 5

MAXWELL'S DEMON IN A THREE DIMENSIONAL TOPOLOGICAL INSULATOR: DISORDER EFFECTS

In this chapter, we investigate the three dimensional topological insulators from the perspective of Maxwell's demon effect. 3D topological insulators feature 2D surface states that exhibit spin-momentum locking, and for that reason, can be considered as a platform for Maxwell's demon implementations utilizing the hyperfine interaction between charge carriers and nuclear spins.

This chapter is organized as follows: In Section 5.1, we introduce the 3D topological insulators and focus on the topologically protected surface states. In Section 5.2, we investigate and study the Maxwell's demon effect for 3D topological insulators in the presence of nuclear spins. We discuss the main differences between 2D topological insulators and 3D topological insulators from the point of view of Maxwell's demon implementations. We then focus on the diffusive transport regime and obtain the diffusion equation for the surface states interacting with both nuclear spins and nonmagnetic impurities in Section 5.3. Finally, we give a brief conclusion in Section 5.4.

5.1 Three Dimensional Topological Insulator

Following the discovery of quantum spin Hall insulators, the three dimensional version of the time-reversal invariant topological insulators was predicted [91, 92]. Analogous to its 2D counterpart, 3D topological insulators have a bulk band gap and conducting surface

states, which are topologically protected by the time-reversal symmetry. The topological phases of 3D topological insulator is described by four Z_2 invariants $(\nu_0; \nu_1, \nu_2, \nu_3)$, where the invariant ν_0 characterizes whether the topological insulator is a strong topological insulator $(\nu_0 = 1)$ or a weak topological insulator $(\nu_0 = 0)$. In this section, we focus on strong topological insulators and recommend the reader to review Ref. [71] for an in-depth discussion on topological phases of 3D topological insulators.

The surface Fermi circle of a strong topological insulator encloses an odd number of Dirac points. These 2D Dirac points are Kramers degeneracy points and the low-energy dynamics in the vicinity of these Dirac points are described by 2D Dirac Hamiltonian:

$$H = \hbar v_F (\mathbf{k} \times \boldsymbol{\sigma}) \cdot \hat{z}, \tag{5.1}$$

where v_F is the Fermi velocity, where $\boldsymbol{k} = (k_x, k_y)$ is the momentum and $\boldsymbol{\sigma}$ is the vector of Pauli matrices in electron spin space. The Hamiltonian for the surface states given in Eq. (5.1) is almost identical to the graphene band structure, except for the fact that graphene contain at least four Dirac points (including spin and valley degrees of freedom), whereas a single surface state of a 3D topological insulator contains only one Dirac point. This is in violation with the Nielsen-Ninomiya theorem that states a single massless Dirac fermion cannot exist in a 2D lattice with time-reversal symmetry [93]. The resolution of this paradox is that there has to be another Dirac fermion residing on the opposite surface.

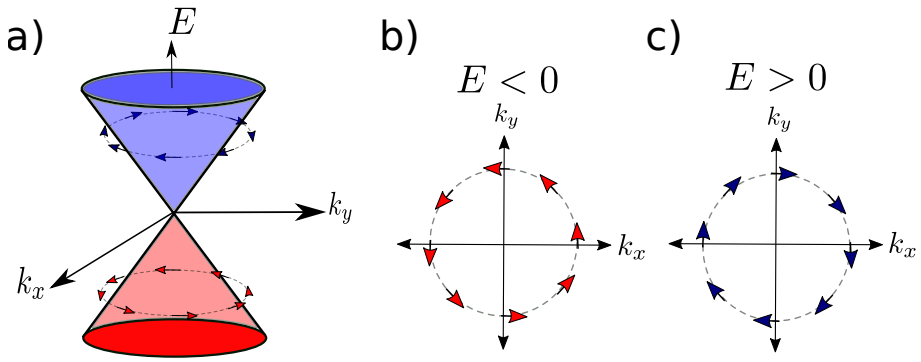

Figure 5.1: a) The dispersion relation for the surface states of a 3D topological insulator. Here, the arrows represent the spin projection of the surface states, determined by the Hamiltonian given in Eq. (5.1). The sign of the spin chirality changes for the surface states with energy b) below or c) above the Dirac point $E = 0$.

Another prominent feature of the surface states of a 3D topological insulator is the helical spin texture. In an ordinary 2D metal, every point on the Fermi circle contains both up and down spin states. However, the surface states of a 3D topological insulator do not have spin degeneracy; the time-reversal symmetry necessitates that states with opposite momenta $\mathbf{k}$ and $-\mathbf{k}$ have opposite spins. As a result, electrons acquire a π Berry phase while encircling the Fermi circle.

The immediate consequences of the π Berry phase is the absence of backscattering and consequently absence of localization for the surface states in the presence of disorder. Similar to helical edge states of the quantum spin Hall insulator phase, the surface states of 3D topological insulators do not suffer from localization under any time-reversal invariant perturbation that does not cause bulk band gap to be closed. As typical for systems with spin-orbit coupling, this brings about weak antilocalization effects. On the other hand, the transport on the surface of a disordered 3D topological insulator is diffusive, whereas transport remains ballistic for quantum spin Hall insulators even in the presence of disorder.

5.2 Maxwell's Demon Effect at the Surface of a 3D Topological Insulator

In this section, we examine the feasibility of Maxwell's demon effect at the surface of 3D topological insulators, similar to the problem we considered in Chapter 3 using quantum spin Hall insulators. We identify the differences and similarities of both 2D and 3D topological insulators, from the point of view of Maxwell's demon effect.

Both 2D and 3D topological insulators exhibit perfect spin-momentum locking, making them useful for Maxwell's demon implementations via spin-flip scattering with the nuclear spins and magnetic impurities. However, the main difference between the helical edge states of a quantum spin Hall insulator and surface states of a 3D topological insulator is the spin quantization axis; the helical edge states have a particular spin quantization axis, owing to one-dimensional nature of the edge states. However, electrons on the surface of 3D topological insulators can propagate in any direction on the surface, resulting in no definite spin quantization axis [71, 91].

We start by defining the effective Hamiltonian that describes the dynamics of the surface states of 3D topological insulators:

$$H_0 = \hbar v_F (\mathbf{k} \cdot \sigma). \tag{5.2}$$

We note that for convenience, we perform a rotation in spin space to the Hamiltonian given in Eq. (5.1) around spin-z axis, so that the spin and momentum points in the same direction. This choice of spin orientation does not change the physics of the problem.

In order to study the properties of the surface states of 3D topological insulators, we first diagonalize the Hamiltonian for the surface states H_0 given in Eq. (5.2) and obtain its

eigenstates as:

$$\psi_{\mathbf{k}\pm}(\mathbf{x}) = \frac{1}{\sqrt{2}} \begin{pmatrix} 1 \\ \pm e^{i\theta} \end{pmatrix} \frac{e^{i\mathbf{k}\cdot\mathbf{x}}}{\sqrt{LW}}, \tag{5.3}$$

where $\theta = \tan^{-1} k_y/k_x$ is the polar angle in the momentum space and L and W are the length and width of the system, respectively. Furthermore, $\pm$ represents the states with different helicity with energies $E = \pm\hbar v_F|\mathbf{k}|$. Without loss of generality, we consider the case where the Fermi energy lies above the Dirac point and focus on $+$ helicity eigenstate and we drop the helicity sign for clarity. We note that the angle θ uniquely specifies the spin orientation of the surface states for a given helicity, and for $+$ helicity, we have $\boldsymbol{s} = \cos(\theta)\hat{x} + \sin(\theta)\hat{y}$.

We shall distinguish two sources of scattering, namely the nonmagnetic impurity scattering, for which we use the term *disorder*, and nuclear spin and/or magnetic impurity scattering which may lead to spin-flip interaction. We assume uncorrelated disorder potential $V(\mathbf{x})$ that obeys $\langle V(\mathbf{x})V(\mathbf{x}')\rangle = D\delta(\mathbf{x} - \mathbf{x}')$, where D is the strength of the disorder. Next in order are the nuclear spins; the dominant source of interaction between the electrons and nuclear spins is the hyperfine Fermi contact interaction, given by:

$$H_{hf} = \frac{\lambda}{2} \sum_n \mathbf{I}^n \cdot \boldsymbol{\sigma}\delta(\mathbf{r} - \mathbf{r}_n). \tag{5.4}$$

Here, the factor $1/2$ is for the nuclear spins and $\lambda = A_0 v_0/\xi$ is the hyperfine interaction strength, A_0 is the hyperfine coupling, $v_0 = a_0^3$ is the unit cell volume, ξ is the surface state decay length in z-direction, $\mathbf{I}_n$ represents the Pauli spin matrices for the n^{th} nuclear spin at position $\mathbf{x}_n = (x_n, y_n)$.

We investigate these two distinct sources of scattering mechanism and compare the resulting probability of elastic scattering from an initial state $\mathbf{k}$ to a final state $\mathbf{k}'$ on the Fermi circle. For scattering from single nonmagnetic impurity, we have:

$$p_{nm}(\mathbf{k}, \mathbf{k}') = \cos^2(\Delta\theta/2), \tag{5.5}$$

where the subscript nm denotes the nonmagnetic impurity scattering and $\Delta\theta \equiv \theta - \theta'$ is the scattering angle. On the other hand, for a scattering processes which changes the direction of a nuclear spin, we have:

$$p_{sf}(\mathbf{k}, \mathbf{k}') = \sin^2(\Delta\theta/2). \tag{5.6}$$

where the subscript sf denotes the spin-flip scattering.

We visualize the normalized scattering probability for each case using a polar coordinate

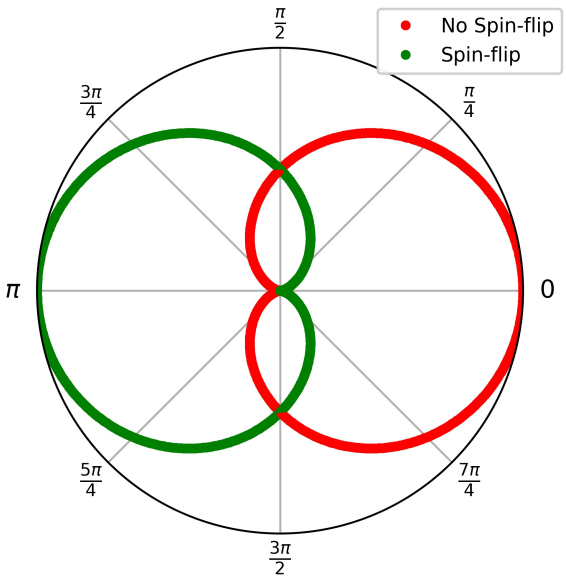

Figure 5.2: The normalized scattering probability of the surface states as a function of the relative angle $\Delta\theta$ for process without spin-flip (shown in red) and with spin-flip (shown in green).

shown in Fig. 5.2, where the distance from the origin is the probability of scattering. First and foremost, we observe that for both nonmagnetic impurity scattering and scattering in which the initial and final states of the nuclear spins are known, which we simply call spin-flip scattering, the scattering probability is anisotropic, which is a manifestation of the nature of 2D Dirac fermions. We distinguish the probability of backscattering for each case; when the spin-flip scattering is not allowed (shown in red), backscattering probability $(\Delta\theta = \pi)$ vanishes, whereas for perturbations that allow spin-flip scattering (shown in green) we have $p_{sf}(\Delta\theta = \pi) = 1$.

At first glance at Eq. (5.5) and Eq. (5.6), one can conclude that the surface states of 3D topological insulators exhibit necessary ingredient for a Maxwell's demon implementation; that is the backscattering of the surface states is only possible via spin-flip scattering with the nuclear spins. This is an essential ingredient for the discharging (work extraction) phase of any Maxwell's demon implementation using our prescription. However, we notice that backscattering is also possible without spin-flip scattering in the diffusive regime. For multiple scattering events from nonmagnetic impurities, the momentum and consequently the spin of the surface states are randomized. Therefore, the surface states suffer from backscattering due to nonmagnetic impurities for samples with length larger than the elastic mean free path ℓ_{el} set by the disorder strength.

In view of this additional backscattering mechanism, let us first consider the nuclear spins only, in order to get a glimpse of the Maxwell's demon effect in 3D topological insulators. We focus on ballistic samples with system size smaller than the elastic mean free path, where we expect backscattering to occur only via spin-flip with the nuclear spins. We

investigate the effect of the nuclear spins on the electron relaxation time by invoking the Fermi's Golden rule:

$$\tau^{-1}_{\mathbf{k}\to\mathbf{k}';} = \frac{2\pi}{\hbar}\frac{A_0^2 v_0^2}{4L^2W^2}\frac{1}{\xi^2}\sum_n \Bigg[\sin^2(\Delta\theta/2)\delta_{m_n,m_n'} + \frac{1}{4}\delta_{m_n-1,m_n'} + \frac{1}{4}\delta_{m_n+1,m_n'}\Bigg]\delta(\hbar v_F(k-k')), \tag{5.7}$$

where m_n and m_n' are the initial and final spin projections for the n^{th} nucleus, respectively. As we consider the electron dynamics first, we perform the sum over the possible nuclear spin configurations and obtain:

$$\tau^{-1}_{\mathbf{k}\to\mathbf{k}'} = \frac{2\pi}{\hbar}\frac{A_0^2 v_0^2}{4L^2W^2}\frac{N}{\xi^2}\Bigg[\sin^2(\Delta\theta/2) + \frac{1}{2}\Bigg]\delta(\hbar v_F(k-k')), \tag{5.8}$$

where $N = N_\uparrow + N_\downarrow$ is the total number of nuclear spins. We note that this scattering rate of the surface states from the nuclear spins includes both spin-flip scattering and the spin-conserving forward scattering. Therefore, the nuclear spins also lead to momentum relaxation via forward scattering.

We now focus on the dynamics of the nuclear spins in the absence of a voltage bias. We take the electronic distribution functions into account and obtain the rate of flips from nuclear spin up to nuclear spin down:

$$\begin{aligned}\Gamma_{-+} &= \frac{1}{8\pi}\frac{A_0^2 v_0^2}{\xi^2}\frac{1}{(\hbar v_F)^4}N_\downarrow\int\frac{dE}{\hbar}\,E^2 f_+(E)(1-f_-(E)),\\ &= \frac{1}{8\pi\hbar}\frac{A_0^2 v_0^2}{(\hbar v_F)^4\xi^2}N_\downarrow\left(E_F^2 + \frac{\pi^2}{3}k_B^2T^2\right)k_BT,\end{aligned} \tag{5.9}$$

where $f_\pm$ is the electron distribution function with spin up/down projected along the direction set by the propagation of the electrons in a two-terminal geometry in a quasi-1D system. Correspondingly, this choice of spin quantization-axis also determines the polarization direction of the nuclear spins. We note that while deriving this rate of flipping, we assume that there only a single mode is occupied.

We now consider the low temperature limit, $E_F >> k_BT$, which is the experimentally relevant limit. We again define a mean polarization and obtain the rate of change of mean polarization as:

$$\Gamma_{-+} - \Gamma_{+-} \equiv \frac{dm}{dt} = -2mN\frac{1}{8\pi\hbar}\frac{a_0^2}{\xi^2}\left(\frac{E_F}{E_B}\right)^2\left(\frac{A_0}{E_B}\right)^2 k_BT. \tag{5.10}$$

where we define an energy scale $E_B = \hbar v_F/a_0$ which roughly corresponds to the bulk band gap of the 3D topological insulator. We stress that we assume no applied voltage

bias, hence Eq. (5.10) describes the depolarization process. We infer the time scale of this process:

$$\tau_m^{-1} \equiv \left(\Gamma_{+-} - \Gamma_{-+}\right)/mN = \gamma_0^{3D} \frac{2k_B T}{\hbar}, \tag{5.11}$$

where we define an effective interaction strength $\gamma_0^{3D} = \frac{1}{8\pi}\frac{a_0^2}{\xi^2}\left(\frac{E_F}{E_B}\right)^2\left(\frac{A_0}{E_B}\right)^2$. We indicate that, as compared to the time scale of mean polarization dynamics of its 2D counterpart, the rate of change of mean polarization dynamics of a 3D topological insulator contains an additional factor of $(E_F/E_B)^2$. We note that we consider the case in which E_F is in the band gap. Therefore, if we also consider possible bulk thermal excitations which may eventually hinder the demon effect, we conclude that this factor can be substantially smaller than unity. This feature offers an explanation to long-retention times seen in experiments [78].

5.3 Diffusive Regime

In the previous section, we established that the surface states of a 3D topological insulator can be used to realize a Maxwell's demon implementation. However, as opposed to the quantum spin Hall insulators, the presence of nonmagnetic impurities at the surface of 3D topological insulators leads to a diffusive transport regime which makes the analysis of Maxwell's demon more complicated. Therefore, an extensive study of the impact of nonmagnetic impurity scattering on the Maxwell's demon effect is required. The diffusive limit of the 3D topological insulators (without the nuclear spins) and its transport properties have been studied in detail [94–96]. In this section, we investigate the contribution of the disorder on the spin-charged coupled transport of electrons interacting with the nuclear spins, for 3D topological insulators.

We start with the Hamiltonian of the overall system:

$$H = H_0 + H_{hf} + V(\mathbf{x}), \tag{5.12}$$

where H_0 describes the surface states of a 3D topological insulator (single surface) given by Eq. (5.1), H_{hf} is the hyperfine interaction between the electrons and the nuclear spins (Eq. (5.4)) and finally, $V(\mathbf{x})$ describes the nonmagnetic impurity potential, specified by a random Gaussian disorder potential profile $\langle V(\mathbf{x})V(\mathbf{x}')\rangle = n_0 U^2 \delta(\mathbf{x}-\mathbf{x}')$ and zero mean value $\langle V(\mathbf{x})\rangle = 0$. Here, U is the magnitude of the nonmagnetic impurity scattering strength and n_0 is the nonmagnetic impurity density.

We employ the nonequilibrium Green's function formalism in order to describe the dynamics of the electrons interacting with both nuclear spins and nonmagnetic impurities. The usefulness of the nonequillibrium Green's function formalism resides in the fact that, the structure of the perturbation expansion is similar to the equilibrium theory, the only difference being the introduction of a contour (see Appendix A for a detailed overview). The diagrammatic formulation of the Keldysh technique is almost identical to the equilibrium diagrammatic formulation, except for the fact that the propagators and vertices contain contour indices [97].

In derivation for the transport equation for the electrons, the central quantity of interest is the electronic Keldysh space Green's function, which can be represented as a matrix in Keldysh space :

$$\underline{G}(1,1') = \begin{bmatrix} G^R(1,1') & G^K(1,1') \\ 0 & G^A(1,1') \end{bmatrix}, \tag{5.13}$$

where we use the abbreviation $1 \equiv (\boldsymbol{x}_1, t_1)$. We note that the matrix elements of the both the Green's function $\underline{G}$ are also matrices in spin space for the specific problem we consider. The diagonal elements of $\underline{G}$, namely G^R and G^A, are the retarded and advanced Green's functions known from the equilibrium theory:

$$G^R(1,1')_{\sigma,\sigma'} = -i\theta(t_1 - t_{1'})\langle\{\psi_\sigma(1), \psi^\dagger_{\sigma'}(1')\}\rangle, \tag{5.14}$$

$$G^A(1,1')_{\sigma,\sigma'} = +i\theta(t_{1'} - t_1)\langle\{\psi_\sigma(1), \psi^\dagger_{\sigma'}(1')\}\rangle, \tag{5.15}$$

where ψ_σ is the field operator for the electrons with spin σ and θ is the Heaviside function. Retarded and advanced Green's functions provide information about the available states, whereas the off-diagonal element of $\underline{G}$, G^K, is the Keldysh Green's function which determines the occupation of the aforementioned states, which is defined as:

$$G^K(1,1')_{\sigma,\sigma'} = -i\langle[\psi_\sigma(1), \psi^\dagger_{\sigma'}(1')]\rangle. \tag{5.16}$$

We seek to introduce the effect of the nonmagnetic impurity scattering, as well as the effect of the nuclear spins, via a perturbation expansion for the Green's function given in Eq. (5.13). Similar to the equilibrium theory, we describe the perturbation expansion via the Dyson equation, which enables us to use the concept of self energy for constructing the Dyson equation. The self energy in Keldysh formulation has the same triangular matrix structure as the Green's function given in Eq. (5.13):

$$\underline{\Sigma}(1,1') = \begin{bmatrix} \Sigma^R(1,1') & \Sigma^K(1,1') \\ 0 & \Sigma^A(1,1') \end{bmatrix}, \tag{5.17}$$

where the $\Sigma^{R(A)}$ is the retarded (advanced) self energy, whereas Σ^{K} is the Keldysh self energy. Each of these self energy components are also matrices in spin space.

The benefit of the self energy is that it allows for a clear way of constructing the Dyson equation. In the nonequilibrium theory, there are actually two Dyson equations (left and right Dyson equations) that contain complete information about the overall system. The derivation of the left and right Dyson equations is beyond the scope of this thesis. Instead, we are going to calculate the self energy for each scattering mechanism (nonmagnetic impurity scattering and nuclear spin scattering) and construct the equation of motion by using the left-right subtracted Dyson equation within the gradient approximation (see Appendix A for a detailed derivation):

$$\partial_t \underline{G} + \frac{v_F}{2}\left\{(\hat{z}\times\boldsymbol{\sigma})\cdot\boldsymbol{\nabla}, \underline{G}\right\} + \frac{i}{\hbar}\left[H_0 + \bar{H}_{hf}, \underline{G}\right] = -\frac{i}{\hbar}\left[\underline{\Sigma}, \underline{G}\right], \tag{5.18}$$

where the term $\bar{H}_{hf}$ describes the average field generated by finite polarization of the nuclear spins, resulting in the precession of the electron spins. In the rest of the calculations, we ignore the precession of the electrons. The effects of both nonmagnetic impurity and nuclear spin scattering are manifested via the electron self energy, which we decompose as $\underline{\Sigma} = \underline{\Sigma}_0 + \underline{\Sigma}_m$.

In principle, the equation of motion for the $\underline{G}$ given in Eq. (5.18) contains the full information about the system. But, we are interested in with the Keldysh component of the equation of motion given in Eq. (5.18), as the Keldysh component yields the information about occupation of the states. Below, we obtain the Keldysh component of Eq. (5.18) and use quasiclassical approximation in order to obtain the transport equations for spin and charge degrees of freedom.

Quasiclassical approximation

The quasiclassical approximation relies on the assumption that all the energy scales of the problem is small compared to the Fermi energy E_F. Here, we make use of this assumption for the surface states of a 3D topological insulators and employ the quasiclassical approximation. We define the quasiclassical Green's function as (see Appendix A):

$$\underline{g}(\boldsymbol{R}, t, \hat{k}, \epsilon) = \frac{i}{\pi}\int d\xi\, \underline{G}(\boldsymbol{R}, t, \boldsymbol{k}, \epsilon), \tag{5.19}$$

where we define $\xi = \hbar v_F k - E_F$. We note that the quasiclassical Green's function g is also a triangular matrix in Keldysh space with the same components (retarded, advanced and Keldysh) with each component being a matrix also in spin space. We emphasize that

the quasiclassical Green's function given in Eq. (5.19) depends on the direction of the momentum, which we denote as $\hat{k}$.

Within the quasiclassical approximation, we obtain the unperturbed retarded and advanced Green's functions for the surface state Hamiltonian H_0 given in Eq. 5.1 as:

$$\begin{aligned} g^{R/A} &= \frac{i}{\pi}\int d\xi \, \left(\epsilon - \hbar v_F \left(\boldsymbol{k}\times\boldsymbol{\sigma}\right)\cdot\hat{z} + E_F \pm i0^+\right)^{-1} \\ &\approx \pm\frac{1}{2}\left(1 + \left(\hat{k}\times\hat{z}\right)\cdot\boldsymbol{\sigma}\right), \end{aligned} \tag{5.20}$$

We note that we regularize the divergent terms in the integral given above by assuming that Fermi energy scale is the largest energy scale in the problem. In this way, we only consider the limit of small energies ($|\epsilon| \ll \hbar v_F k_F$ with k_F being the Fermi wavevector) and obtain Eq. (5.20)

We now use Eq. (5.20) and the relation $\Sigma^R = -\Sigma^A$ (as we show below that this relation holds) in order to obtain the kinetic equation, *i.e.* the Keldysh component of the equation of motion given in Eq. (5.18) within quasiclassical approximation:

$$\begin{aligned} \partial_t g^K + \frac{v_F}{2}\left\{(\hat{z}\times\boldsymbol{\sigma})\cdot\boldsymbol{\nabla}, g^K\right\} + iv_F k_F\left[\left(\hat{k}\times\hat{z}\right)\cdot\boldsymbol{\sigma}, g^K\right] = \\ -\frac{i}{\hbar}\{\Sigma^R, g^K\} + \frac{i}{\hbar}\Sigma^K + \frac{i}{2\hbar}\{(\hat{k}\times\hat{z})\cdot\boldsymbol{\sigma}, \Sigma^K\}. \end{aligned} \tag{5.21}$$

We note that Eq.(5.21) is generic for 3D topological insulators without hexagonal warping and it is the central equation that we need to solve in order to obtain the transport equation for the 3D topological insulators.

To that end, we first disregard the effect of the nuclear spins and obtain the self energy due to nonmagnetic impurity scattering. Later, we shall include the effect of the nuclear spins and derive the transport equations for the overall system, described by the Hamiltonian given in Eq. (5.12).

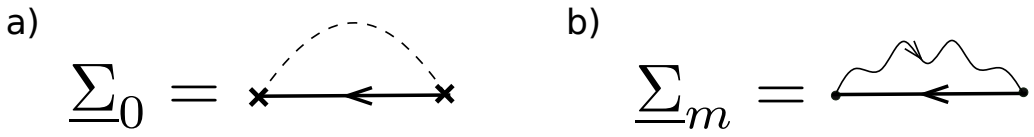

Figure 5.3: a) The self energy for the nonmagnetic impurity scattering. The dashed line indicates the averaging over the positions of the impurities. b) The self energy for the nuclear spin scattering, where the wiggly line is the nuclear spin correlators. The solid circles in b) represent the nuclear spin scattering vertex, whereas the cross in a) represent the nonmagnetic impurity scattering vertex. In both a) and b), the solid line represents the electronic Keldysh space Green's function.

Nonmagnetic impurity scattering

In Fig. 5.3a, we show the self energy diagram for the nonmagnetic impurity scattering. As we consider Gaussian correlated nonmagnetic impurities with zero mean value, we can easily evaluate the self energy in Keldysh space $\underline{\Sigma}_0$:

$$\underline{\Sigma}_0\left(\boldsymbol{R}, t, \epsilon\right) = n_0 U^2 \int \frac{d^2\mathbf{k}}{(2\pi)^2}\, \underline{G}\left(\boldsymbol{R}, t, \boldsymbol{k}, \epsilon\right), \tag{5.22}$$

where we switch to the Wigner representation and use the center of mass time and position $t \equiv (t_1 + t_2)/2$ and $\boldsymbol{R} \equiv (\boldsymbol{x}_1 + \boldsymbol{x}_2)/2$, respectively. In addition, we take the Fourier transform with respect to the relevant coordinates $\eta = t_1 - t_2$ and $\boldsymbol{r} \equiv \boldsymbol{x}_1 - \boldsymbol{x}_2$ (see Appendix A) and represent the Green's function in energy(ϵ)-momentum($\boldsymbol{k}$) domain. Using the definition of the quasiparticle Green's function given in Eq. (5.19), we reexpress the electron self energy due to nonmagnetic impurity scattering as:

$$\underline{\Sigma}_0 = -\frac{i}{\tau_0}\langle \underline{g} \rangle, \tag{5.23}$$

where $\langle g \rangle \equiv \int d\hat{k}'/(2\pi)\, g$ denotes the angular average over the Fermi circle. Moreover, τ_0 is the time scale related to this scattering mechanism is denoted by $\tau_0 = (\pi\nu(E_F) n_0 U^2)^{-1}$, where $\nu(E_F) = E_F/(2\pi\hbar^2 v_F^2)$ is the density of states at the Fermi energy. We note that the elastic mean free path associated with the nonmagnetic impurity scattering is $\ell_{\mathrm{el}} = v_F \tau_0$.

Each element of the self energy matrix given in Eq. (5.23) is obtained by calculating the quasiclassical Green's function. By using the retarded/advanced quasiclassical Green's function given in Eq. (5.20), we obtain the retarded/advanced self energy due to nonmagnetic impurity scattering as:

$$\Sigma_0^{R/A} = \mp \frac{i}{2\tau_0}. \tag{5.24}$$

On the other hand, the Keldysh component of the self energy matrix enters the kinetic equation as $\Sigma_0^K = -i\langle g^K \rangle/\tau_0$.

Nuclear spin scattering

Next, we focus on the electron self energy arising from the interaction with the nuclear spins. We show the diagrammatic representation of the self energy due to nuclear spin scattering in Fig. 5.3b. Even though the nuclear spins have no energetic dynamics similar to the case of nonmagnetic impurities, they still feature spin dynamics. Therefore, we first

need to obtain the nuclear spins correlators, which we define as:

$$iD_{\alpha\beta}(1,2) = \langle \mathcal{T}_c \left(I_\alpha^{n_1}(t_1) I_\beta^{n_2}(t_2) \right) \rangle, \tag{5.25}$$

where we use the same abbreviation $1 \equiv (t_1, \boldsymbol{x}_1)$ we used for electron Green's function. Here $\mathcal{T}_c$ denotes the contour ordering (see Appendix A). We note that throughout the rest of the calculation, we consider two-point correlators for the nuclear spins only and ignore the higher order terms.

We then map the contour ordered nuclear spin correlators given in Eq. (5.25) onto the Keldysh space and find each element of the nuclear spin correlators as:

$$iD_{\alpha\beta}^{\pm\mp}(1,2) = \delta_{n_1,n_2} \left(\delta_{\alpha\beta} \pm i\epsilon_{\alpha\beta\gamma} m_\gamma^{n_1} - m_\alpha^{n_1} m_\beta^{n_2} \right), \tag{5.26}$$

$$iD_{\alpha\beta}^{\mp\mp}(1,2) = \delta_{n_1,n_2} \left(\delta_{\alpha\beta} \pm \text{sign}(t_1 - t_2) i\epsilon_{\alpha\beta\gamma} m_\gamma^{n_1} - m_\alpha^{n_1} m_\beta^{n_2} \right), \tag{5.27}$$

where we define $m_\alpha^n \equiv \langle I_\alpha^n \rangle$. We note that we represent the position of the i^{th} nuclear spin via n_i. In the rest of the calculations, we consider only on-site correlations and assume low nuclear spin density.

Next, we calculate the self energy for electrons due to their interaction with the nuclear spins. We consider two-point correlators for the nuclear spins only and obtain the components of the self energy matrix $\underline{\Sigma}_m$ as:

$$\begin{aligned}
\Sigma_m^{--}(\boldsymbol{R}, \boldsymbol{k}, t_1, t_2) &= +i\frac{\lambda^2}{4} \int \frac{d^2\mathbf{k}'}{(2\pi)^2} \sigma_\alpha G^{--}(\boldsymbol{R}, \boldsymbol{k}', t_1, t_2) \sigma_\beta D_{\alpha\beta}^{--}(\boldsymbol{R}, \boldsymbol{k} - \boldsymbol{k}', t_1, t_2), \\
\Sigma_m^{++}(\boldsymbol{R}, \boldsymbol{k}, t_1, t_2) &= +i\frac{\lambda^2}{4} \int \frac{d^2\mathbf{k}'}{(2\pi)^2} \sigma_\alpha G^{++}(\boldsymbol{R}, \boldsymbol{k}', t_1, t_2) \sigma_\beta D_{\alpha\beta}^{++}(\boldsymbol{R}, \boldsymbol{k} - \boldsymbol{k}', t_1, t_2), \\
\Sigma_m^{-+}(\boldsymbol{R}, \boldsymbol{k}, t_1, t_2) &= -i\frac{\lambda^2}{4} \int \frac{d^2\mathbf{k}'}{(2\pi)^2} \sigma_\alpha G^{-+}(\boldsymbol{R}, \boldsymbol{k}', t_1, t_2) \sigma_\beta D_{\alpha\beta}^{+-}(\boldsymbol{R}, \boldsymbol{k} - \boldsymbol{k}', t_1, t_2), \\
\Sigma_m^{+-}(\boldsymbol{R}, \boldsymbol{k}, t_1, t_2) &= -i\frac{\lambda^2}{4} \int \frac{d^2\mathbf{k}'}{(2\pi)^2} \sigma_\alpha G^{+-}(\boldsymbol{R}, \boldsymbol{k}', t_1, t_2) \sigma_\beta D_{\alpha\beta}^{-+}(\boldsymbol{R}, \boldsymbol{k} - \boldsymbol{k}', t_1, t_2).
\end{aligned} \tag{5.28}$$

We emphasize that the elements of the self energy matrix given in Eq. (5.28) is written in a different basis than the one we use in description of the electronic Green's function. To that end, we switch to the retarded, advanced and Keldysh representation of the self energy given in Eq. (5.28). We start with transforming the the nuclear spin correlators given in Eq. (5.26) into retarded, advanced and Keldysh representation:

$$iD_{\alpha\beta}^{R}(1,2) = \theta(t_1 - t_2) 2i\delta_{n_1,n_2} \epsilon_{\alpha\beta\gamma} m_\gamma^{n_1}, \tag{5.29}$$

$$iD^{A}_{\alpha\beta}(1,2) = -\theta(t_2 - t_1) 2i\delta_{n_1,n_2}\epsilon_{\alpha\beta\gamma} m^{n_1}_{\gamma}, \tag{5.30}$$

$$iD^{K}_{\alpha\beta}(1,2) = 2\delta_{n_1,n_2}\left(\delta_{\alpha\beta} - m^{n_1}_{\alpha} m^{n_2}_{\beta}\right). \tag{5.31}$$

For brevity, we use the matrix representation which we denote as $\underline{D}$, with a similar structure to the electron Green's function given in Eq. (5.13). We then transform all the elements of the self energy given in Eq. (5.28) into retarded, advanced and Keldysh components. We find them within the quasiclassical approximation to be:

$$\Sigma^{R/A}_{m}(\boldsymbol{R}, \boldsymbol{k}, t_1, t_2) = \frac{\lambda^2}{8}\pi\nu(E_F)\int \frac{d\hat{k}'}{2\pi}\Big[\sigma_i\, g^{K}(\boldsymbol{R}, \boldsymbol{k}', t_1, t_2)\,\sigma_j\, D^{R/A}_{ij}(\boldsymbol{R}, \boldsymbol{k} - \boldsymbol{k}', t_1, t_2), + \sigma_i\, g^{R/A}(\boldsymbol{R}, \boldsymbol{k}', t_1, t_2)\,\sigma_j\, D^{K}_{ij}(\boldsymbol{R}, \boldsymbol{k} - \boldsymbol{k}', t_1, t_2)\Big] \tag{5.32}$$

$$\Sigma^{K}_{m}(\boldsymbol{R}, \boldsymbol{k}, t_1, t_2) = \frac{\lambda^2}{8}\pi\nu(E_F)\int \frac{d\hat{k}'}{2\pi}\Big[\sigma_i\, g^{K}(\boldsymbol{R}, \boldsymbol{k}', t_1, t_2)\,\sigma_j\, D^{K}_{ij}(\boldsymbol{R}, \boldsymbol{k} - \boldsymbol{k}', t_1, t_2) + \sigma_i\,\left(g^{R} - g^{A}\right)(\boldsymbol{R}, \boldsymbol{k}', t_1, t_2)\,\sigma_j\,\left(D^{R}_{ij} - D^{A}_{ij}\right)(\boldsymbol{R}, \boldsymbol{k} - \boldsymbol{k}', t_1, t_2)\Big], \tag{5.33}$$

where we use a mixed representation involving $\boldsymbol{R}$ and momentum $\boldsymbol{k}$, as well as the temporal coordinates t_1 and t_2 . We now use the nuclear spin correlators given in Eq. (5.29), and obtain the explicit form of the self energy as:

$$\Sigma^{R/A}_{m} = \frac{\hbar}{\tau_{sf}}\Big[\sigma_i\,\langle g^{K}\rangle\,\sigma_j\,\left(\pm\theta(\pm(t_1 - t_2))\epsilon_{ijk}m_k\right) + \sigma_i\,\langle g^{R/A}\rangle\,\sigma_j\,\left(-i\delta_{ij}\right)\Big], \tag{5.34}$$

$$\Sigma^{K}_{m} = \frac{\hbar}{\tau_{sf}}\Big[\sigma_i\,\langle g^{K}\rangle\,\sigma_j\,\left(-i\delta_{ij}\right) + \sigma_i\,\left(\langle g^{R}\rangle - \langle g^{A}\rangle\right)\,\sigma_j\,\left(\epsilon_{ijk}m_k\right)\Big], \tag{5.35}$$

where we define a timescale $\tau^{-1}_{sf} \equiv \frac{\lambda^2}{4\hbar}n_m\pi\nu(\epsilon_F)$ associated with the mean nuclear spin polarization dynamics. We note that we use a coarse grained description of the local mean nuclear spin polarization, namely $m_n \to m(\boldsymbol{R})$.

As the self energy components given in Eq. (5.34) are matrices within the spin subspace, we parametrize the quasiclassical Green's function as $g^K = g_0\sigma_0 + \boldsymbol{g}\cdot\boldsymbol{\sigma}$. We assume that the nuclear spin correlators are independent of momentum and energy. We obtain:

$$\Sigma^{R/A}_{m} = \mp\frac{i\hbar}{\tau_{sf}}\Big[\frac{3}{2}\sigma_0 + \langle\boldsymbol{g}\rangle\cdot\boldsymbol{m}\sigma_0 - \langle g_0\rangle\boldsymbol{m}\cdot\boldsymbol{\sigma}\Big],$$

$$\Sigma^{K}_{m} = -\frac{i\hbar}{\tau_{sf}}\Big[3\langle g_0\rangle\sigma_0 - \langle\boldsymbol{g}\rangle\cdot\boldsymbol{\sigma} - 2\boldsymbol{m}\cdot\boldsymbol{\sigma}\Big], \tag{5.36}$$

where we use $\langle g^{R/A}\rangle = \pm 1/2$. We note that we omit the arguments of the self energy

components, namely the position $\boldsymbol{R}$, time T and energy ϵ. Furthermore, $\Sigma^{R/A}$ contain terms that arise from the Fourier transformation with respect to the relative time coordinate $\eta = t_1 - t_2$, which describe the nuclear spin mediated electron-electron interaction. We ignore these terms as their contribution is not signifacant compared to the electron dynamics.

The nonmagnetic impurity averaged self energy given in Eq. (5.23) and the nuclear spin self energy given in Eq. (5.36) allow us to determine the right hand side of Eq. (5.21), which we separate into two parts $I[g] = I_0[g] + I_m[g]$, each of which is given as

$$I_0[g] = -\frac{1}{\tau_0}\left[g - \langle g\rangle - \frac{1}{2}\{(\hat{k}\times\hat{z})\cdot\sigma, \langle g\rangle\}\right]. \tag{5.37}$$

and

$$\begin{aligned} I_m[g] = -\frac{3}{\tau_{sf}}\Bigg[&g - \langle g_0\rangle\sigma_0 + \frac{2}{3}\langle \boldsymbol{g}\rangle\cdot\boldsymbol{m}g - \frac{2}{3}\langle g_0\rangle \boldsymbol{m}\cdot\boldsymbol{\sigma}g_0 - \frac{2}{3}\langle g_0\rangle\boldsymbol{m}\cdot\boldsymbol{g}\sigma_0 + \frac{1}{3}\langle\boldsymbol{g}\rangle\cdot\boldsymbol{\sigma} \\ &+ \frac{2}{3}\boldsymbol{m}\cdot\boldsymbol{\sigma} - \langle g_0\rangle\left(\hat{k}\times\hat{z}\right)\cdot\boldsymbol{\sigma} + \frac{1}{3}\left(\hat{k}\times\hat{z}\right)\cdot\langle\boldsymbol{g}\rangle\sigma_0 + \frac{2}{3}\boldsymbol{m}\cdot\left(\hat{k}\times\hat{z}\right)\sigma_0\Bigg]. \end{aligned} \tag{5.38}$$

We insert Eq. (5.37) and Eq. (5.38) into Eq. (5.21) and consequently, we obtain the quantum kinetic equation, which we use to derive the transport equations for the surface states.

Transport equations for the surface states

The form of the Hamiltonian for the surface states (Eq. (5.1)) suggests that the transport equations for the spin and charge degrees of freedom are coupled. As a first step in deriving the transport equations for the surface states, we take the spin traces of Eq. (5.21). We start with the σ_0 trace and obtain:

$$\begin{aligned} \partial_t g_0 + v_F\hat{k}\cdot\boldsymbol{\nabla}g_0 = -\frac{1}{\tau_0}\left[g_0 - \langle g_0\rangle + \left(\hat{k}\times\langle\boldsymbol{g}\rangle\right)_z\right] - \frac{3}{\tau_{sf}}\Bigg[&g_0 - \langle g_0\rangle - \frac{1}{3}\left(\hat{k}\times\langle\boldsymbol{g}\rangle\right)_z \\ &+ \frac{2}{3}\boldsymbol{m}\cdot\left(g_0\langle\boldsymbol{g}\rangle - \langle g_0\rangle\boldsymbol{g} + (\hat{k}\times\hat{z})\right)\Bigg]. \end{aligned} \tag{5.39}$$

It is straightforward to obtain $\boldsymbol{\sigma}$ traces (see Appendix H). We now focus on a nonequilibrium state such that g is diagonal in the eigenstates of H_0 [95]. In this case, only the states that are in the upper band contributes to g, hence at zeroth order we have $\boldsymbol{g} = g_0(\hat{k}\times\hat{z})$

with each element given by:

$$g_x = \hat{k}_y g_0, \tag{5.40}$$

$$g_y = -\hat{k}_x g_0. \tag{5.41}$$

At this point, we assume that the nonmagnetic impurity scattering is the dominant source of scattering and ignore the contribution of the nuclear spins at first. In this case, we use Eq. (5.40) and obtain the subdominant term g_z as:

$$g_z \approx \frac{1}{2v_F k_F}\left(\frac{\hat{k}_x}{\tau_0}\langle \hat{k}_y g_0\rangle - \frac{\hat{k}_y}{\tau_0}\langle \hat{k}_x g_0\rangle + v_F \hat{k}_y \nabla_x g_0 - v_F \hat{k}_x \nabla_y g_0\right), \tag{5.42}$$

where we see that the term g_z is only nonzero for the first order in $(k_F \ell_{\text{el}})^{-1}$. We note that we consider a scenario for which spin transport is not diffusive. Therefore, we do not consider the first order corrections to Eq. (5.40). We now insert this set of equations back into Eq. (5.39) and we have

$$\begin{aligned}\partial_t g_0 + v_F \nabla \cdot \hat{k} g_0 = &-\frac{1}{\tau_0}\left[g_0 - \langle g_0\rangle - \hat{k}\cdot\langle \hat{k}' g_0\rangle\right] - \frac{3}{\tau_{sf}}\left[g_0 - \langle g_0\rangle + \frac{1}{3}\hat{k}\cdot\langle \hat{k}' g_0\rangle\right. \\ &\left. + \frac{2}{3}\boldsymbol{m}\cdot\left(g_0\langle g_0(\hat{k}'\times\hat{z})\rangle - \langle g_0\rangle g_0(\hat{k}\times\hat{z}) + (\hat{k}\times\hat{z})\right)\right].\end{aligned} \tag{5.43}$$

This is the quantum kinetic equation for the charge sector of the surface states, interacting with both nonmagnetic impurities and nuclear spins. The quantum kinetic equations for the spin sector are demonstrated in Appendix H. We then take the angular average over the quantum kinetic equation and obtain the transport equation for the charge sector:

$$\partial_t n + 2v_F\left(\boldsymbol{\nabla}\times\boldsymbol{s}\right)\cdot\hat{z} = 0, \tag{5.44}$$

and for the spin sector:

$$\partial_t s_x + \frac{v_F}{4}\nabla_y n + \frac{s_x}{2\tau_0} = \Gamma_x, \tag{5.45}$$

$$\partial_t s_y - \frac{v_F}{4}\nabla_x n + \frac{s_y}{2\tau_0} = \Gamma_y, \tag{5.46}$$

where we use the generalized density matrix $F(\epsilon, \boldsymbol{R}) = n(\epsilon, \boldsymbol{R})/2\sigma_0 + \boldsymbol{s}(\epsilon, \boldsymbol{R})\cdot\boldsymbol{\sigma}$, associated with the angular average of the quasiclassical Keldysh Green's function. Here, we define Γ_i as the nuclear spin contribution to the diffusion equation:

$$\Gamma_x = -\frac{1}{\tau_{sf}}\left[s_x - m_x\left(\frac{n}{2}\left(1-\frac{n}{2}\right) + s_x^2\right)\right], \tag{5.47}$$

$$\Gamma_y = -\frac{1}{\tau_{sf}}\left[s_y - m_y\left(\frac{n}{2}\left(1-\frac{n}{2}\right)+s_y^2\right)\right], \tag{5.48}$$

where we redefine the timescale $4\tau_{sf} \equiv \tau_{sf}$. We note that in the absence of nuclear spin scattering, the terms Γ_i vanish. In this case, we recover the results obtained by Ref. [95].

We explore the case where the transport is dominated by the nonmagnetic impurity scattering, $\tau_0 \ll \tau_{sf}$. In this case, the transport is diffusive and we solve the transport equations in this limit. We focus on the quasistationary state ($\omega\tau \ll 1$) and take the nonmagnetic impurity scattering as the dominant source of scattering. In the lowest order, we have:

$$s_{x(y)} = \mp\frac{v_F\tau_0}{2}\nabla_{y(x)}n + 2\tau_0\Gamma_{x(y)}. \tag{5.49}$$

We insert Eq. (5.49) into the continuity equation given in Eq. (5.44) and we obtain an energy resolved diffusion equation:

$$\partial_t n - D\nabla^2 n + 4\ell_{\text{el}}\left(\boldsymbol{\nabla}\times\boldsymbol{\Gamma}\right)\cdot\hat{z} = 0, \tag{5.50}$$

where we define $D = v_F^2\tau_0$ as the diffusion constant [95]. We identify the energy resolved particle current density as $\boldsymbol{j}(\epsilon, \boldsymbol{R}) = -D\nabla n + 4\ell_{\text{el}}(\hat{z}\times\boldsymbol{\Gamma})$. Complementary to the electron dynamics, we next obtain the nuclear spin dynamics and identify the term $\boldsymbol{\Gamma}$.

Nuclear spin polarization dynamics and induced current

We now obtain the dynamics of the nuclear spin polarization under the influence of nonequilibrium electron spin polarization and establish the connection between the source term $\boldsymbol{\Gamma}$ in Eq. (5.50).

We first consider the nuclear spin self energy, which we denote as Π, which takes into account the effect of the electrons on the nuclear spins. We obtain the nuclear spin self energy Π as follows:

$$\Pi^{-+}_{\alpha\beta}(1,2) = -i\frac{\lambda^2}{4}\,\text{Tr}\left[\sigma_\alpha G^{-+}(1,2)\sigma_\beta G^{+-}(2,1)\right], \tag{5.51}$$

where the trace is over the spin degree of freedom. Here, we use the lesser (greater) component of the electronic Green's function, namely $G^{-+}(G^{+-})$, for convenience. We emphasize that the Keldysh representation of the electronic Green's function is related to the representation we use here via a linear transformation (see Appendix A).

In Fig. 5.4, we show the diagrammatic representation of the lesser component of the self energy. We switch to the Wigner representation for Π^{-+} and then apply Fourier transformation with respect to the relative coordinates, we have:

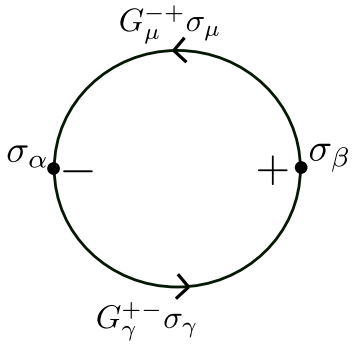

Figure 5.4: The diagrammatic representation for the lesser component of the nuclear spin self energy $\Pi^{-+}_{\alpha\beta}$.

$$\Pi^{-+}_{\alpha\beta}(\boldsymbol{q},\Omega) = -i\frac{\lambda^2}{4}\int\frac{d^2\boldsymbol{k}}{(2\pi)^2}\int\frac{d\omega}{2\pi}\,\mathrm{Tr}\left[\sigma_{\alpha}G^{-+}(\boldsymbol{k},\omega)\sigma_{\beta}G^{+-}(\boldsymbol{k}-\boldsymbol{q},\omega-\Omega)\right]. \quad (5.52)$$

We proceed by parametrizing the electronic Green's function, namely $G \equiv G_{\mu}\sigma_{\mu}$ with $\mu = \{0, x, y, z\}$ and calculate the lesser and greater components of the nuclear spin self energy (see Appendix H).

Next, we focus on the quantum kinetic equation for the lesser components of the momentum integrated nuclear spin correlator, $d^{-+}_{\alpha\beta}$ (see Appendix H):

$$\dot{d}^{-+}_{\alpha\beta}(\boldsymbol{r},t) = -\frac{i}{\hbar}\left(\pi^{-+}_{\alpha\delta}d^{+-}_{\delta\beta}(\boldsymbol{r},t) - \pi^{+-}_{\alpha\delta}d^{-+}_{\delta\beta}(\boldsymbol{r},t)\right), \quad (5.53)$$

where the term on the right hand side describes the spin-flip interaction taking place between nuclear spins and electron spins. Here, $\pi^{\mp\pm}$ describes the nuclear spin self energy components, integrated over the momentum $\boldsymbol{q}$ (see Appendix H). We then insert the nuclear spin self energy into Eq. (5.53) and obtain the equation for the nuclear spin polarization dynamics. For the $x-$component, we have:

$$\dot{m}_x(\boldsymbol{r},t) = -\frac{\lambda^2\epsilon_F^2}{4\pi(\hbar v_F)^4}\int\frac{d\epsilon}{\hbar}\,m_x(\boldsymbol{r})\left(\frac{n(\epsilon,\boldsymbol{r})}{2}\left(1-\frac{n(\epsilon,\boldsymbol{r})}{2}\right)+s_x^2(\epsilon,\boldsymbol{r})\right) - s_x(\epsilon,\boldsymbol{r}), \quad (5.54)$$

where we use the relation $d^{-+}_{\alpha\beta} = \epsilon_{\alpha\beta\gamma}m_{\gamma}(\boldsymbol{r})$ (see Eq. (5.26)) for the case $\alpha \neq \beta$ and consider a coarse grained description and define the average nuclear spin polarization $\boldsymbol{m}(\boldsymbol{r})$. Furthermore, we make use of the generalized density matrix $F(\epsilon,\boldsymbol{r}) =$

$n(\epsilon, \boldsymbol{r})/2\sigma_0 + \boldsymbol{s}(\epsilon, \boldsymbol{r}) \cdot \boldsymbol{\sigma}$. Similarly, we find the $y-$component of the magnetization to be:

$$\dot{m}_y(\boldsymbol{r}, t) = -\frac{\lambda^2 \epsilon_F^2}{4\pi(\hbar v_F)^4} \int \frac{d\epsilon}{\hbar}\, m_y(\boldsymbol{r}) \left(\frac{n(\epsilon, \boldsymbol{r})}{2} \left(1 - \frac{n(\epsilon, \boldsymbol{r})}{2} \right) + s_y^2(\epsilon, \boldsymbol{r}) \right) - s_y(\epsilon, \boldsymbol{r}). \tag{5.55}$$

We note that the equations for the nuclear spin polarization dynamics given in Eq. (5.54) and Eq. (5.55) are generic for the Fermi contact interaction, whereas the density of states and the electron spin density vary depending on the electronic part of the Hamiltonian. To that end, we incorporate the effect of the surface states of the 3D topological insulator via the electron density matrix and establish the connection between the nuclear spin dynamics and the source term $\boldsymbol{\Gamma}$ in the diffusion equation given in Eq. (5.50). We identify the integrand in the right hand side of Eq. (5.54) and Eq. (5.55) as the source term Γ_x and Γ_y, respectively. We find it insightful to express the nuclear spin dynamics in a more compact form as:

$$\frac{d\mathbf{m}}{dt} = -\nu \int d\epsilon\, \boldsymbol{\Gamma}, \tag{5.56}$$

where we define $\mathbf{m}(\boldsymbol{r}) \equiv n_m \boldsymbol{m}(\boldsymbol{r})$ as the nuclear spin polarization density. We note that the energy integral of the source term $\boldsymbol{\Gamma}$ is related to the time rate of change of mean nuclear spin polarization density $\mathbf{m}$. We stress that Eq. (5.56) is generic for the dynamics of nuclear spin polarization interacting with the electron spins via Fermi contact interaction, while the term $\boldsymbol{\Gamma}$ is specific for the system under consideration.

We now integrate Eq. (5.50) over energy and use Eq. (5.56) to obtain the diffusion equation for the charge density:

$$\partial_t \rho - D\nabla^2 \rho + 2e\ell_{\text{el}} \boldsymbol{\nabla} \cdot \left(\frac{d\mathbf{m}}{dt} \times \hat{z} \right) = 0, \tag{5.57}$$

where we define the charge density as $\rho \equiv -e\nu/2 \int d\epsilon\, n + \nu e^2 \phi$, where ϕ is the scalar electrostatic field. We find the charge current density from the diffusion equation given in Eq. (5.57) as

$$\boldsymbol{J}(\boldsymbol{r}, t) = -D\boldsymbol{\nabla}\rho + 2e\ell_{\text{el}} \left(\frac{d\mathbf{m}}{dt} \times \hat{z} \right), \tag{5.58}$$

where we identify the time rate of change of the nuclear spin polarization density $\mathbf{m}$ as a charge current source due to the spin-momentum locking feature of the surface states.

We now demonstrate the effect of the nuclear spin polarization dynamics in a setup depicted in Fig. 5.5, where two reservoirs are connected to a 3D topological insulator. We

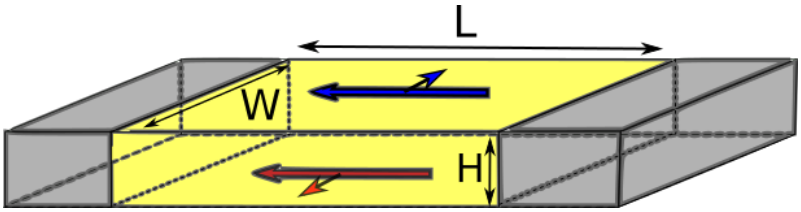

Figure 5.5: The schematic description of the transport setup involving a 3D topological insulator (yellow) and metallic leads (gray) that are connected to reservoirs. The charge carriers for top and bottom surfaces are polarized in the opposite direction, in response to a charge current flowing through each surface.

focus only on the top surface and assume that the top and bottom surface states do not hybridize. For the sake of demonstration, we assume that the nuclear spin polarization density $\mathfrak{m}$ has a weak position dependence and hence, we take only take its position independent contribution into account.

We first consider a case where we apply a voltage bias between the reservoirs, therefore, we have a charge current flowing in the $x-$direction. In this case, we have a one-dimensional diffusion equation, which we solve for and obtain the charge current as:

$$I = GV + 2eN\frac{\ell_{\rm el}}{L}\frac{dm_y}{dt}, \tag{5.59}$$

where we use the relation $I = JW$. The first term on the right hand side represents the usual Ohm's law with conductance $G = \sigma W/L$, where $\sigma = e^2\nu D$ is the conductivity given by the Einstein's relation (not to be confused with Pauli matrices in spin space), whereas the second term is the nuclear spin dynamics induced charge current. Here, N is the total number of nuclear spins at the surface of a 3D topological insulator and m_y is the average nuclear spin polarization in the $y-$direction.

We obtain the explicit form of the induced charge current due to nuclear spin dynamics by solving Eq. (5.55) under an applied voltage bias:

$$\frac{dm_y}{dt} = \frac{\gamma_0^{3D}}{\hbar}\left(\frac{\ell_{\rm el}}{L}eV - m_y\left(\frac{\ell_{\rm el}}{L}eV\coth\left(\frac{\ell_{\rm el}}{L}\frac{eV}{2k_BT}\right)\right)\right), \tag{5.60}$$

where we assume that nuclear spins are polarized in the $y-$direction only. We now insert Eq. (5.60) into Eq. (5.59) and obtain the current-voltage characteristics of the 3D topological insulator in the presence of a Maxwell's demon memory:

$$I = GV + 2eN\frac{\ell_{\rm el}}{L}\frac{\gamma_0^{3D}}{\hbar}\left(\frac{\ell_{\rm el}}{L}eV - m_y\left(\frac{\ell_{\rm el}}{L}eV\coth\left(\frac{\ell_{\rm el}}{L}\frac{eV}{2k_BT}\right)\right)\right), \tag{5.61}$$

where we identify the effective interaction strength $\gamma_0^{3D} \equiv \lambda^2\nu^2/4$ as defined in Eq. (5.11).

We focus on the work extraction phase. In the absence of an applied voltage bias, the first

term in Eq. (5.59) vanishes. However, we find that a finite nuclear spin polarization m_y induces a charge current:

$$I_{\text{MD}} = -eN\frac{\ell_{\text{el}}}{L}\frac{m_y}{\tau_m}, \tag{5.62}$$

where we identify the characteristic time scale τ_m given in Eq. (5.11), entering the nuclear spin polarization induced charge current equation in the diffusive limit as well. The nonzero charge current due to finite nuclear spin polarization demonstrates that the Maxwell's demon effect is still valid in the diffusive regime. However, the magnitude of the Maxwell's demon induced current is scaled by the ratio of ℓ_{el}/L in the diffusive regime, as opposed to the quantum spin Hall insulator case. We stress that this inefficiency is due to the randomization of the spin of the carriers due to nonmagnetic impurity scattering.

5.4 Conclusion

In conclusion, we investigated the 3D topological insulator from the perspective of quantum information engine implementation based on the interaction of spin-momentum locked charge carriers with the nuclear spins and/or magnetic impurity spins. As opposed to their 2D counterparts, the transport at the surface of 3D topological insulator can be diffusive for systems longer than the elastic mean free path ℓ_{el}. For that reason, we first focused only on the nuclear spins interacting with the spin-momentum locked surface states and established that 3D topological insulators can be used as platforms to realize Maxwell's demon implementation, similar to the quantum information engine based on a 2D topological insulator that we discussed in Chapter 3. On the other hand, in the diffusive limit, the momentum relaxation due to disorder is accompanied by the randomization of the spin of charge carriers due to the helical nature of the surface states, decreasing the efficiency of the conversion of the information entropy of the nuclear spin subsystem into electrical work. To that end, we studied the effect of the disorder, caused by nonmagnetic impurity scattering, and obtained the quantum kinetic equation using Keldysh formalism and derived the diffusion equation for the electrons at the surface of a 3D topological insulator. We found that the Maxwell's demon effect still survives for devices longer than the mean free path. However, as opposed to the ballistic case, the magnitude of the induced current (or similarly the induced voltage) is reduced by a factor of ℓ_{el}/L.

Chapter 6

A BRIEF INTRODUCTION TO TOPOLOGICAL SUPERCONDUCTORS

The topological classification scheme relies on having a band gap in the energy spectrum. Historically, the classification of insulators based on their topological properties started with quantum Hall insulators, discovery of quantum spin Hall insulators [98] and 3D topological insulators [91, 92] came afterwards. It was soon discovered that the topological classification can be extended for superconductors, as they also feature an energy gap for quasiparticle excitations in their single-particle band description. Similar to the topological insulators, the topological classification of the superconductors is based on the symmetry and dimensionality [99, 100]. For a comprehensive review on topological superconductors and their classification based on topological invariants, we direct the reader to Ref. [72].

Of particular interest is the time-reversal symmetry breaking topological superconductors, for which a topologically nontrivial bulk structure that promotes the emergence of quasiparticle excitations, named Majorana zero modes, within the superconducting gap [101–111]. The interest in Majorana zero modes in topological superconductors stems from their non-Abelian exchange statistics that is crucial for topological quantum computation [71, 72, 112–115]. A pair of spatially separated Majorana zero modes constitute a topologically protected qubit, where the information is stored nonlocally. As a result, the Majorana qubit is immune to local sources of decoherence.

We start our discussion by considering the simplest Bogoliubov–de Gennes Hamiltonian describing a topological superconductor, which is the Hamiltonian of a spinless super-

conductor. As the fermionic statistics only allow for antisymmetric pairing potentials, the antisymmetry of the superconducting pairing potential for a spinless superconductor is manifested in its real space structure. In other words, the superconducting pairing potential must be proportional to the momentum, and in the lowest order in momentum, we have a *p*-wave pairing potential:

$$H_p = h(\mathbf{p}, \mathbf{r})\, \tau_z + \Delta' \boldsymbol{\tau} \cdot \mathbf{p}, \tag{6.1}$$

where τ_i are the Pauli matrices in particle-hole space ($i = x, y, z$), Δ' is the *p*-wave pairing potential strength, $h(\mathbf{p}, \mathbf{r}) = (p^2/2m + V(\mathbf{r}) - \mu)$ is the spinless normal state Hamiltonian with chemical potential μ and $V(\mathbf{r})$ is the single-particle scalar potential, characterizing the disorder and confinement potentials.

The one dimensional version of the *p*-wave topological superconductor given in Eq. (6.1) corresponds to continuum version of the original proposal of Kitaev [112], setting the Majorana zero modes at the ends. The 2D version, also known as *p+ip* superconductor, hosts Majorana zero modes localized at the vortices.

However, except for rare cases, superconductors in nature feature *s*-wave pairing, where electrons of opposite spins constitute Cooper pairs. As a result, spin degeneracy prevents the realization of the topologically nontrivial phase. Nevertheless, it has been established that it is still possible to utilize *s*-wave superconductors to engineer the Hamiltonian for *p*-wave superconductors [116, 117]. This is achieved by combination of spin-orbit coupling, external magnetic field and *s*-wave superconductor.

We focus on a general setting where we consider a 2D semiconductor system with Rashba spin-orbit coupling proximity coupled to a superconductor under a magnetic field, whose dynamics are given by the Bogoliubov–de Gennes Hamiltonian [118]

$$H_s = h(\mathbf{p}, \mathbf{r})\, \tau_z + \alpha(p_x \sigma_y - p_y \sigma_x)\tau_z + B\sigma_x + \Delta\tau_x, \tag{6.2}$$

where σ_i are the Pauli matrices in spin space ($i = x, y, z$), α is the Rashba spin-orbit coupling strength, B is the Zeeman energy and Δ is the *s*-wave pair potential. For the one dimensional version of Eq. (6.2), high enough Zeeman energy splits opposite spins. In this case, the system is effectively described by a one dimensional spinless *p*-wave superconductor given in Eq. (6.1), with an effective *p*-wave pair potential strength given by $\Delta' = \alpha\, \Delta/\epsilon$ with $\epsilon = \sqrt{B^2 - \Delta^2}$ for $B > \Delta$ [116, 117].

In the next chapter, we shall investigate the ground state fermion parity switches in topological superconductors, whose dynamics are described by the Hamiltonian H_s [H_p] "*s*-wave" ["*p*-wave"] topological superconductor.

Chapter 7

FERMION PARITY CROSSINGS STATISTICS AND SCARS IN MAJORANA BILLIARDS

The ground state fermion parity of conventional superconductors can switch from even fermion parity to odd fermion parity under certain conditions. This switch is known as fermion parity switch (or crossing) and this level crossing is protected because the parity is a conserved quantity and the crossings indicate a topological phase transition [100–111]. The degenerate states at the crossing point are Majorana zero modes, which are governed by non-Abelian statistics [71, 72, 112–115].

Experimentally observed zero-bias conductance peaks in tunneling differential conductance measurements on semiconductor nanowires with proximity-induced superconductivity signifies the existence of topologically nontrivial Majorana zero modes bound to the edges [119–122]. However, the physical origin of zero-bias conductance peaks is not yet conclusive. Several different mechanism, such as Andreev bound states [109, 110, 123–140], Kondo effect, weak antilocalization, and disorder [107, 141–150] were proposed to explain the zero-bias conductance peaks. Therefore, an alternative approach is needed to identify Majorana zero modes in proximity coupled nanowires. Sequences of fermion parity crossings have been considered to be the smoking gun evidence of the presence of a pair of Majorana bound states localized at the edges of a ballistic one dimensional wire [151, 152]. Such sequences of fermion parity crossings, as a function of the applied magnetic field and chemical potential, were observed in recent experiments on semiconductor nanowires with proximity-induced superconductivity [137, 138].

In this chapter, we study the fermion parity crossings in arbitrarily shaped Majorana bil-

liards within the framework of spectral geometry, semiclassical physics and random matrix theory. The fermion parity crossings in Majorana billiards appear as an external parameter (magnetic field B or chemical potential μ) of the system is varied. The set of points at which fermion parity crossings occur is called the fermion parity crossing spectrum. We demonstrate that the spectrum of fermion parity crossings in topological superconductors can be obtained by solving a corresponding normal state eigenvalue problem. Subsequently, the mapping allows us to use all the tools from semiclassical physics in order to obtain properties of the fermion parity crossing spectrum. In this way, we relate the properties of this spectrum to the geometrical shape of the Majorana billiard. We note that this relation is reminiscent to Kac's famous question (as phrased by L. Bers), "Can one hear the shape of a drum?" [153]. Therefore, we establish that "One can hear the shape of a Majorana Billiard" by investigating "the spectrum of topological phase transitions".

This chapter is organized as follows: In Sec. 7.1, we introduce the Majorana billiards and define the fermion parity crossing spectrum. In Sec. 7.2, we show that the average density of fermion parity crossings of a Majorana billiard is related to its geometrical shape. In addition, we derive a scaling property of fermion parity crossings for *s*-wave Majorana billiards. We also show that disordered Majorana billiards feature nonzero density of fermion parity crossings below the clean-system topological phase transition, analogous to Lifshitz tails in disordered systems. In Sec. 7.3, we consider the oscillations of density of parity crossings due to supershell effects and demonstrate that such oscillations are associated with the classical periodic orbits of the billiard. In Sec. 7.4, we show that the statistics of the fermion parity crossing spacings in Majorana billiards is universal and the universality class depends on whether the corresponding normal state system is regular, diffusive, chaotic or localized. Finally, in Sec. 7.5, we show that Majorana wavefunctions in chaotic Majorana billiards display quantum scarring; an enhancement of the eigenfunctions along unstable classical periodic orbits of a classically chaotic system.

7.1 Majorana Billiards from *s*- and *p*-wave Topological Superconductors

Majorana billiards can either be finite-sized superconductors or a finite-sized semiconductors with proximity induced superconductivity (also known as Andreev billiards [154–156]). The former is described by the *p*-wave topological superconductor Hamiltonian given in Eq. (6.1), while the latter is described by the *s*-wave topological superconductor Hamiltonian given in Eq. (6.2). We focus on Majorana billiards which can be clean or disordered, with regular or irregular geometrical shapes. As a result, the dynamics of the

system can be ballistic chaotic/integrable or diffusive in the classical limit. In Fig. 7.1, we show the geometrical shapes that we use in numerical tight-binding simulations.

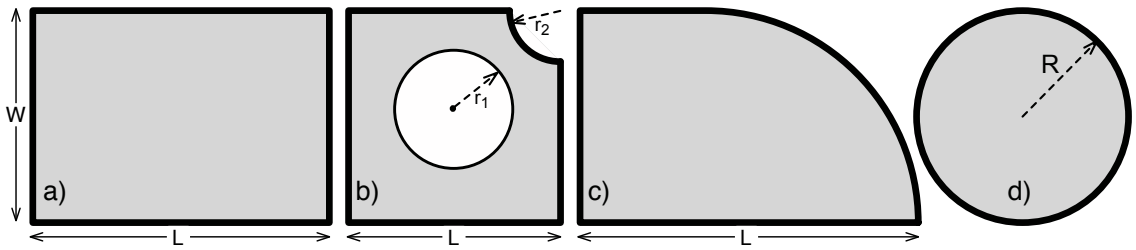

Figure 7.1: The geometrical shapes we use in the tight-binding numerical simulations: (a) rectangle, (b) Lorentz gas cavity, (c) quarter-stadium cavity, (d) disk.

7.1.1 Fermion Parity Crossings in Majorana Billiards

Fermion parity switch in a superconducting system is defined by the crossing of the energy levels with different fermion parities at the Fermi energy. In our problem, this corresponds to looking for the zero energy solutions of s-wave and p-wave Hamiltonians (Eqs. 6.2 and 6.1) as an external parameter is changed. The external parameters for H_s are the chemical potential μ that can be changed via gate voltage or the Zeeman energy B that can be changed via magnetic field. On the other hand, the only external parameter for H_p is the chemical potential μ. We label the parameters at which H_s or H_p have zero energy solutions as the fermion parity crossing points.

7.1.2 Density of Fermion Parity Crossings

We introduce the density of fermion parity crossing points of a Majorana billiard as a function of a dimensionless parameter β ($\beta = \mu/t$ or $\beta = B/t$)

$$\rho(\beta) \equiv \sum_i \delta(\beta - \beta_i), \tag{7.1}$$

where $\beta_i = \mu_i/t$ or $\beta_i = B_i/t$, μ_i and B_i are the fermion parity crossing points and t is the relevant energy scale of the problem (in tight-binding simulations, $t = \hbar^2/2ma^2$ is the hopping integral and a is the lattice constant). We find that the integrated density of fermion parity crossings is more accessible numerically, hence we define $\mathcal{N}(\beta)$ as

$$\mathcal{N}(\beta) = \int_{-\infty}^{\beta} \rho(\beta')\, d\beta'. \tag{7.2}$$

As is generally done in semiclassical approach to the density of states of a quantum billiard [157–161], we separate the density $\rho(\beta)$ into two parts; the average value $\bar{\rho}(\beta)$ and the oscillations around this average $\rho_{\text{osc}}(\beta)$:

$$\rho(\beta) = \bar{\rho}(\beta) + \rho_{\text{osc}}(\beta). \tag{7.3}$$

We study $\bar{\rho}(\beta)$ in Sec. 7.2 and $\rho_{\text{osc}}(\beta)$ in Sec. 7.3.

7.2 Mapping to the Weyl Problem

In this section, we demonstrate that the problem of finding fermion parity crossing points of a topological superconductor can be mapped to an eigenvalue problem of a normal state Hamiltonian. We then use the Weyl expansion, which relates the smooth part of the density of states to the geometrical shape of the system [157, 158, 162], and use all the tools of semiclassical physics in order to obtain information about the fermion parity crossings in topological superconductors [159–161, 163, 164].

7.2.1 Average Density of Fermion Parity Crossings of a *p*-wave Majorana Billiard

We first investigate a *p*-wave Majorana billiard described by the Hamiltonian H_p [Eq. (6.1)]. The only external parameter to be varied for a *p*-wave system is the chemical potential. We solve for the zero-energy eigenstates of *p*-wave Hamiltonian, in order to obtain the fermion parity crossing points μ_i :

$$H_p|_{\mu=\mu_i}\,\chi = 0. \tag{7.4}$$

We premultiply Eq. (7.4) by τ_z and map the problem of finding μ_i to a non-Hermitian eigenvalue problem:

$$\left(\frac{\left(\mathbf{p} + im\Delta'\boldsymbol{\eta}\right)^2}{2m} + V(\mathbf{r}) + m\Delta'^2\right)\chi = \mu\,\chi, \tag{7.5}$$

where we define $\boldsymbol{\eta} = \tau_y\hat{x} - \tau_x\hat{y}$. This non-Hermitian operator can be identified as the Hamiltonian of a Rashba 2DEG with an imaginary Rashba parameter $\alpha = i\Delta'$. We see that the real right eigenvalues of the non-Hermitian operator given in Eq. 7.5 coincide with the fermion parity crossing points μ_i. On the other hand, the complex eigenvalues

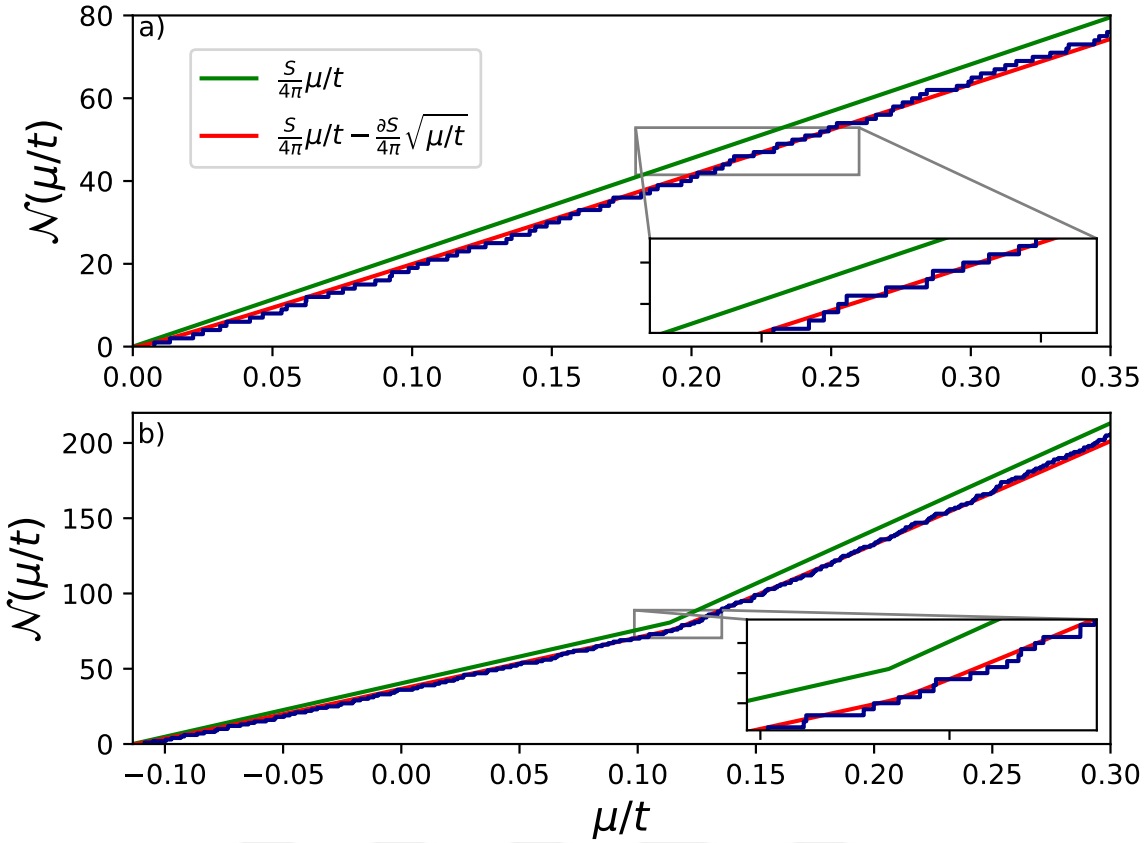

Figure 7.2: $\mathcal{N}(\mu/t)$ for a ballistic quarter stadium MB [see Fig. 7.1c]. The solid lines are obtained using Eq. (7.8) for the top panel and Eq. (7.17) for the bottom panel, as a function of μ/t. The green line refers to the first term in the Weyl expansion whereas the red line includes the surface corrections. The staircase plot (blue line) is the result of tight-binding simulations. Lower-right insets are zoom-ins to show the fit between tight-binding simulation and theory. (a) p-wave Majorana billiard with with $L = 80a$, $W = 40a$ and $\Delta' = 0.001ta$. (b) s-wave MB with $L = 100a$, $W = 50a$, $B = 0.23t$, $\Delta = 0.2t$ and $\alpha = 0.001ta$. The kink in the plot is at $\mu = \epsilon$ and signals the entrance of the second spin band, previously spin-polarized, into the picture.

are associated with avoided level crossings.

Essentially, solving Eq. 7.5 is sufficient for obtaining fermion parity crossing points. We find that further simplification of the problem is possible in the experimentally relevant limit $S \ll \xi \partial S$. Here, S is the system area, ∂S is the size of the boundary and ξ is the superconducting coherence length. This limit would correspond to $W \ll \xi$ for a rectangular system. We find that, in this limit, the non-Hermitian eigenvalue problem can be transformed by a local rescaling transformation to a Hermitian eigenvalue problem. We rescale the eigenfunction $\chi = \mathrm{e}^{\boldsymbol{\eta}\cdot\mathbf{r}/\xi - r^2/\xi^2}\tilde{\chi}$ and then expand in powers of $S/(\xi\,\partial S)$, we obtain [165]

$$\left(\frac{\left(\mathbf{p} + \frac{2m^2\Delta'^2}{\hbar}(\hat{\mathbf{z}} \times \mathbf{r})\,\tau_z\right)^2}{2m} + V(\mathbf{r}) + m\Delta'^2 \right) \tilde{\chi} = \mu\,\tilde{\chi}. \tag{7.6}$$

We arrive at the result that the fermion parity crossing points are eigenvalues of a normal state Hamiltonian with a fictitious magnetic field $\pm 2m^2(\Delta')^2/e\hbar$ and a constant potential shift $m(\Delta')^2$. As the energy levels are even functions of the Zeeman energy, we find that the fictitious magnetic field only modify the energy splitting for nondegenerate energy levels and hence its effects on the spectrum can be ignored. Consequently, we see that all eigenvalues of Eq. (7.6) are real and we conclude that all fermion parity crossing points (fermion parity crossing spectrum) are simply eigenvalues of a *normal state* Hamiltonian:

$$\left(\frac{p^2}{2m} + V(\mathbf{r}) + m\Delta'^2\right)\tilde{\chi} = \mu\tilde{\chi}. \tag{7.7}$$

Therefore, we establish that we can apply all the relevant tools from semiclassical physics to the spectrum of fermion parity crossings using Eq. (7.7). These tools include the Weyl expansion for average density of states [157, 162, 166] (or, for the case of soft confinement, the Thomas-Fermi approximation [158]); Gutzwiller's trace formula in billiards for oscillations (supershell effects) in density of states [155, 161, 167–169]; the theory of Lifshitz tails [170–172] for disordered systems; as well as the random matrix theory results for density of states fluctuations [104, 173].

We use the mapping and obtain the average density of fermion parity crossings for the p-wave system $\bar{\rho}_{\mathrm{w},p}(\mu)$ in d dimensions:

$$\bar{\rho}_{\mathrm{w},p}(\mu) = \begin{cases} \frac{L}{2\pi\sqrt{\mu}} + \mathcal{O}(1) & \text{if } d = 1 \\ \frac{S}{4\pi} - \frac{\partial S}{8\pi\sqrt{\mu}} & \text{if } d = 2 \\ \frac{V\sqrt{\mu}}{4\pi^2} - \frac{\partial V}{16\pi} & \text{if } d = 3, \end{cases} \tag{7.8}$$

where L is the length of the 1D wire, S and ∂S are the area and perimeter of the 2D billiard, and V and ∂V the volume and surface area of the 3D dot cavity respectively. We note that the $d = 3$ case is a trivial extension of the $d = 2$ case in which we consider a 2D p-wave pairing. We present both analytical and numerical (tight-binding simulations) results for the integrated density of fermion parity crossings $\mathcal{N}(\mu/t)$ for a 2D p-wave Majorana billiard in Figs. 7.2(a). We see that the analytical and numerical results fit remarkably well without any fitting parameters, once the boundary corrections in the Weyl expansion are taken into account.

7.2.2 Average Density of Fermion Parity Crossings of a *s*-wave Majorana Billiard

We now consider the s-wave Majorana billiard described by H_s [Eq. (6.2)]. In contrast to p-wave case, there are two external parameters in s-wave Majorana billiards, namely the chemical potential and the Zeeman energy. Similarly, we start with the zero-energy eigenvalue problem

$$H_s|_{\mu_i,B_j}\,\psi = 0 \tag{7.9}$$

where μ_i and B_j are the fermion parity crossing points.

Here, we have two equivalent choices of obtaining a non-Hermitian eigenvalue problem: eigenvalues corresponding to B or to μ. This equivalence leads to a scaling relation between μ_i and B_j which we discuss in Sec. 7.2.3. Without loss of generality we focus on the eigenvalue problem for μ_i below. We premultiply Eq. (7.9) with τ_z and obtain

$$\left(\frac{\mathbf{p}^2}{2m} + V(\mathbf{r}) + \alpha\boldsymbol{\eta}\cdot\mathbf{p} + B\sigma_x\tau_z + i\Delta\tau_y\right)\psi = \mu\,\psi, \tag{7.10}$$

where $\boldsymbol{\eta} = (\sigma_y\hat{x} - \sigma_x\hat{y})$. This equation can then be solved using tight binding methods and obtain the fermion parity crossing points μ_i, see Appendix I.

In order to compare with the numerical results obtained from Eq. (7.10), we also proceed analytically. We ignore the chiral symmetry breaking term $i\alpha p_y\sigma_y$ in Eq. (6.2), which is justified in the experimentally relevant limit $S \ll \xi\partial S$. In this case, the operator $\sigma_y\tau_y$ anticommutes with *S*-wave Hamiltonian. We follow Ref. [[165]] and [[174]] to bring the Hamiltonian to an off-diagonal form using the operator:

$$U = (1 + i\sigma_x)\,(1 + i\tau_x)\,[(1 + \sigma_z) + (1 - \sigma_z)\,\tau_x]\,/4, \tag{7.11}$$

and we obtain:

$$H = h(\mathbf{p},\mathbf{r})\,\sigma_z\tau_y - \alpha p_x\tau_y + B\sigma_x\tau_x + \Delta\tau_x. \tag{7.12}$$

The zero-energy solutions of the Hamiltonian given in Eq. (7.12) are of the form $\chi_+ = (\phi_+, 0)^T$ and $\chi_- = (0, \phi_-)^T$. $\phi_\pm$ satisfy the following non-Hermitian eigenvalue problem:

$$(h(\mathbf{p},\mathbf{r})\sigma_z - i\alpha p_x\sigma_x \mp B \mp \Delta\sigma_x)\;\phi_\pm = 0. \tag{7.13}$$

As we consider a finite system, we find the solution that satisfies all boundary conditions

$$\phi_{n,\pm}(\epsilon) = \zeta_{\pm}(\epsilon) \mathrm{e}^{\pm x/\xi} \psi_n(\epsilon), \tag{7.14}$$

where $\zeta_{\pm}(\epsilon)$ are the eigenvectors of the 2×2 matrix $\epsilon\,\sigma_z \mp \Delta\sigma_x$ with eigenvalue $\pm\sqrt{\epsilon^2+\Delta^2}$ and ψ_n satisfies the eigenvalue equation:

$$h\,\psi_n = E_n\,\psi_n. \tag{7.15}$$

We substitute Eq. (7.14) into Eq. (7.13) and notice that the zero-energy solutions occur on family of curves in the $B-\mu$ plane. We find that the curves obey the following equation:

$$B^2 = (\mu - E_n)^2 + \Delta^2, \tag{7.16}$$

for a given eigenvalue E_n of the spinless single particle Hamiltonian $h(\mathbf{p},\mathbf{r})$. Therefore, we demonstrate that the eigenvalue spectrum of the normal state Hamiltonian $h(\mathbf{p},\mathbf{r})$ yields the density of fermion parity crossing spectrum with respect to either chemical potential or Zeeman energy.

We note that the single particle Hamiltonian $h(\mathbf{p},\mathbf{r})$ is the same for *s*- and *p*-wave cases. Therefore, it is possible to write the *s*-wave Weyl expansion for $\rho_{\mathrm{w},s}(\mu)$ and $\rho_{\mathrm{w},s}(B)$ in terms of their *p*-wave counterpart $\rho_{\mathrm{w},p}(\mu)$ in Eq. (7.8):

$$\rho_{\mathrm{w},s}(\mu,B) = \sum_{\varsigma=\pm1} \rho_{\mathrm{w},p}(\mu+\varsigma\epsilon)\,\theta(\mu+\varsigma\epsilon), \tag{7.17}$$

where $\theta(x)$ is the Heaviside step function, $\epsilon = \sqrt{B^2-\Delta^2}$ as before and the $\varsigma = \pm1$ terms in the sum represent the different spin states, separated in energy by the magnetic field.

7.2.3 Universal Scaling Properties of Fermion Parity Crossing Points in *s*-wave Systems

Eq. (7.16) indicates that the fermion parity crossing spectra feature a scaling relation for a given disorder realization and/or geometric shape. For a given system, fermion parity crossing spectra for different set of values of μ, B, or Δ show no correlation. However, expressed in terms of the combination $\mu \pm \sqrt{B^2-\Delta^2}$, all fermion parity crossing points collapse on the same set of points (Fig. 7.3). In addition, if the fermion parity crossing spectrum of a single Zeeman-split spin band is known, the other can immediately be obtained by shifting the spectrum by $2\sqrt{B^2-\Delta^2}$.

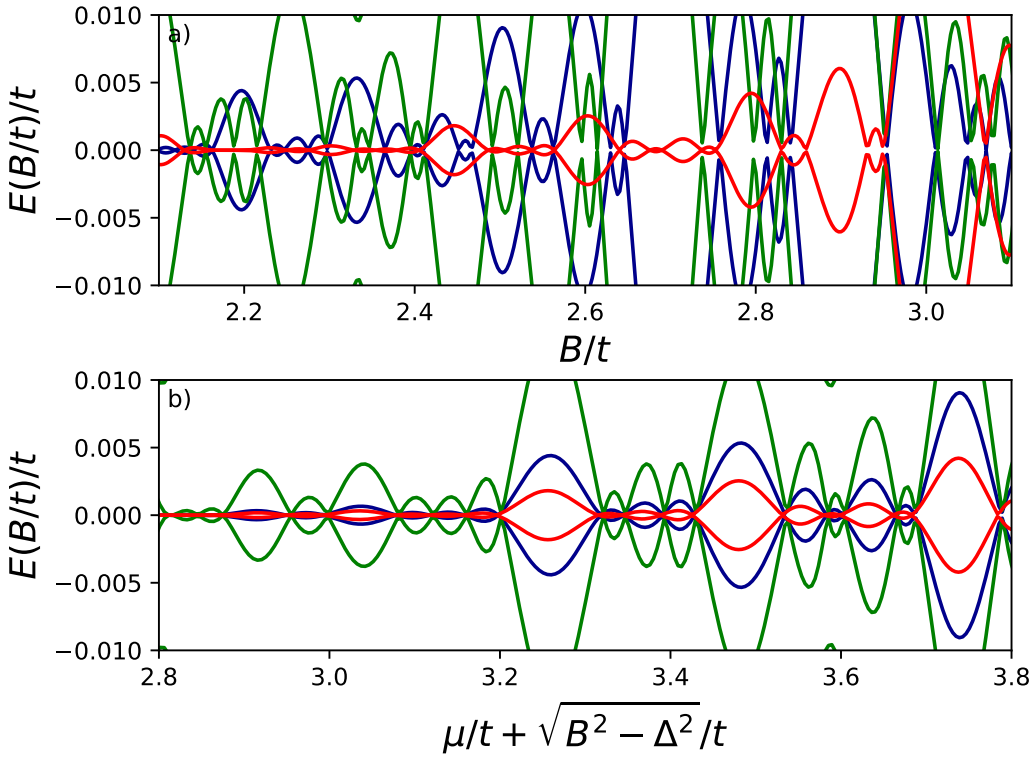

Figure 7.3: A plot of the lowest four eigenvalues of the disordered s-wave Hamiltonian in Eq. (6.2), discretized on a 1D lattice of 100 sites, plotted as a function of (a) B/t and (b) $\mu/t + \sqrt{B^2 - \Delta^2}/t$, for different values of Hamiltonian parameters. In both plots, the green set of curves represents the lowest four eigenvalues obtained for $\Delta = 1.5t$, $\alpha = 0.05ta$, $\mu = 1.8t$; the blue set is for $\Delta = 1.8t$, $\alpha = 0.05ta$, $\mu = 2.0t$; and the red set is for $\Delta = 1.8t$, $\alpha = 0.08ta$, $\mu = 1.6t$. In all cases, the same disorder realization with a disorder strength $V_d = 0.5t$ is utilized.

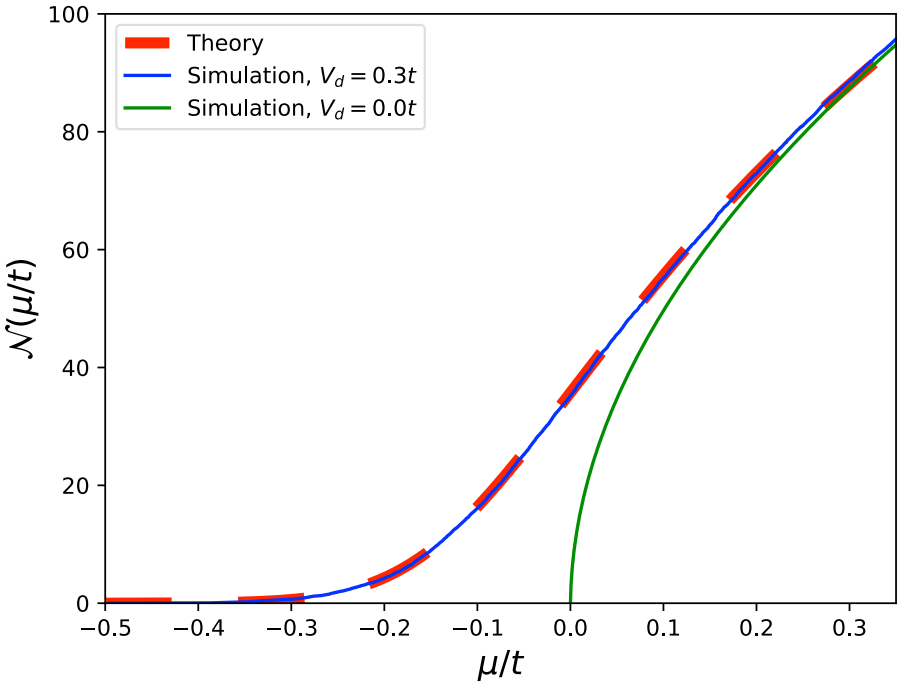

Figure 7.4: $\mathcal{N}(\mu/t)$ vs. μ/t for a p-wave 1D MB for a wire of length $500a$ and $\Delta' = 0.001ta$. For the disordered case, the tight-binding simulation plot is the average of 200 disorder realizations. The theory lines are the plots of Eq. (7.18) for $V_d = 0$ and $V_d = 0.3t$.

We demonstrate this universality by plotting first four eigenvalues of a 1D s-wave system with a specific disorder realization for different values of μ and Δ as a function of B in Fig. 7.3(a) and as a function of $\mu + \sqrt{B^2 - \Delta^2}$ in Fig. 7.3(b). We obtain these plots discretizing the s-wave Hamiltonian in Eq. (6.2) in 1D over 100 sites and numerically solving the resulting eigenvalue problem. It is evident in Fig. 7.3(b) that, all level crossings occur at the same set of values of $\mu + \sqrt{B^2 - \Delta^2}$ for systems with the same disorder realization but different system parameters.

7.2.4 Lifshitz Tail in Disordered Majorana Billiards

For noninteracting systems with random disorder potential, quasiparticles get localized due to the presence of islands with an average of below zero potential, even though the overall average potential for the whole system is zero. This results in a nonzero density of states below the bottom of the band, known as the Lifshitz tail [170–172]. We find that the phenomenon of Lifshitz tail is also present in average density of fermion parity crossings in Majorana billiards (see Fig. 7.4). We numerically obtain the disorder-averaged integrated density of fermion parity crossings for a 1D p-wave MB with Gaussian disorder [i.e., $\langle V(\mathbf{r})V(\mathbf{r}')\rangle = D\,\delta(\mathbf{r}-\mathbf{r}')$] and compare with the analytical formula for the Lifshitz

tail [172]:

$$\mathcal{N}(\mu) = \frac{\kappa_0}{\pi^2\,\varepsilon_0}\,\frac{1}{[\mathrm{Ai}(-2\mu/\varepsilon_0)]^2 + [\mathrm{Bi}(-2\mu/\varepsilon_0)]^2}, \tag{7.18}$$

where Ai and Bi are the Airy functions, $\varepsilon_0 = (D^2\, m\hbar^{-2})^{1/3}$ and $\kappa_0 = (D\, m^2\hbar^{-4})^{1/3}$.

In Fig. 7.4, we plot the analytical formula Eq. (7.18) and numerical results obtained from a tight-binding simulations for a 1D disordered p-wave wire (and a tight-binding simulation for the same wire with zero disorder for comparison). We notice that there is a nonzero density of parity crossings at negative μ values, which is not present for a clean wire. We emphasize that this is caused by rare disorder configurations that allows trapping of quasiparticles. We note that the theory and the numerical simulations show remarkable agreement without any fitting parameters.

7.3 Oscillatory Part of Density of Fermion Parity Crossings

In this section, we examine the oscillatory part ρ_{osc} of the density of fermion parity crossings [see Eq. (7.3)]. Density of states oscillations of finite quantum systems such as nuclei, atomic clusters and nanoparticles are the known as the shell and supershell effects. These oscillations are associated with the classical periodic orbits of a given quantum system and described by Guztwiller or Balian-Bloch trace formula [155, 157, 161, 167–169].

We apply the analysis of the oscillatory part of density of states in Refs. [[157]] and [[158]] to the case of the fermion parity crossing spectrum of a clean p-wave MB. We obtain the fermion parity crossing points by the method described in Sec. 7.2.1 of the p-wave Hamiltonian. In this way, we extend the Gutzwiller and/or Balian-Bloch trace formula [157, 161] into the fermion parity crossings of finitely sized topological superconductors. Similar to the original case, the new trace formula also expresses the oscillating part ρ_{osc} as a sum over classical periodic orbits ζ that contributes a term oscillating with its classical action:

$$\rho_{\mathrm{osc}}(\mu) = \sum_{\zeta} \mathcal{A}_\zeta \cos\Phi_\zeta(\mu), \tag{7.19}$$

where $\mathcal{A}_\zeta$ is related to the stability of the orbit ζ and $\hbar\Phi_\zeta$ is associated with the classical action as well as the Maslov indices. The precise form of these terms depends on whether the periodic orbits in question are isolated or degenerate. In the case of isolated periodic

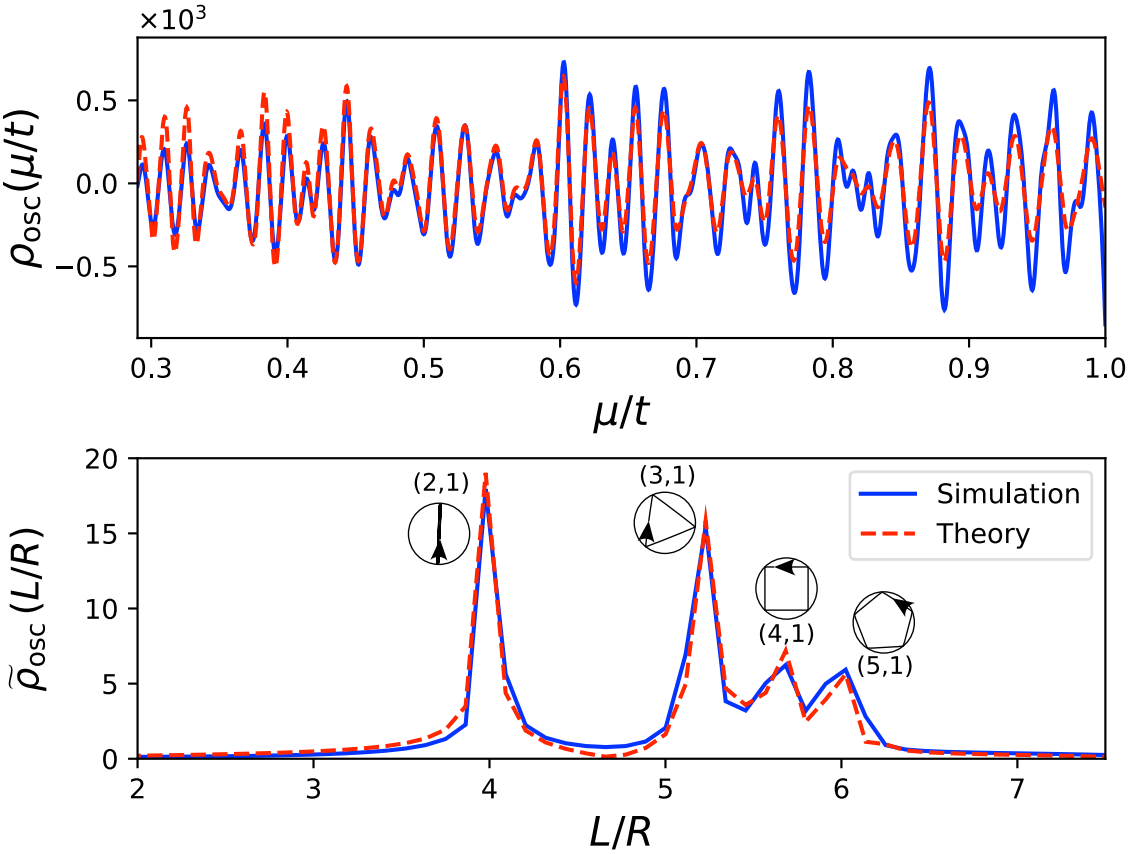

Figure 7.5: (a) Density oscillations of fermion parity crossings ρ_{osc} for a clean p-wave disk Majorana billiard with $R = 100a$, $\Delta' = 0.001ta$. (b) The Fourier transform of ρ_{osc}. The (v, w) pairs and corresponding classical orbits for the peaks are labeled. The smoothing parameter for both figures is $\gamma = 0.4/R$.

orbits, we have:

$$\mathcal{A}_\zeta = \frac{T_\zeta/\pi\hbar}{\sqrt{|\det(M_\zeta - I)|}}, \quad \Phi_\zeta(\mu) = \frac{S_\zeta(\mu)}{\hbar} - \frac{\sigma_\gamma \pi}{2}, \tag{7.20}$$

The term T_ζ corresponds to the period of the parent periodic orbit for which there is no retracing. M_ζ is the so-called the monodromy matrix of the orbit [158], and finally σ_γ is known as the Maslov index. The classical action for a periodic orbit ζ is defined as $S_\zeta(\mu) = \oint_\zeta \mathbf{p} \cdot d\mathbf{r}$ and the significant contribution is due to single degenerate orbits. We consider two-dimensional systems and the corresponding singly degenerate orbits

$$\begin{aligned} \mathcal{A}_\zeta &= \frac{2m}{(2\pi\hbar)^{3/2} p_F} \int \left| \frac{\partial r_\perp}{\partial p'_\perp} \right|_\zeta^{-1/2} dr_\parallel \, dr_\perp \,, \\ \Phi_\zeta(\mu) &= \frac{S_\zeta(\mu)}{\hbar} - \frac{\sigma_\gamma \pi}{2} - \frac{\pi}{4}, \end{aligned} \tag{7.21}$$

where p_F is the Fermi momentum. Eq. (7.21) describes the case in which an initial transverse perturbation of momentum $p'_\perp$ results in a deviation $r_\perp$ after a full period. It is evident that for a ballistic chaotic system, we have $|\mathbf{p}| = p_F$, therefore the classical action of the classical periodic orbit is evaluated at the Fermi momentum, i.e. $S_\zeta(\mu) = p_F L_\zeta$ where L_ζ is the length of the orbit ζ.

We now illustrate a case of a clean textitp-wave disk MB of radius R (see Fig. 7.1) and display our results. We obtain a closed-form analytical solution to this problem, using Eq. (7.19). In addition to the analytical formula, we perform numerical simulations and compare them. The periodic orbits of a disk billiard is specified by two integer numbers, namely the winding number w which is the number of times the orbit winds around the billiard and the vertex number v which is the number of times it reflects from the boundary. It is a straightforward task to find the length of the orbit as $L_{vw} = 2vR\sin(\pi w/v)$. Finally, we obtain

$$\begin{aligned}\rho_{\text{osc}}(\mu) = \frac{2mR^2}{\hbar^2}\left(\frac{\hbar}{\pi R\, p(\mu)}\right)^{1/2} \\ \times \sum_{w=1}^{\infty}\sum_{v=2w}^{\infty} f_{vw}\frac{\sin^{3/2}(\pi w/v)}{\sqrt{v}} \\ \times \text{Im}\left[\exp\left\{i\frac{p_F L_{vw}}{\hbar} + i\phi_{\text{po}}\right\}\right],\end{aligned} \tag{7.22}$$

where $\phi_{\text{po}} = -3v\pi/2 + 3\pi/4$, $f_{vw} = 2\,\theta(v-2w)$ with $\theta(x)$ being the unit step function. We plot the oscillatory part of the density of fermion parity crossings $\rho_{\text{osc}}(\mu/t)$, separately for the numerical simulations (blue, solid line), where we numerically solve Eq. (A6) of Ref. [175] for E = 0 and thus obtain the set of μ values that allow a zero mode solution, and analytical solutions given by Eq. (7.22) (red, dashed line) for a *p*-wave disk Majorana billiard in Fig. 7.5(a) and the agreement between numerics and analytics is remarkable. We note that our choice of smoothing function is a Gaussian function. Furthermore, the Fourier transform of the oscillatory part of the density of fermion parity crossings, which we denote as $\tilde{\rho}_{\text{osc}}(L/R)$ is plotted in Fig. 7.5(b). We use a dimensionless parameter L/R, i.e., orbit length divided by disk radius, for convenience.

We identify the peaks in Fig. 7.5(b) as the contributions of the periodic orbits and with corresponding relative amplitudes. We note that, the locations of the peaks at specific L/R values represent the corresponding high-degeneracy orbits (as shown in the insets) and the relative amplitudes indicate the order of degeneracy of the orbit, as expected. In Appendix J, we consider the tight-binding version of the two-dimensional disk Majorana billiard and obtain the oscillatory part of the density of fermion parity crossings ρ_{osc}.

7.4 Universal Fluctuations of Fermion Parity Crossings

In this section, we study the correlation between the consecutive fermion parity crossings. In the limit $S/\partial S \ll \xi$ (for a rectangular billiard, this limit would correspond to having the width being smaller than the superconducting coherence length), we obtain the distribution of the fermion parity crossing spacings. We show that the fermion parity crossings points show no correlation and their spacing distribution is Poissonian, if the corresponding normal state is localized:

$$P(\delta\mu) = \exp\big(-\delta\mu/\langle\delta\mu\rangle\big), \tag{7.23}$$

where $\delta\mu$ is the fermion parity crossing spacing and $\langle\delta\mu\rangle$ is the corresponding mean value, which we obtain by taking an ensemble of different disorder configurations. The fermion parity crossing points start to show correlation in the form of antibunching for small spacings, as the normal state system is near a delocalization transition. However, in this case, the large spacings are still uncorrelated. This behavior is well-known from the Anderson metal-insulator transition, and it is manifested by the semi-Poissonian distribution [176]:

$$P(\delta\mu) = \frac{\delta\mu}{\langle\delta\mu\rangle}\exp\big(-2\delta\mu/\langle\delta\mu\rangle\big). \tag{7.24}$$

As the normal system becomes further delocalized in such a way that the escape time associated with the Thouless energy is shorter than $\hbar/\langle\delta\mu\rangle$, the distribution of fermion parity crossing point spacings is given by the Wigner-Dyson distribution for the orthogonal matrices and spacings themselves are represented by the eigenvalues of an ensemble of real Hermitian random matrices [163, 173, 177–180]:

$$P(\delta\mu) = \frac{\pi\delta\mu}{2\langle\delta\mu\rangle}\exp\left(-\frac{\pi\delta\mu^2}{4\langle\delta\mu\rangle^2}\right). \tag{7.25}$$

We perform numerical simulations for tight-binding Majorana billiards in order to demonstrate the fermion parity crossing spacings and plot them against the distribution functions given in Eqs. (7.23), (7.24), and (7.25). We note that we do not use the chiral approximation while performing the numerical simulations. Instead, we use the tight-binding version of the full 2-D version of the Bogoliubov–de Gennes Hamiltonian (see Appendix I).

We first consider rectangular shaped p-wave Majorana billiards with disorder in Fig. 7.6 (a)-(c). We increase the length of the billiard but keep the width and the coherence length as constants. As a result, the escape time of the system also increases. Correspondingly, the distributions of the fermion parity crossing spacings evolve from Wigner-Dyson (a)

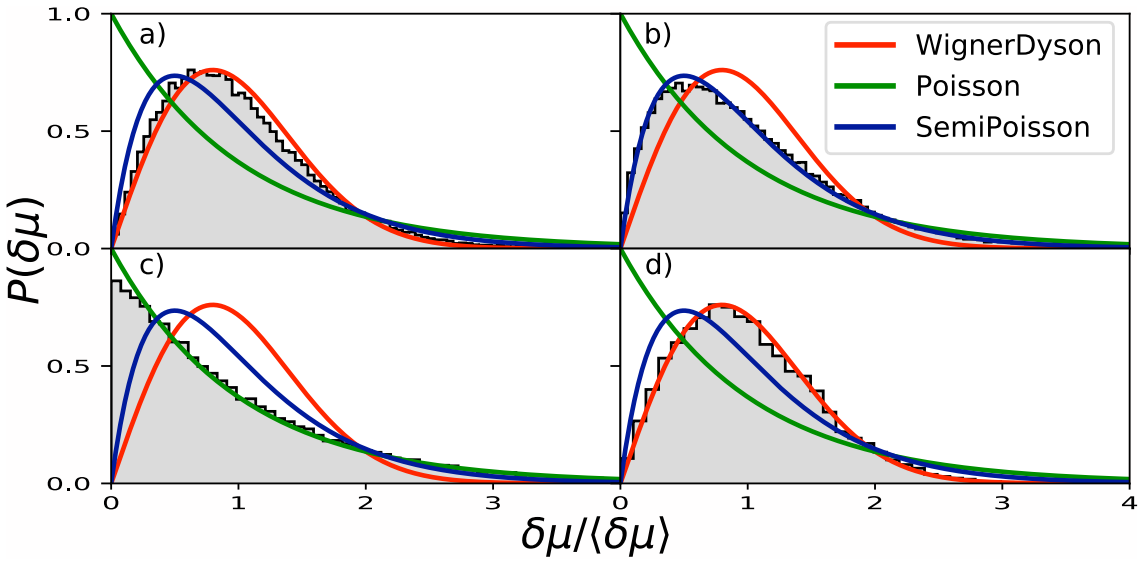

Figure 7.6: (a)-(c) Level spacing distributions for a disordered rectangular p-wave MBs of varying lengths, averaged over 500 disorder realizations, with $\Delta' = 0.025ta$, disorder strength $V_d = 0.5t$, width $W = 20a$. (a) $L = 40a < \xi$, (b) $L = 100a \gtrsim \xi$ and (c) $L = 1600a \gg \xi$, with $\xi = 80a$ being the superconducting coherence length. (d) Level spacing distributions, averaged over 225 cavity realizations, for a clean p-wave Lorentz cavity MB. Here, $\Delta' = 0.001ta$, $L = 50a$, $W = 50a$, and $r_1 = r_2 = 10a$. The values of L/ξ in panels (a)-(d) are 0.5, 1.25, 20 and 0.4, respectively.

to semi-Poissonian(b) and finally to Poissonian (c). This is a result of the normal state system becoming more localized as the length of the cavity grows. Finally, in Fig. 7.6(d), we consider a chaotic billiard without any disorder. As expected, the distribution of the fermion parity crossing spacings is given by the Wigner-Dyson distribution.

Next we consider the statistics of fermion parity crossing spacings of s-wave Majorana billiards. Unlike the p-wave case, this time we decrease the coherence length by changing the Zeeman energy, while keeping the size parameters of the cavity constant in Fig. 7.7 (a)-(c). This approach is essentially the same as increasing the length from the point of view of localization in the normal state. As the coherence length is decreased, the normal state system becomes more localized, resulting in the same evolution of the distribution of the fermion parity crossing spacings in the p-wave billiard case. However, s-wave billiards differ from their p-wave counterparts in the following way: if both spin states are occupied, each spin species form their own statistics and feature level repulsion [174] for larger Zeeman energy [see Eq. (7.17)]. As the Zeeman energy increases, the level statistics for both spin species become uncorrelated, therefore the overall consecutive fermion parity crossings also becomes uncorrelated. As a result, the level repulsion is not only suppressed but also the distribution of small spacings $P(\delta\mu \to 0)$ approaches 0.5 [see Fig. 7.7 (c)-(d)].

We recapitulate the universality class crossover in narrow, ($W \ll \xi$) 2D Majorana billiards in Fig. 7.8. We list all the values of L/ξ for the billiards illustrated in Figs. 7.6(a)-

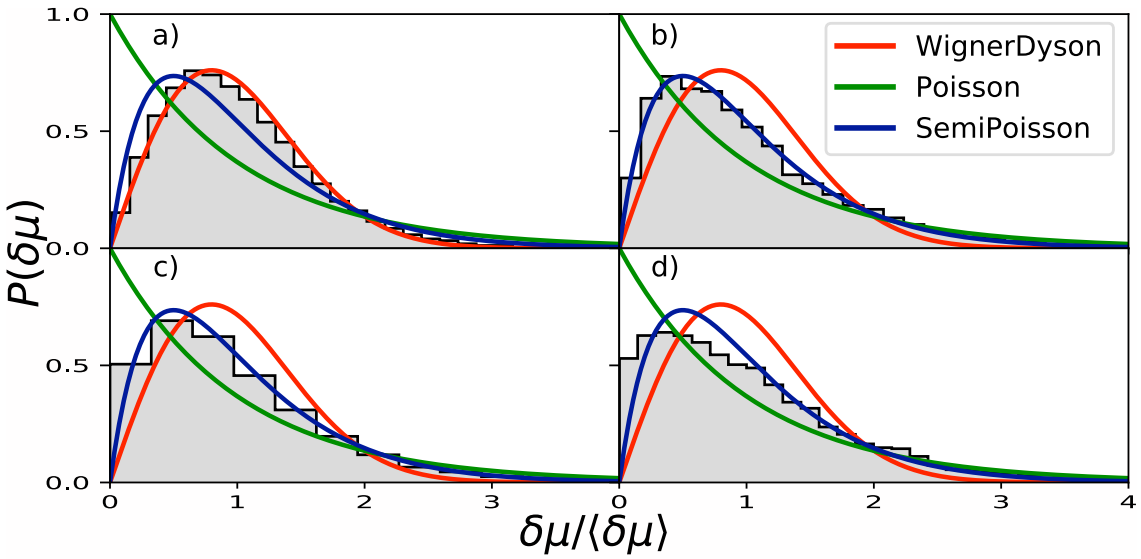

Figure 7.7: (a)-(c) Level spacing distributions for disordered rectangular s-wave MBs with increasing Zeeman energy B, averaged over 500 disorder realizations, with $L = 200a$, $W = 10a$, $V_d = 0.2t$, $\alpha = 0.025ta$, $\Delta = 0.12t$, and (a) $B = 1.12t$, (b) $B = 0.22t$ and (c) $B = 0.13t$. (d) Level spacing distributions for clean s-wave Lorentz cavity MB, averaged over 225 cavity realizations. Here, $\alpha = 0.001ta$, $\Delta = 0.2t$, $B = 0.23t$, $L = 50a$, $W = 50a$, and $r_1 = r_2 = 10a$. The values of L/ξ in panels (a)-(d) are 0.27, 1.63, 6.1 and 0.04, respectively.

(d) and 7.7(a)-(d). As the ratio of the length L and coherence length ξ is varied from being small ($L/\xi \ll 1$) to large ($L/\xi \gg 1$), the distribution of the fermion parity crossing spacings vary from the Wigner-Dyson to semi-Poissonian to Poissonian, hence showing the universality class crossover in Majorana billiards.

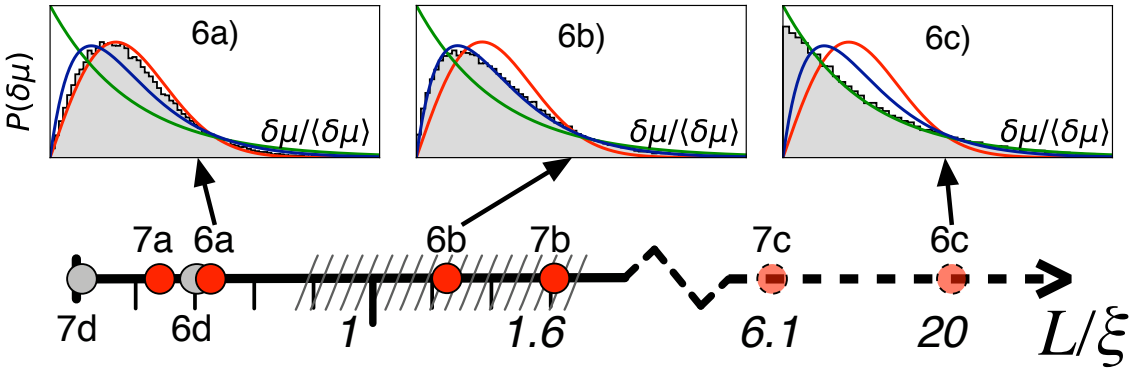

Figure 7.8: The L/ξ values for Figs. 7.6(a)-7.6(d) and 7.7a-7.7(d). The shaded region on the L/ξ axis around $L/\xi = 1$ illustrates the universality class crossover region where the statistics is semi-Poissonian. Three panes from Fig. 7.6 are reproduced as an example of Gaussian, semi-Poissonian and Poissonian statistics. Here, the length L for each shape is defined in Fig. 7.1.

Finally, we study the short coherence length limit, in which the overall system size exceeds ξ in all directions. This case was considered by Beenakker *et al.* [104], and it

was concluded that the fermion parity crossing points display statistics equivalent to real eigenvalues of a real *non-Hermitian* matrix. We also demonstrate that this is indeed the case by considering a Majorana billiard with both dimensions L_1 and L_2 much larger than ξ. We numerically obtain the fermion parity crossing spacings and display their statistics in Fig. 7.9, which verifies that the statistics is described by the semi-Poissonian distribution.

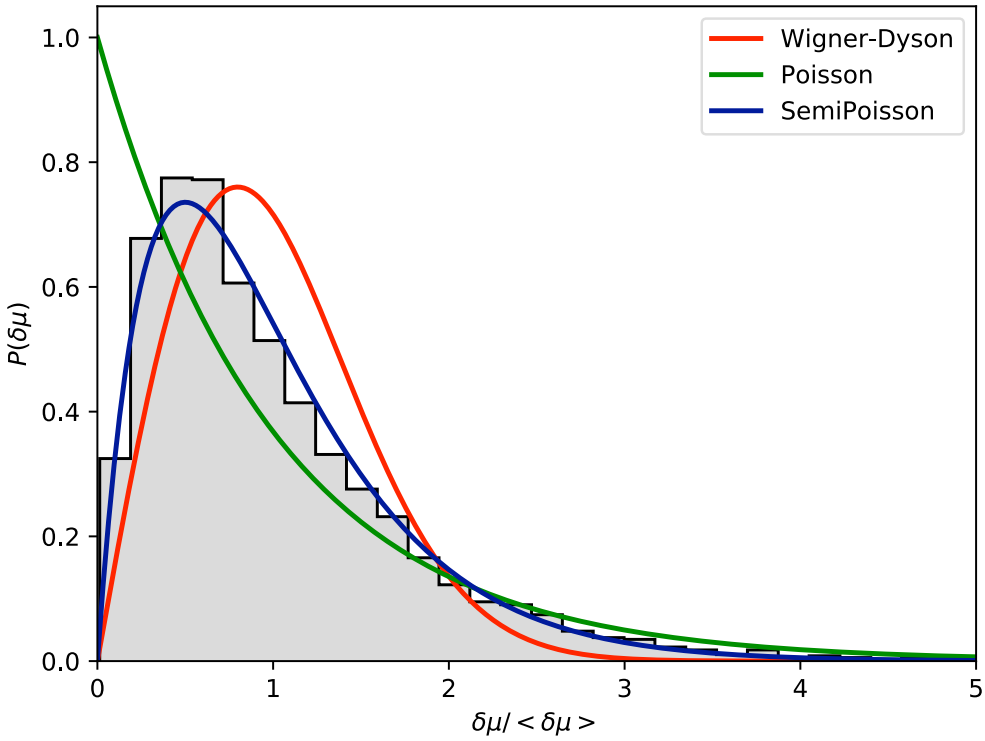

Figure 7.9: Fermion parity crossing spacing statistics for a p-wave system with *both* dimensions much larger than ξ ($L = W = 5\xi$), showing the statistics obtained from a tight-binding simulation of a disordered system in a square geometry (500 disorder realizations) whose parameters are $L = W = 80a$, $V_0 = 0.32t$, $\Delta' = 0.125ta$ and $\xi = 16a$.

7.5 Majorana Scars

In this section, we focus on the quantum scars in Majorana wavefunctions of chaotic Majorana billiards. First conceived by Heller [181], quantum scars are non-chaotic eigenstates that exist along the isolated unstable classical periodic orbits of classically chaotic system. Even though the unstable periodic orbits have zero measure in the phase space of a chaotic system, the ones with the shortest periods give rise to enhanced probability density.

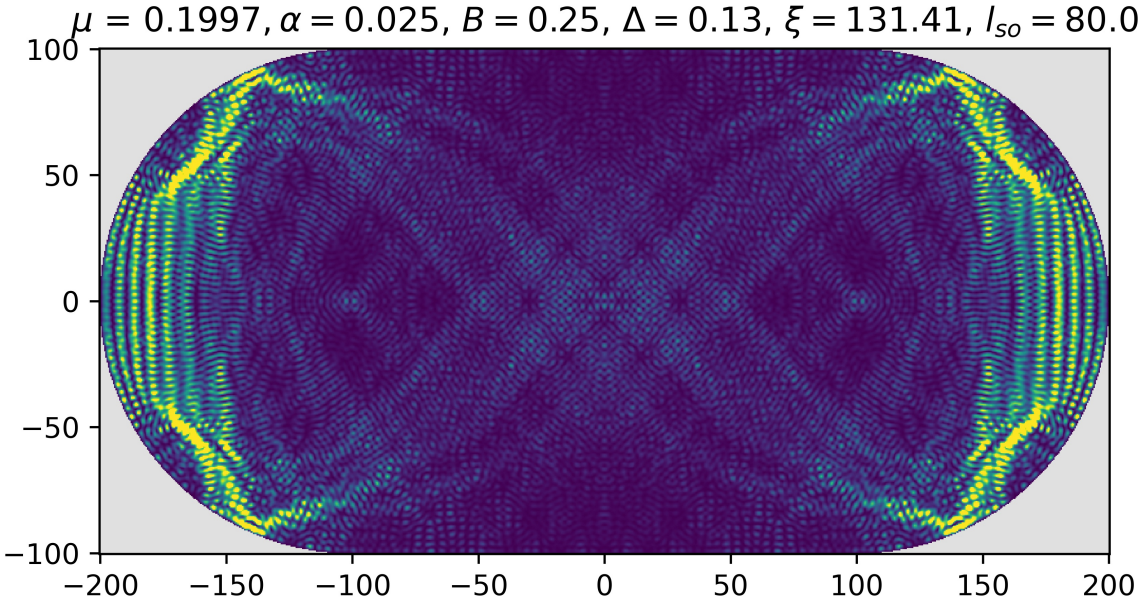

Figure 7.10: A stadium shaped Majorana billiard, displaying quantum scars with a localized behavior of a Majorana bound state.

This is a striking property of quantum chaos. Quantum scarring is a correction to the Berry's conjecture that the eigenstates of a classically chaotic systems are uniformly distributed over the phase space, up to corrections due to quantum fluctuations [182]. In this regard, quantum scars are an example of non-ergodic eigenfunctions of an otherwise chaotic system in the quantum regime.

In Sec. 7.2, we have shown that the eigenvalue spectrum of the normal state Hamiltonian $h(\mathbf{p}, \mathbf{r})$ yields the density of fermion parity crossing spectrum. Correspondingly, the eigenstates of the normal state Hamiltonian given in Eq. (7.14) can be used to construct the Majorana wavefunctions:

$$\phi_{\pm}(\mathbf{r}) = \sum_{n} \zeta_{\pm}(\epsilon) \mathrm{e}^{\pm x/\xi} \psi_n(\mathbf{r}, \epsilon) + \zeta_{\pm}(-\epsilon) \mathrm{e}^{\mp x/\xi} \psi_n(\mathbf{r}, -\epsilon). \tag{7.26}$$

It is evident from Eq. (7.26) that, the Majorana wavefunctions inherit the properties of the normal state wavefunctions ψ_n. Therefore, if a normal state eigenstate of a classically chaotic billiard is scarred and the eigenvalue of such an eigenstate satisfies Eq. (7.16) for given B, μ and Δ parameters, then the corresponding Majorana billiard retains scarring, reminiscent of the normal state quantum scar. We call such quantum scars with localized behavior as Majorana scars.

We demonstrate this by focusing on a stadium shaped billiard, which is among the most prominent systems that display quantum scarring. In Fig. 7.10, we show an example of a clearly visible quantum scar along the classical periodic orbit of the stadium shaped billiard. As anticipated, the quantum scar of the superconducting phase is tend to be more

localized on the edges of the system, set by the direction of the external magnetic field. However, we note that for the sake of demonstration of Majorana scars, these bound states are not well-localized as expected from a Majorana bound state.

7.6 Conclusions

In summary, we studied the spectra of fermion parity switches of a Majorana billiard using methods from semiclassical physics and quantum chaos. In particular, we show that the average density of fermion parity crossings is described by a Weyl expansion and the disordered billiards feature Lifshitz tails in the fully depleted limit. Moreover, we demonstrate that the parity crossings have a tendency to sequentially bunch and anti-bunch, which is reminiscent of supershell effects in finite systems. We show that the oscillations in the density of fermion parity crossings resulting from this bunching can be obtained by semiclassical means, extending Gutzwiller's trace formula for conventional quantum billiards to Majorana billiards. We show that the fermion parity crossing spacings obey a universal distribution as described by random matrix theory. Finally, we demonstrate that the eigenfunctions of a chaotic Majorana billiard show quantum scarring, reminiscent of the quantum scars in the normal state. We thus demonstrate that "one can hear (information about) the shape of a Majorana billiard" from fermion parity switches.

Chapter 8

CONCLUSION

In summary, we demonstrated that systems featuring spin-momentum locking can be utilized as platforms for Maxwell's demon implementations, provided that a "spin bath" is also present. We studied time-reversal invariant topological insulators as systems with spin-momentum locking, in particular quantum spin Hall insulators and three dimensional topological insulators as platforms. Our choice of topological insulators as opposed to topologically trivial systems with spin-momentum locking (such as Rashba 2DEG) is based on the fact that the topological properties prohibit backscattering of electrons from nonmagnetic impurities which may spoil the Maxwell's demon effect.

Previously, the spin bath in time-reversal invariant topological insulators was considered only as a source of backscattering that destroys topological protection. On the other hand, we demonstrated that the spin bath can be utilized as a memory resource of a Maxwell's demon setup. The spin bath consists mostly of nuclear spins that are readily available in most of the materials and magnetic impurity spins that can be deposited on demand. The choice of nuclear spins and/or magnetic impurities as the Maxwell's demon memory is the prominent feature of our proposals, making them convenient for engine applications that requires a scalable memory. Therefore, we solved the scalability problem of the Maxwell's demon implementations and offered an alternative way of storing and extracting energy.

In Chapter 3, we proposed and investigated our first Maxwell's demon engine proposal, which we call a quantum information engine. We established the charging and discharging cycle of the quantum information engine and derived the energy storage capacity and power output. An interesting aspect of the quantum information engine is that in the short edge limit, the stored energy that can be extracted in the form of electrical work scales quadratically with the size of the memory, (see Eq. (3.19)), indicating dense energy stor-

age capacity. In fact, we showed that the quantum information engine is experimentally feasible and has two distinct functionalities based on the material parameters: (i) as a spin-supercapacitor/engine or (ii) a spin-battery. Furthermore, we established that the quantum information engine exhibits an inductive response under an AC bias and demonstrated that the equivalent inductance scales inversely proportional to the number of nuclear spins. We stress that the quantum information engine is also useful for applications that require high inductance.

In Chapter 4, we presented a second Maxwell's demon engine proposal, which we call the capacitive quantum information engine, which takes advantage of specialized leads in order to improve the efficiency of the Maxwell's demon protocol. We established that the capacitive quantum information engine can operate at the Landauer's limit, provided that the memory erasure process is adiabatic. Equivalently, the energy stored in the information entropy of the memory can be extracted via the same specialized leads, completing the operating cycle of the capacitive quantum information engine. Moreover, we demonstrated that the capacitive quantum information engine is an ideal memristor, a two-terminal circuit component that regulates the charge current flow based on a memory component. This behavior of the capacitive quantum information engine provides another functionality that might prove useful for circuit applications as well.

Furthermore, we investigated 3D topological insulators as a platform for Maxwell's demon implementations in Chapter 5. As opposed to their 2D counterparts, 3D topological insulators exhibit diffusive transport behavior for systems longer than the elastic mean free path. The consequence of this difference is that the conversion of information entropy of the Maxwell's demon memory into electrical work is reduced. Therefore, we focused on ballistic and diffusive regimes and studied them separately. In the ballistic regime, we showed that the physics of Maxwell's demon based on the interaction between nuclear spins and spin-momentum locked electrons is still effective for 3D topological insulators, with a reduced effective interaction strength. In the diffusive regime, we found that the Maxwell's Demon effect still survives for devices longer than the mean free path. However, as opposed to the ballistic case, the magnitude of the induced current is reduced by a factor of ℓ_{el}/L.

Finally, in Chapter 7, we studied the spectra of fermion parity switches of a Majorana billiard using methods from semiclassical physics and quantum chaos. We demonstrated that the average density of parity crossings is described by the Weyl expansion. In the fully depleted limit of a disordered s-wave topological superconductor, the average density of parity crossings also features a Lifshitz tail. We also showed that the oscillations around the average density of parity crossings are described by the Gutzwiller's trace formula for conventional quantum billiards. Moreover, we found that the fermion parity crossings

spacings follow a universal distribution, determined by the dynamics in the normal limit. Lastly, we demonstrated that the eigenfunctions of a chaotic Majorana billiard feature quantum scars.

Bibliography

[1] A. M. Bozkurt, B. Pekerten, and İ. Adagideli, "Work extraction and Landauer's principle in a quantum spin Hall device," *Physical Review B*, vol. 97, p. 245414, June 2018. Publisher: American Physical Society.

[2] İ. Adagideli, A. M. Bozkurt, and B. Pekerten, "Implementing Maxwell's demon in spintronics devices," in *Spintronics XIII* (H.-J. M. Drouhin, J.-E. Wegrowe, and M. Razeghi, eds.), vol. 11470, International Society for Optics and Photonics, SPIE, 2020.

[3] B. Pekerten, A. M. Bozkurt, and İ. Adagideli, "Fermion parity switches of the ground state of Majorana billiards," *Physical Review B*, vol. 100, p. 235455, Dec. 2019.

[4] K. Maruyama, F. Nori, and V. Vedral, "Colloquium: The physics of Maxwell's demon and information," *Reviews of Modern Physics*, vol. 81, pp. 1–23, Jan. 2009. Publisher: American Physical Society.

[5] H. Leff and A. F. Rex, *Maxwell's Demon 2 Entropy, Classical and Quantum Information, Computing*. CRC Press, Dec. 2002.

[6] L. Szilard, "über die Entropieverminderung in einem thermodynamischen System bei Eingriffen intelligenter Wesen," *Zeitschrift für Physik*, vol. 53, pp. 840–856, Nov. 1929.

[7] R. Landauer, "Irreversibility and Heat Generation in the Computing Process," *IBM Journal of Research and Development*, vol. 5, pp. 183–191, July 1961. Conference Name: IBM Journal of Research and Development.

[8] S. Lloyd, "Quantum-mechanical Maxwell's demon," *Physical Review A*, vol. 56, pp. 3374–3382, Nov. 1997. Publisher: American Physical Society.

[9] M. O. Scully, "Extracting Work from a Single Thermal Bath via Quantum Negentropy," *Physical Review Letters*, vol. 87, p. 220601, Nov. 2001. Publisher: American Physical Society.

[10] T. D. Kieu, "The Second Law, Maxwell's Demon, and Work Derivable from Quantum Heat Engines," *Physical Review Letters*, vol. 93, p. 140403, Sept. 2004. Publisher: American Physical Society.

[11] J. A. Vaccaro and S. M. Barnett, "Information erasure without an energy cost," *Proceedings of the Royal Society A: Mathematical, Physical and Engineering Sciences*, vol. 467, pp. 1770–1778, June 2011. Publisher: Royal Society.

[12] S. M. Barnett and J. A. Vaccaro, "Beyond Landauer Erasure," *Entropy*, vol. 15, pp. 4956–4968, Nov. 2013. Number: 11 Publisher: Multidisciplinary Digital Publishing Institute.

[13] T. Croucher, S. Bedkihal, and J. A. Vaccaro, "Discrete Fluctuations in Memory Erasure without Energy Cost," *Physical Review Letters*, vol. 118, p. 060602, Feb. 2017. Publisher: American Physical Society.

[14] Z. Tang and P. Sheng, eds., *Nanoscale Phenomena: Basic Science to Device Applications*. Lecture Notes in Nanoscale Science and Technology, New York: Springer-Verlag, 2008.

[15] R. Bustos-Marún, G. Refael, and F. von Oppen, "Adiabatic Quantum Motors," *Physical Review Letters*, vol. 111, p. 060802, Aug. 2013. Publisher: American Physical Society.

[16] L. Arrachea and F. von Oppen, "Nanomagnet coupled to quantum spin Hall edge: An adiabatic quantum motor," *Physica E: Low-dimensional Systems and Nanostructures*, vol. 74, pp. 596–602, Nov. 2015.

[17] S. Hilt, S. Shabbir, J. Anders, and E. Lutz, "Landauer's principle in the quantum regime," *Physical Review E*, vol. 83, p. 030102, Mar. 2011. Publisher: American Physical Society.

[18] D. Mandal, H. T. Quan, and C. Jarzynski, "Maxwell's Refrigerator: An Exactly Solvable Model," *Physical Review Letters*, vol. 111, p. 030602, July 2013. Publisher: American Physical Society.

[19] A. C. Barato and U. Seifert, "An autonomous and reversible Maxwell's demon," *EPL (Europhysics Letters)*, vol. 101, p. 60001, Mar. 2013. Publisher: IOP Publishing.

[20] P. Strasberg, G. Schaller, T. Brandes, and M. Esposito, "Thermodynamics of a Physical Model Implementing a Maxwell Demon," *Physical Review Letters*, vol. 110, p. 040601, Jan. 2013. Publisher: American Physical Society.

[21] J. M. Horowitz, T. Sagawa, and J. M. R. Parrondo, "Imitating Chemical Motors with Optimal Information Motors," *Physical Review Letters*, vol. 111, p. 010602, July 2013. Publisher: American Physical Society.

[22] S. Deffner, "Information-driven current in a quantum Maxwell demon," *Physical Review E*, vol. 88, no. 6, 2013.

[23] J. J. Park, K.-H. Kim, T. Sagawa, and S. W. Kim, "Heat Engine Driven by Purely Quantum Information," *Physical Review Letters*, vol. 111, p. 230402, Dec. 2013. Publisher: American Physical Society.

[24] J. Roßnagel, O. Abah, F. Schmidt-Kaler, K. Singer, and E. Lutz, "Nanoscale Heat Engine Beyond the Carnot Limit," *Physical Review Letters*, vol. 112, p. 030602, Jan. 2014. Publisher: American Physical Society.

[25] P. Strasberg, G. Schaller, T. Brandes, and C. Jarzynski, "Second laws for an information driven current through a spin valve," *Physical Review E*, vol. 90, p. 062107, Dec. 2014. Publisher: American Physical Society.

[26] J. Gemmer and J. Anders, "From single-shot towards general work extraction in a quantum thermodynamic framework," *New Journal of Physics*, vol. 17, p. 085006, Aug. 2015. Publisher: IOP Publishing.

[27] J. P. Pekola, D. S. Golubev, and D. V. Averin, "Maxwell's demon based on a single qubit," *Physical Review B*, vol. 93, p. 024501, Jan. 2016. Publisher: American Physical Society.

[28] A. Kutvonen, J. Koski, and T. Ala-Nissila, "Thermodynamics and efficiency of an autonomous on-chip Maxwell's demon," *Scientific Reports*, vol. 6, pp. 1–7, Feb. 2016. Number: 1 Publisher: Nature Publishing Group.

[29] A. V. Lebedev, D. Oehri, G. B. Lesovik, and G. Blatter, "Trading coherence and entropy by a quantum Maxwell demon," *Physical Review A*, vol. 94, p. 052133, Nov. 2016. Publisher: American Physical Society.

[30] M. Campisi, J. Pekola, and R. Fazio, "Feedback-controlled heat transport in quantum devices: theory and solid-state experimental proposal," *New Journal of Physics*, vol. 19, p. 053027, May 2017. Publisher: IOP Publishing.

[31] C. Elouard, D. Herrera-Martí, B. Huard, and A. Auffèves, "Extracting Work from Quantum Measurement in Maxwell's Demon Engines," *Physical Review Letters*, vol. 118, p. 260603, June 2017. Publisher: American Physical Society.

[32] G. Rosselló, R. López, and G. Platero, "Chiral Maxwell demon in a quantum Hall system with a localized impurity," *Physical Review B*, vol. 96, p. 075305, Aug. 2017. Publisher: American Physical Society.

[33] G. Schaller, J. Cerrillo, G. Engelhardt, and P. Strasberg, "Electronic Maxwell demon in the coherent strong-coupling regime," *Physical Review B*, vol. 97, p. 195104, May 2018.

[34] N. Cottet and B. Huard, "Maxwell's Demon in Superconducting Circuits," in *Thermodynamics in the Quantum Regime: Fundamental Aspects and New Directions* (F. Binder, L. A. Correa, C. Gogolin, J. Anders, and G. Adesso, eds.), Fundamental Theories of Physics, pp. 959–981, Cham: Springer International Publishing, 2018.

[35] B. Annby-Andersson, P. Samuelsson, V. F. Maisi, and P. P. Potts, "Maxwell's demon in a double quantum dot with continuous charge detection," *Physical Review B*, vol. 101, p. 165404, Apr. 2020.

[36] S. Toyabe, T. Sagawa, M. Ueda, E. Muneyuki, and M. Sano, "Experimental demonstration of information-to-energy conversion and validation of the generalized Jarzynski equality," *Nature Physics*, vol. 6, pp. 988–992, Dec. 2010. Number: 12 Publisher: Nature Publishing Group.

[37] A. Bérut, A. Arakelyan, A. Petrosyan, S. Ciliberto, R. Dillenschneider, and E. Lutz, "Experimental verification of Landauer's principle linking information and thermodynamics," *Nature*, vol. 483, pp. 187–189, Mar. 2012. Number: 7388 Publisher: Nature Publishing Group.

[38] É. Roldán, I. A. Martínez, J. M. R. Parrondo, and D. Petrov, "Universal features in the energetics of symmetry breaking," *Nature Physics*, vol. 10, pp. 457–461, June 2014. Number: 6 Publisher: Nature Publishing Group.

[39] M. D. Vidrighin, O. Dahlsten, M. Barbieri, M. S. Kim, V. Vedral, and I. A. Walmsley, "Photonic Maxwell's Demon," *Physical Review Letters*, vol. 116, p. 050401, Feb. 2016. Publisher: American Physical Society.

[40] M. A. Ciampini, L. Mancino, A. Orieux, C. Vigliar, P. Mataloni, M. Paternostro, and M. Barbieri, "Experimental extractable work-based multipartite separability criteria," *npj Quantum Information*, vol. 3, pp. 1–6, Mar. 2017. Number: 1 Publisher: Nature Publishing Group.

[41] P. A. Camati, J. P. S. Peterson, T. B. Batalhão, K. Micadei, A. M. Souza, R. S. Sarthour, I. S. Oliveira, and R. M. Serra, "Experimental Rectification of Entropy Production by Maxwell's Demon in a Quantum System," *Physical Review Letters*, vol. 117, p. 240502, Dec. 2016. Publisher: American Physical Society.

[42] J. P. S. Peterson, R. S. Sarthour, A. M. Souza, I. S. Oliveira, J. Goold, K. Modi, D. O. Soares-Pinto, and L. C. Céleri, "Experimental demonstration of information to energy conversion in a quantum system at the Landauer limit," *Proceedings of the Royal Society A: Mathematical, Physical and Engineering Sciences*, vol. 472, p. 20150813, Apr. 2016. Publisher: Royal Society.

[43] J. V. Koski, "Experimental Observation of the Role of Mutual Information in the Nonequilibrium Dynamics of a Maxwell Demon," *Physical Review Letters*, vol. 113, no. 3, 2014.

[44] J. V. Koski, V. F. Maisi, J. P. Pekola, and D. V. Averin, "Experimental realization of a Szilard engine with a single electron," *Proceedings of the National Academy of Sciences*, vol. 111, pp. 13786–13789, Sept. 2014. Publisher: National Academy of Sciences Section: Physical Sciences.

[45] J. V. Koski, A. Kutvonen, I. M. Khaymovich, T. Ala-Nissila, and J. P. Pekola, "On-Chip Maxwell's Demon as an Information-Powered Refrigerator," *Physical Review Letters*, vol. 115, p. 260602, Dec. 2015. Publisher: American Physical Society.

[46] K. Chida, S. Desai, K. Nishiguchi, and A. Fujiwara, "Power generator driven by Maxwell's demon," *Nature Communications*, vol. 8, pp. 1–7, May 2017. Number: 1 Publisher: Nature Publishing Group.

[47] N. Cottet, S. Jezouin, L. Bretheau, P. Campagne-Ibarcq, Q. Ficheux, J. Anders, A. Auffèves, R. Azouit, P. Rouchon, and B. Huard, "Observing a quantum Maxwell demon at work," *Proceedings of the National Academy of Sciences*, vol. 114, pp. 7561–7564, July 2017. Publisher: National Academy of Sciences Section: Physical Sciences.

[48] M. König, S. Wiedmann, C. Brüne, A. Roth, H. Buhmann, L. W. Molenkamp, X.-L. Qi, and S.-C. Zhang, "Quantum Spin Hall Insulator State in HgTe Quantum Wells," *Science*, vol. 318, pp. 766–770, Nov. 2007. Publisher: American Association for the Advancement of Science Section: Research Article.

[49] B. A. Bernevig, T. L. Hughes, and S.-C. Zhang, "Quantum Spin Hall Effect and Topological Phase Transition in HgTe Quantum Wells," *Science*, vol. 314, pp. 1757–1761, Dec. 2006. Publisher: American Association for the Advancement of Science Section: Report.

[50] C. Liu, T. L. Hughes, X.-L. Qi, K. Wang, and S.-C. Zhang, "Quantum Spin Hall Effect in Inverted Type-II Semiconductors," *Physical Review Letters*, vol. 100, p. 236601, June 2008. Publisher: American Physical Society.

[51] L. Du, I. Knez, G. Sullivan, and R.-R. Du, "Robust Helical Edge Transport in Gated InAs/GaSb Bilayers," *Physical Review Letters*, vol. 114, p. 096802, Mar. 2015. Publisher: American Physical Society.

[52] Z. Fei, T. Palomaki, S. Wu, W. Zhao, X. Cai, B. Sun, P. Nguyen, J. Finney, X. Xu, and D. H. Cobden, "Edge conduction in monolayer WTe 2," *Nature Physics*, vol. 13, pp. 677–682, July 2017.

[53] S. Wu, V. Fatemi, Q. D. Gibson, K. Watanabe, T. Taniguchi, R. J. Cava, and P. Jarillo-Herrero, "Observation of the quantum spin Hall effect up to 100 kelvin in a monolayer crystal," *Science*, vol. 359, pp. 76–79, Jan. 2018.

[54] M. König, H. Buhmann, L. W. Molenkamp, T. Hughes, C.-X. Liu, X.-L. Qi, and S.-C. Zhang, "The Quantum Spin Hall Effect: Theory and Experiment," *Journal of the Physical Society of Japan*, vol. 77, p. 031007, Mar. 2008. Publisher: The Physical Society of Japan.

[55] A. M. Lunde and G. Platero, "Helical edge states coupled to a spin bath: Current-induced magnetization," *Physical Review B*, vol. 86, p. 035112, July 2012. Publisher: American Physical Society.

[56] V. Cheianov and L. I. Glazman, "Mesoscopic Fluctuations of Conductance of a Helical Edge Contaminated by Magnetic Impurities," *Physical Review Letters*, vol. 110, p. 206803, May 2013. Publisher: American Physical Society.

[57] A. Del Maestro, T. Hyart, and B. Rosenow, "Backscattering between helical edge states via dynamic nuclear polarization," *Physical Review B*, vol. 87, p. 165440, Apr. 2013. Publisher: American Physical Society.

[58] L. Kimme, B. Rosenow, and A. Brataas, "Backscattering in helical edge states from a magnetic impurity and Rashba disorder," *Physical Review B*, vol. 93, p. 081301, Feb. 2016. Publisher: American Physical Society.

[59] C.-H. Hsu, P. Stano, J. Klinovaja, and D. Loss, "Nuclear-spin-induced localization of edge states in two-dimensional topological insulators," *Physical Review B*, vol. 96, p. 081405, Aug. 2017. Publisher: American Physical Society.

[60] C. Liu and S. Zhang, "Chapter 3 - Models and Materials for Topological Insulators," in *Contemporary Concepts of Condensed Matter Science* (M. Franz and L. Molenkamp, eds.), vol. 6 of *Topological Insulators*, pp. 59–89, Elsevier, Jan. 2013.

[61] A. M. Lunde and G. Platero, "Hyperfine interactions in two-dimensional HgTe topological insulators," *Physical Review B*, vol. 88, p. 115411, Sept. 2013. Publisher: American Physical Society.

[62] İ. Adagideli, V. Lutsker, M. Scheid, P. Jacquod, and K. Richter, "Spin Transistor Action from Hidden Onsager Reciprocity," *Physical Review Letters*, vol. 108, p. 236601, June 2012. Publisher: American Physical Society.

[63] C. P. Slichter, *Principles of Magnetic Resonance*. Springer Series in Solid-State Sciences, Berlin Heidelberg: Springer-Verlag, third ed., 1990.

[64] M. A. Ruderman and C. Kittel, "Indirect Exchange Coupling of Nuclear Magnetic Moments by Conduction Electrons," *Physical Review*, vol. 96, pp. 99–102, Oct. 1954.

[65] C. W. Lai, P. Maletinsky, A. Badolato, and A. Imamoglu, "Knight-Field-Enabled Nuclear Spin Polarization in Single Quantum Dots," *Physical Review Letters*, vol. 96, p. 167403, Apr. 2006.

[66] R. I. Dzhioev and V. L. Korenev, "Stabilization of the Electron-Nuclear Spin Orientation in Quantum Dots by the Nuclear Quadrupole Interaction," *Physical Review Letters*, vol. 99, p. 037401, July 2007. Publisher: American Physical Society.

[67] S. Datta and B. Das, "Electronic analog of the electro-optic modulator," *Applied Physics Letters*, vol. 56, pp. 665–667, Feb. 1990. Publisher: American Institute of Physics.

[68] G. Schmidt, D. Ferrand, L. W. Molenkamp, A. T. Filip, and B. J. van Wees, "Fundamental obstacle for electrical spin injection from a ferromagnetic metal into a diffusive semiconductor," *Physical Review B*, vol. 62, pp. R4790–R4793, Aug. 2000. Publisher: American Physical Society.

[69] R. S. Whitney, "Thermodynamic and quantum bounds on nonlinear dc thermoelectric transport," *Physical Review B*, vol. 87, p. 115404, Mar. 2013.

[70] N. Nagaosa, "Emergent inductor by spiral magnets," *Japanese Journal of Applied Physics*, vol. 58, p. 120909, Nov. 2019.

[71] M. Z. Hasan and C. L. Kane, "Colloquium: Topological insulators," *Reviews of Modern Physics*, vol. 82, pp. 3045–3067, Nov. 2010. Publisher: American Physical Society.

[72] X.-L. Qi and S.-C. Zhang, "Topological insulators and superconductors," *Reviews of Modern Physics*, vol. 83, pp. 1057–1110, Oct. 2011. Publisher: American Physical Society.

[73] X. Qian, J. Liu, L. Fu, and J. Li, "Quantum spin Hall effect in two-dimensional transition metal dichalcogenides," *Science*, vol. 346, pp. 1344–1347, Dec. 2014.

[74] S. Tang, C. Zhang, D. Wong, Z. Pedramrazi, H.-Z. Tsai, C. Jia, B. Moritz, M. Claassen, H. Ryu, S. Kahn, J. Jiang, H. Yan, M. Hashimoto, D. Lu, R. G. Moore, C.-C. Hwang, C. Hwang, Z. Hussain, Y. Chen, M. M. Ugeda, Z. Liu, X. Xie, T. P. Devereaux, M. F. Crommie, S.-K. Mo, and Z.-X. Shen, "Quantum spin Hall state in monolayer 1T'-WTe 2," *Nature Physics*, vol. 13, pp. 683–687, July 2017.

[75] I. D. Avdeev and D. S. Smirnov, "Hyperfine interaction in atomically thin transition metal dichalcogenides," *Nanoscale Advances*, vol. 1, pp. 2624–2632, July 2019.

[76] F. Nichele, H. J. Suominen, M. Kjaergaard, C. M. Marcus, E. Sajadi, J. A. Folk, F. Qu, A. J. A. Beukman, F. K. de Vries, J. van Veen, S. Nadj-Perge, L. P. Kouwenhoven, B.-M. Nguyen, A. A. Kiselev, W. Yi, M. Sokolich, M. J. Manfra, E. M. Spanton, and K. A. Moler, "Edge transport in the trivial phase of InAs/GaSb," *New Journal of Physics*, vol. 18, p. 083005, July 2016.

[77] F. Reis, G. Li, L. Dudy, M. Bauernfeind, S. Glass, W. Hanke, R. Thomale, J. Schäfer, and R. Claessen, "Bismuthene on a SiC substrate: A candidate for a high-temperature quantum spin Hall material," *Science*, vol. 357, pp. 287–290, July 2017.

[78] J. Tian, S. Hong, I. Miotkowski, S. Datta, and Y. P. Chen, "Observation of current-induced, long-lived persistent spin polarization in a topological insulator: A rechargeable spin battery," *Science Advances*, vol. 3, p. e1602531, Apr. 2017. Publisher: American Association for the Advancement of Science Section: Research Article.

[79] S.-Y. Xu, L. A. Wray, Y. Xia, R. Shankar, A. Petersen, A. Fedorov, H. Lin, A. Bansil, Y. S. Hor, D. Grauer, R. J. Cava, and M. Z. Hasan, "Discovery of several large families of Topological Insulator classes with backscattering-suppressed spin-polarized single-Dirac-cone on the surface," *arXiv:1007.5111 [cond-mat, physics:physics, physics:quant-ph]*, July 2010. arXiv: 1007.5111.

[80] G. Benenti, G. Casati, K. Saito, and R. S. Whitney, "Fundamental aspects of steady-state conversion of heat to work at the nanoscale," *Physics Reports*, 2017. Publisher: Elsevier.

[81] L. Chua, "Memristor-The missing circuit element," *IEEE Transactions on Circuit Theory*, vol. 18, pp. 507–519, Sept. 1971.

[82] D. B. Strukov, G. S. Snider, D. R. Stewart, and R. S. Williams, "The missing memristor found," *Nature*, vol. 453, pp. 80–83, May 2008.

[83] Y. V. Pershin and M. Di Ventra, "Spin memristive systems: Spin memory effects in semiconductor spintronics," *Physical Review B*, vol. 78, p. 113309, Sept. 2008.

[84] A. Chanthbouala, V. Garcia, R. O. Cherifi, K. Bouzehouane, S. Fusil, X. Moya, S. Xavier, H. Yamada, C. Deranlot, N. D. Mathur, M. Bibes, A. Barthélémy, and J. Grollier, "A ferroelectric memristor," *Nature Materials*, vol. 11, pp. 860–864, Oct. 2012.

[85] A. A. Bessonov, M. N. Kirikova, D. I. Petukhov, M. Allen, T. Ryhänen, and M. J. A. Bailey, "Layered memristive and memcapacitive switches for printable electronics," *Nature Materials*, vol. 14, pp. 199–204, Feb. 2015.

[86] M. V. Il'ina, O. I. Il'in, Y. F. Blinov, V. A. Smirnov, A. S. Kolomiytsev, A. A. Fedotov, B. G. Konoplev, and O. A. Ageev, "Memristive switching mechanism of vertically aligned carbon nanotubes," *Carbon*, vol. 123, pp. 514–524, Oct. 2017.

[87] Y. V. Pershin and M. Di Ventra, "Current-voltage characteristics of semiconductor/ferromagnet junctions in the spin-blockade regime," *Physical Review B*, vol. 77, p. 073301, Feb. 2008.

[88] A. Chanthbouala, A. Crassous, V. Garcia, K. Bouzehouane, S. Fusil, X. Moya, J. Allibe, B. Dlubak, J. Grollier, S. Xavier, C. Deranlot, A. Moshar, R. Proksch, N. D. Mathur, M. Bibes, and A. Barthélémy, "Solid-state memories based on ferroelectric tunnel junctions," *Nature Nanotechnology*, vol. 7, pp. 101–104, Feb. 2012.

[89] Y. V. Pershin and M. D. Ventra, "A simple test for ideal memristors," *Journal of Physics D: Applied Physics*, vol. 52, p. 01LT01, Oct. 2018.

[90] M. D. Ventra and Y. V. Pershin, "On the physical properties of memristive, memcapacitive and meminductive systems," *Nanotechnology*, vol. 24, p. 255201, May 2013.

[91] L. Fu, C. L. Kane, and E. J. Mele, "Topological Insulators in Three Dimensions," *Physical Review Letters*, vol. 98, p. 106803, Mar. 2007.

[92] J. E. Moore and L. Balents, "Topological invariants of time-reversal-invariant band structures," *Physical Review B*, vol. 75, p. 121306, Mar. 2007.

[93] H. B. Nielsen and M. Ninomiya, "The Adler-Bell-Jackiw anomaly and Weyl fermions in a crystal," *Physics Letters B*, vol. 130, pp. 389–396, Nov. 1983.

[94] A. A. Burkov and D. G. Hawthorn, "Spin and Charge Transport on the Surface of a Topological Insulator," *Physical Review Letters*, vol. 105, p. 066802, Aug. 2010.

[95] P. Schwab, R. Raimondi, and C. Gorini, "Spin-charge locking and tunneling into a helical metal," *EPL (Europhysics Letters)*, vol. 93, p. 67004, Mar. 2011.

[96] X. Liu and J. Sinova, "Reading Charge Transport from the Spin Dynamics on the Surface of a Topological Insulator," *Physical Review Letters*, vol. 111, p. 166801, Oct. 2013.

[97] J. Rammer, "Quantum field-theoretical methods in transport theory of metals," *Reviews of Modern Physics*, vol. 58, no. 2, pp. 323–359, 1986.

[98] C. L. Kane and E. J. Mele, "Quantum Spin Hall Effect in Graphene," *Physical Review Letters*, vol. 95, p. 226801, Nov. 2005. Publisher: American Physical Society.

[99] A. Altland and M. R. Zirnbauer, "Nonstandard symmetry classes in mesoscopic normal-superconducting hybrid structures," *Physical Review B*, vol. 55, pp. 1142–1161, Jan. 1997.

[100] S. Ryu, A. P. Schnyder, A. Furusaki, and A. W. W. Ludwig, "Topological insulators and superconductors: tenfold way and dimensional hierarchy," *New Journal of Physics*, vol. 12, p. 065010, June 2010. Publisher: IOP Publishing.

[101] L. Fu and C. L. Kane, "Josephson current and noise at a superconductor/quantum-spin-Hall-insulator/superconductor junction," *Physical Review B*, vol. 79, p. 161408, Apr. 2009. Publisher: American Physical Society.

[102] T. D. Stanescu, R. M. Lutchyn, and S. Das Sarma, "Majorana fermions in semiconductor nanowires," *Physical Review B*, vol. 84, p. 144522, Oct. 2011. Publisher: American Physical Society.

[103] E. J. H. Lee, X. Jiang, R. Aguado, G. Katsaros, C. M. Lieber, and S. De Franceschi, "Zero-Bias Anomaly in a Nanowire Quantum Dot Coupled to Superconductors," *Physical Review Letters*, vol. 109, p. 186802, Oct. 2012. Publisher: American Physical Society.

[104] C. W. J. Beenakker, J. M. Edge, J. P. Dahlhaus, D. I. Pikulin, S. Mi, and M. Wimmer, "Wigner-Poisson Statistics of Topological Transitions in a Josephson Junction," *Physical Review Letters*, vol. 111, p. 037001, July 2013. Publisher: American Physical Society.

[105] M.-T. Rieder, P. W. Brouwer, and İ. Adagideli, "Reentrant topological phase transitions in a disordered spinless superconducting wire," *Physical Review B*, vol. 88, p. 060509, Aug. 2013. Publisher: American Physical Society.

[106] W. Chang, V. E. Manucharyan, T. S. Jespersen, J. Nygård, and C. M. Marcus, "Tunneling Spectroscopy of Quasiparticle Bound States in a Spinful Josephson Junction," *Physical Review Letters*, vol. 110, p. 217005, May 2013. Publisher: American Physical Society.

[107] J. D. Sau and E. Demler, "Bound states at impurities as a probe of topological superconductivity in nanowires," *Physical Review B*, vol. 88, p. 205402, Nov. 2013. Publisher: American Physical Society.

[108] D. M. Badiane, L. I. Glazman, M. Houzet, and J. S. Meyer, "Ac Josephson effect in topological Josephson junctions," *Comptes Rendus Physique*, vol. 14, pp. 840–856, Nov. 2013.

[109] D. Chevallier, P. Simon, and C. Bena, "From Andreev bound states to Majorana fermions in topological wires on superconducting substrates: A story of mutation," *Physical Review B*, vol. 88, p. 165401, Oct. 2013. Publisher: American Physical Society.

[110] E. J. H. Lee, X. Jiang, M. Houzet, R. Aguado, C. M. Lieber, and S. De Franceschi, "Spin-resolved Andreev levels and parity crossings in hybrid superconductor–semiconductor nanostructures," *Nature Nanotechnology*, vol. 9, pp. 79–84, Jan. 2014. Number: 1 Publisher: Nature Publishing Group.

[111] S. Hegde, V. Shivamoggi, S. Vishveshwara, and D. Sen, "Quench dynamics and parity blocking in Majorana wires," *New Journal of Physics*, vol. 17, p. 053036, May 2015. Publisher: IOP Publishing.

[112] A. Y. Kitaev, "Unpaired Majorana fermions in quantum wires," *Physics-Uspekhi*, vol. 44, pp. 131–136, Oct. 2001. Publisher: Uspekhi Fizicheskikh Nauk (UFN) Journal.

[113] J. Alicea, "New directions in the pursuit of Majorana fermions in solid state systems," *Reports on Progress in Physics*, vol. 75, p. 076501, June 2012. Publisher: IOP Publishing.

[114] B. A. Bernevig and T. L. Hughes, *Topological Insulators and Topological Superconductors*. Princeton: Princeton University Press, illustrated edition ed., Apr. 2013.

[115] S. R. Elliott and M. Franz, "Colloquium: Majorana fermions in nuclear, particle, and solid-state physics," *Reviews of Modern Physics*, vol. 87, pp. 137–163, Feb. 2015. Publisher: American Physical Society.

[116] R. M. Lutchyn, J. D. Sau, and S. Das Sarma, "Majorana Fermions and a Topological Phase Transition in Semiconductor-Superconductor Heterostructures," *Physical Review Letters*, vol. 105, p. 077001, Aug. 2010. Publisher: American Physical Society.

[117] Y. Oreg, G. Refael, and F. von Oppen, "Helical Liquids and Majorana Bound States in Quantum Wires," *Physical Review Letters*, vol. 105, p. 177002, Oct. 2010. Publisher: American Physical Society.

[118] P. G. De Gennes, *Superconductivity Of Metals And Alloys*. Reading, Mass: CRC Press, Mar. 1999.

[119] V. Mourik, K. Zuo, S. M. Frolov, S. R. Plissard, E. P. a. M. Bakkers, and L. P. Kouwenhoven, "Signatures of Majorana Fermions in Hybrid Superconductor-Semiconductor Nanowire Devices," *Science*, vol. 336, pp. 1003–1007, May 2012. Publisher: American Association for the Advancement of Science Section: Report.

[120] S. Nadj-Perge, I. K. Drozdov, J. Li, H. Chen, S. Jeon, J. Seo, A. H. MacDonald, B. A. Bernevig, and A. Yazdani, "Observation of Majorana fermions in ferromagnetic atomic chains on a superconductor," *Science*, vol. 346, pp. 602–607, Oct. 2014. Publisher: American Association for the Advancement of Science Section: Research Article.

[121] A. Fornieri, A. M. Whiticar, F. Setiawan, E. Portolés, A. C. C. Drachmann, A. Keselman, S. Gronin, C. Thomas, T. Wang, R. Kallaher, G. C. Gardner, E. Berg, M. J. Manfra, A. Stern, C. M. Marcus, and F. Nichele, "Evidence of topological superconductivity in planar Josephson junctions," *Nature*, vol. 569, pp. 89–92, May 2019.

[122] S. Vaitiekėnas, G. W. Winkler, B. v. Heck, T. Karzig, M.-T. Deng, K. Flensberg, L. I. Glazman, C. Nayak, P. Krogstrup, R. M. Lutchyn, and C. M. Marcus, "Flux-induced topological superconductivity in full-shell nanowires," *Science*, vol. 367, Mar. 2020. Publisher: American Association for the Advancement of Science Section: Research Article.

[123] T. H. Hsieh and L. Fu, "Majorana Fermions and Exotic Surface Andreev Bound States in Topological Superconductors: Application to $\mathrm{Cu}_x\mathrm{Bi}_2\mathrm{Se}_3$," *Physical Review Letters*, vol. 108, p. 107005, Mar. 2012. Publisher: American Physical Society.

[124] E. Prada, P. San-Jose, and R. Aguado, "Transport spectroscopy of NS nanowire junctions with Majorana fermions," *Physical Review B*, vol. 86, p. 180503, Nov. 2012. Publisher: American Physical Society.

[125] J. F. Silva and E. Vernek, "Andreev and Majorana bound states in single and double quantum dot structures," *Journal of Physics: Condensed Matter*, vol. 28, p. 435702, Sept. 2016. Publisher: IOP Publishing.

[126] C.-X. Liu, J. D. Sau, T. D. Stanescu, and S. Das Sarma, "Andreev bound states versus Majorana bound states in quantum dot-nanowire-superconductor hybrid structures: Trivial versus topological zero-bias conductance peaks," *Physical Review B*, vol. 96, p. 075161, Aug. 2017. Publisher: American Physical Society.

[127] F. Nichele, A. C. C. Drachmann, A. M. Whiticar, E. C. T. O'Farrell, H. J. Suominen, A. Fornieri, T. Wang, G. C. Gardner, C. Thomas, A. T. Hatke, P. Krogstrup, M. J. Manfra, K. Flensberg, and C. M. Marcus, "Scaling of Majorana Zero-Bias Conductance Peaks," *Physical Review Letters*, vol. 119, p. 136803, Sept. 2017. Publisher: American Physical Society.

[128] K. Zuo, V. Mourik, D. B. Szombati, B. Nijholt, D. J. van Woerkom, A. Geresdi, J. Chen, V. P. Ostroukh, A. R. Akhmerov, S. R. Plissard, D. Car, E. P. A. M. Bakkers, D. I. Pikulin, L. P. Kouwenhoven, and S. M. Frolov, "Supercurrent Interference in Few-Mode Nanowire Josephson Junctions," *Physical Review Letters*, vol. 119, p. 187704, Nov. 2017. Publisher: American Physical Society.

[129] H.-Z. Tang, Y.-T. Zhang, and J.-J. Liu, "Josephson current through a quantum dot molecule with a Majorana zero mode and Andreev bound states," *Physics Letters A*, vol. 382, pp. 991–994, Apr. 2018.

[130] C. Moore, C. Zeng, T. D. Stanescu, and S. Tewari, "Quantized zero-bias conductance plateau in semiconductor-superconductor heterostructures without topological Majorana zero modes," *Physical Review B*, vol. 98, p. 155314, Oct. 2018. Publisher: American Physical Society.

[131] M. Hell, K. Flensberg, and M. Leijnse, "Distinguishing Majorana bound states from localized Andreev bound states by interferometry," *Physical Review B*, vol. 97, p. 161401, Apr. 2018. Publisher: American Physical Society.

[132] C.-X. Liu, J. D. Sau, and S. Das Sarma, "Distinguishing topological Majorana bound states from trivial Andreev bound states: Proposed tests through differential tunneling conductance spectroscopy," *Physical Review B*, vol. 97, p. 214502, June 2018. Publisher: American Physical Society.

[133] A. Vuik, B. Nijholt, A. Akhmerov, and M. Wimmer, "Reproducing topological properties with quasi-Majorana states," *SciPost Physics*, vol. 7, p. 061, Nov. 2019.

[134] C. Moore, T. D. Stanescu, and S. Tewari, "Two-terminal charge tunneling: Disentangling Majorana zero modes from partially separated Andreev bound states in semiconductor-superconductor heterostructures," *Physical Review B*, vol. 97, p. 165302, Apr. 2018. Publisher: American Physical Society.

[135] C. Reeg, O. Dmytruk, D. Chevallier, D. Loss, and J. Klinovaja, "Zero-energy Andreev bound states from quantum dots in proximitized Rashba nanowires," *Physical Review B*, vol. 98, p. 245407, Dec. 2018. Publisher: American Physical Society.

[136] M. Kayyalha, M. Kargarian, A. Kazakov, I. Miotkowski, V. M. Galitski, V. M. Yakovenko, L. P. Rokhinson, and Y. P. Chen, "Anomalous Low-Temperature Enhancement of Supercurrent in Topological-Insulator Nanoribbon Josephson Junctions: Evidence for Low-Energy Andreev Bound States," *Physical Review Letters*, vol. 122, p. 047003, Feb. 2019. Publisher: American Physical Society.

[137] J. Chen, B. D. Woods, P. Yu, M. Hocevar, D. Car, S. R. Plissard, E. P. A. M. Bakkers, T. D. Stanescu, and S. M. Frolov, "Ubiquitous Non-Majorana Zero-Bias Conductance Peaks in Nanowire Devices," *Physical Review Letters*, vol. 123, p. 107703, Sept. 2019. Publisher: American Physical Society.

[138] B. D. Woods, J. Chen, S. M. Frolov, and T. D. Stanescu, "Zero-energy pinning of topologically trivial bound states in multiband semiconductor-superconductor nanowires," *Physical Review B*, vol. 100, p. 125407, Sept. 2019. Publisher: American Physical Society.

[139] Z. Cao, H. Zhang, H.-F. Lü, W.-X. He, H.-Z. Lu, and X. C. Xie, "Decays of Majorana or Andreev Oscillations Induced by Steplike Spin-Orbit Coupling," *Physical Review Letters*, vol. 122, p. 147701, Apr. 2019. Publisher: American Physical Society.

[140] N. Leumer, M. Grifoni, B. Muralidharan, and M. Marganska, "Linear and nonlinear transport across a finite Kitaev chain: An exact analytical study," *Physical Review B*, vol. 103, p. 165432, Apr. 2021.

[141] O. Motrunich, K. Damle, and D. A. Huse, "Griffiths effects and quantum critical points in dirty superconductors without spin-rotation invariance: One-dimensional examples," *Physical Review B*, vol. 63, p. 224204, May 2001. Publisher: American Physical Society.

[142] P. W. Brouwer, M. Duckheim, A. Romito, and F. von Oppen, "Probability Distribution of Majorana End-State Energies in Disordered Wires," *Physical Review Letters*, vol. 107, p. 196804, Nov. 2011. Publisher: American Physical Society.

[143] P. W. Brouwer, M. Duckheim, A. Romito, and F. von Oppen, "Topological superconducting phases in disordered quantum wires with strong spin-orbit coupling," *Physical Review B*, vol. 84, p. 144526, Oct. 2011. Publisher: American Physical Society.

[144] D. I. Pikulin, J. P. Dahlhaus, M. Wimmer, H. Schomerus, and C. W. J. Beenakker, "A zero-voltage conductance peak from weak antilocalization in a Majorana nanowire," *New Journal of Physics*, vol. 14, p. 125011, Dec. 2012. Publisher: IOP Publishing.

[145] M. Popinciuc, V. E. Calado, X. L. Liu, A. R. Akhmerov, T. M. Klapwijk, and L. M. K. Vandersypen, "Zero-bias conductance peak and Josephson effect in graphene-NbTiN junctions," *Physical Review B*, vol. 85, p. 205404, May 2012. Publisher: American Physical Society.

[146] D. Bagrets and A. Altland, "Class D Spectral Peak in Majorana Quantum Wires," *Physical Review Letters*, vol. 109, p. 227005, Nov. 2012. Publisher: American Physical Society.

[147] J. Liu, A. C. Potter, K. T. Law, and P. A. Lee, "Zero-Bias Peaks in the Tunneling Conductance of Spin-Orbit-Coupled Superconducting Wires with and without Majorana End-States," *Physical Review Letters*, vol. 109, p. 267002, Dec. 2012. Publisher: American Physical Society.

[148] P. Neven, D. Bagrets, and A. Altland, "Quasiclassical theory of disordered multichannel Majorana quantum wires," *New Journal of Physics*, vol. 15, p. 055019, May 2013. Publisher: IOP Publishing.

[149] H. O. H. Churchill, V. Fatemi, K. Grove-Rasmussen, M. T. Deng, P. Caroff, H. Q. Xu, and C. M. Marcus, "Superconductor-nanowire devices from tunneling to the multichannel regime: Zero-bias oscillations and magnetoconductance crossover," *Physical Review B*, vol. 87, p. 241401, June 2013. Publisher: American Physical Society.

[150] H. Pan, W. S. Cole, J. D. Sau, and S. Das Sarma, "Generic quantized zero-bias conductance peaks in superconductor-semiconductor hybrid structures," *Physical Review B*, vol. 101, p. 024506, Jan. 2020. Publisher: American Physical Society.

[151] S. Das Sarma, J. D. Sau, and T. D. Stanescu, "Splitting of the zero-bias conductance peak as smoking gun evidence for the existence of the Majorana mode in a superconductor-semiconductor nanowire," *Physical Review B*, vol. 86, p. 220506, Dec. 2012. Publisher: American Physical Society.

[152] R. Rodríguez-Mota, S. Vishveshwara, and T. Pereg-Barnea, "Detecting Majorana modes through Josephson junction ring-quantum dot hybrid architectures," *Journal of Physics and Chemistry of Solids*, vol. 128, pp. 179–187, May 2019.

[153] M. Kac, "Can One Hear the Shape of a Drum?," *The American Mathematical Monthly*, vol. 73, pp. 1–23, Apr. 1966. Publisher: Taylor & Francis.

[154] I. Kosztin, D. L. Maslov, and P. M. Goldbart, "Chaos in Andreev Billiards," *Physical Review Letters*, vol. 75, pp. 1735–1738, Aug. 1995. Publisher: American Physical Society.

[155] İ. Adagideli and P. M. Goldbart, "Quantal Andreev billiards: Density of states oscillations and the spectrum-geometry relationship," *Physical Review B*, vol. 65, p. 201306, May 2002. Publisher: American Physical Society.

[156] C. Beenakker, "Andreev billiards," in *Quantum Dots: A Doorway to Nanoscale Physics* (W. Dieter Heiss, ed.), pp. 131–174, Berlin, Heidelberg: Springer Berlin Heidelberg, 2005.

[157] R. Balian and C. Bloch, "Distribution of eigenfrequencies for the wave equation in a finite domain: I. Three-dimensional problem with smooth boundary surface," *Annals of Physics*, vol. 60, pp. 401–447, Oct. 1970.

[158] M. Brack, R. Bhaduri, and R. K. Bhaduri, *Semiclassical Physics*. Boulder, Colo.: CRC Press, Jan. 2003.

[159] R. Balian and C. Bloch, "Distribution of eigenfrequencies for the wave equation in a finite domain: III. Eigenfrequency density oscillations," *Annals of Physics*, vol. 69, pp. 76–160, Jan. 1972.

[160] M. V. Berry, "Semiclassical theory of spectral rigidity," *Proceedings of the Royal Society of London. A. Mathematical and Physical Sciences*, vol. 400, pp. 229–251, Aug. 1985. Publisher: Royal Society.

[161] M. C. Gutzwiller, *Chaos in Classical and Quantum Mechanics*. Interdisciplinary Applied Mathematics, New York: Springer-Verlag, 1990.

[162] H. Baltes and E. Hilf, "Spectra of finite systems : A review of weyl's problem, the eigenvalue distribution of the wave equation for finite domains and its applications on the physics of small systems," 1976.

[163] M. L. Mehta, *Random Matrices, Volume 142, Third Edition*. Academic Press, 3rd edition ed., Nov. 2004.

[164] J. Wurm, A. Rycerz, İ. Adagideli, M. Wimmer, K. Richter, and H. U. Baranger, "Symmetry Classes in Graphene Quantum Dots: Universal Spectral Statistics, Weak Localization, and Conductance Fluctuations," *Physical Review Letters*, vol. 102, p. 056806, Feb. 2009. Publisher: American Physical Society.

[165] İ. Adagideli, M. Wimmer, and A. Teker, "Effects of electron scattering on the topological properties of nanowires: Majorana fermions from disorder and superlattices," *Physical Review B*, vol. 89, p. 144506, Apr. 2014. Publisher: American Physical Society.

[166] H. Weyl, *Gesammelte Abhandlungen IV*. Springer Collected Works in Mathematics, Berlin Heidelberg: Springer-Verlag, 1968.

[167] R. A. Jalabert, H. U. Baranger, and A. D. Stone, "Conductance fluctuations in the ballistic regime: A probe of quantum chaos?," *Physical Review Letters*, vol. 65, pp. 2442–2445, Nov. 1990. Publisher: American Physical Society.

[168] H. Ishio and J. Burgdörfer, "Quantum conductance fluctuations and classical short-path dynamics," *Physical Review B*, vol. 51, pp. 2013–2016, Jan. 1995. Publisher: American Physical Society.

[169] İ. Adagideli and P. M. Goldbart, "Quantal andreev billiards: semiclassical approach to mesoscale oscillations in the density of states," *International Journal of Modern Physics B*, vol. 16, pp. 1381–1458, Apr. 2002. Publisher: World Scientific Publishing Co.

[170] I. M. Lifshitz, "The energy spectrum of disordered systems," *Advances in Physics*, vol. 13, pp. 483–536, Oct. 1964. Publisher: Taylor & Francis.

[171] B. I. Halperin, "Green's Functions for a Particle in a One-Dimensional Random Potential," *Physical Review*, vol. 139, pp. A104–A117, July 1965. Publisher: American Physical Society.

[172] C. Itzykson, *Statistical Field Theory: Volume 2, Strong Coupling, Monte Carlo Methods, Conformal Field Theory and Random Systems*. Cambridge: Cambridge University Press, Mar. 1991.

[173] C. W. J. Beenakker, "Random-matrix theory of quantum transport," *Reviews of Modern Physics*, vol. 69, pp. 731–808, July 1997. Publisher: American Physical Society.

[174] B. Pekerten, A. Teker, Ö. Bozat, M. Wimmer, and İ. Adagideli, "Disorder-induced topological transitions in multichannel Majorana wires," *Physical Review B*, vol. 95, p. 064507, Feb. 2017. Publisher: American Physical Society.

[175] B. Scharf and I. Žutić, "Probing Majorana-like states in quantum dots and quantum rings," *Physical Review B*, vol. 91, p. 144505, Apr. 2015. Publisher: American Physical Society.

[176] B. I. Shklovskii, B. Shapiro, B. R. Sears, P. Lambrianides, and H. B. Shore, "Statistics of spectra of disordered systems near the metal-insulator transition," *Physical Review B*, vol. 47, pp. 11487–11490, May 1993. Publisher: American Physical Society.

[177] E. P. Wigner, "Characteristic Vectors of Bordered Matrices With Infinite Dimensions," *Annals of Mathematics*, vol. 62, no. 3, pp. 548–564, 1955. Publisher: Annals of Mathematics.

[178] F. J. Dyson, "Statistical Theory of the Energy Levels of Complex Systems. II," *Journal of Mathematical Physics*, vol. 3, pp. 157–165, Jan. 1962. Publisher: American Institute of Physics.

[179] F. J. Dyson, "The Threefold Way. Algebraic Structure of Symmetry Groups and Ensembles in Quantum Mechanics," *Journal of Mathematical Physics*, vol. 3, pp. 1199–1215, Nov. 1962.

[180] F. J. Dyson and M. L. Mehta, "Statistical Theory of the Energy Levels of Complex Systems. IV," *Journal of Mathematical Physics*, vol. 4, pp. 701–712, May 1963. Publisher: American Institute of Physics.

[181] E. J. Heller, "Bound-State Eigenfunctions of Classically Chaotic Hamiltonian Systems: Scars of Periodic Orbits," *Physical Review Letters*, vol. 53, no. 16, pp. 1515–1518, 1984.

[182] L. Kaplan, "Scars in quantum chaotic wavefunctions," *Nonlinearity*, vol. 12, pp. R1–R40, Jan. 1999.

[183] J. Rammer and H. Smith, "Quantum field-theoretical methods in transport theory of metals," *Reviews of Modern Physics*, vol. 58, pp. 323–359, Apr. 1986.

[184] T. T. Heikkilä, *The Physics of Nanoelectronics: Transport and Fluctuation Phenomena at Low Temperatures*. OUP Oxford, Jan. 2013.

[185] M. I. Dyakonov, ed., *Spin Physics in Semiconductors*. Springer Series in Solid-State Sciences, Berlin Heidelberg: Springer-Verlag, 2008.

[186] C. W. Groth, M. Wimmer, A. R. Akhmerov, and X. Waintal, "Kwant: a software package for quantum transport," *New Journal of Physics*, vol. 16, p. 063065, June 2014. Publisher: IOP Publishing.

[187] S. Datta, *Electronic Transport in Mesoscopic Systems*. Cambridge Studies in Semiconductor Physics and Microelectronic Engineering, Cambridge: Cambridge University Press, 1995.

[188] E. Jones, T. Oliphant, P. Peterson, *et al.*, "SciPy: Open source scientific tools for Python," 2001–.

Appendix A

OVERVIEW OF QUANTUM TRANSPORT

Mesoscopic systems are known to be ideal platforms for novel device applications, as they exhibit quantum effects. There are multitudinous examples of such devices that utilize charge and heat currents, the most notorious example being the transistor. Over the last two decades, the number of proposals for new device applications has increased very rapidly. Moreover, these proposals exploit new physical concepts, such as the Maxwell's demon, that requires a good understanding not only for the sake of fundamental physics but also for the purpose of designing more efficient and powerful devices. To that end, it is paramount to understand how and where the energy dissipation occurs in the system, making it essential to study the transport properties of these systems and understand how charge and heat currents flow.

In this appendix, we introduce the fundamental concepts and tools used in quantum transport and quantum thermodynamics of mesoscopic systems that are used in this thesis. We first review the nonequilibrium Green's function formalism in Section A.1. Next, we consider the semiclassical limit and investigate the basics of the semiclassical transport of noninteracting electrons in Section A.2 with particular focus on Boltzmann transport equation. Finally, in Section A.3, we discuss the heat and charge transport in mesoscopic systems that play essential role in quantum transport.

A.1 Nonequilibrium Green's Function Method

In this section, we briefly review the nonequlibrium Green's function method in order to obtain the transport equations for mesoscopic systems. For detailed discussion and calculations, we recommend the reader to review Ref. [97] and references within. The nonequilibrium nature of the transport problem requires one to make use of *contour-ordered* Green's function for fermions, which is defined as

$$G_c(1,1') = -i\langle \mathcal{T}_c \left(\psi(1)\psi^\dagger(1')\right)\rangle, \tag{A.1}$$

where $\mathcal{T}_c$ is the contour-ordering operator. We use the shorthand notation for space and

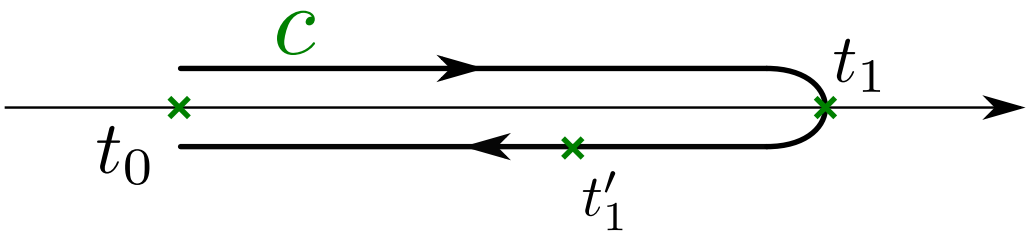

Figure A.1: The closed time path contour c.

time variables, namely $1 \equiv (\boldsymbol{x}_1, t_1)$. The abbreviation "1" can also include the other degrees of freedom such as spin or valley. The contour ordering operator orders the field operators given in Eq. (A.1) based on their position on the contour, which is set by the time arguments (see Fig. A.1).

In the absence of initial correlations, we can use the Keldysh formulation and map the contour ordered Green's function onto the Keldysh space:

$$G_c(1,1') \to \underline{G}(1,1') = \begin{bmatrix} G_{11} & G_{12} \\ G_{21} & G_{22} \end{bmatrix}, \tag{A.2}$$

The resulting Green's function in Keldysh space, which we denote as $\underline{G}$, has four dif-

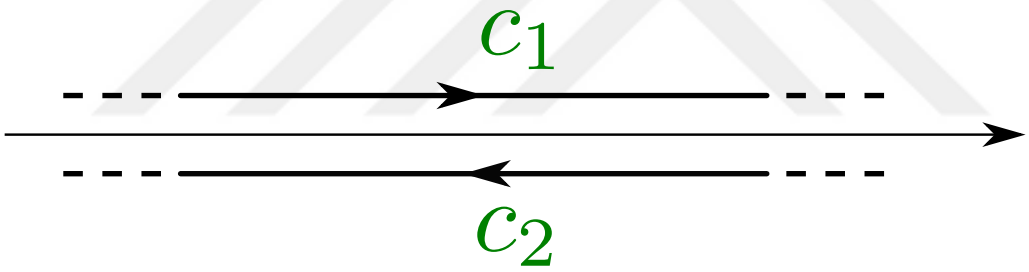

Figure A.2: The Keldysh contour c_K.

ferent components with subscripts ij define the field operators at t_1 and t_1' residing on the Keldysh contour c_i and c_j, respectively. We drop out the subscripts and define the conventional components of the Keldysh space Green's function:

$$\begin{aligned} G_{11} &\equiv G^{--}(1,1') = -i\langle \mathcal{T}\psi(1)\psi^\dagger(1'))\rangle; \\ G_{12} &\equiv G^{-+}(1,1') = +i\langle \psi^\dagger(1')\psi(1)\rangle; \\ G_{21} &\equiv G^{+-}((1,1') = -i\langle \psi(1)\psi^\dagger(1')\rangle; \\ G_{22} &\equiv G^{++}(1,1') = -i\langle \widetilde{\mathcal{T}}\psi(1)\psi^\dagger(1')\rangle, \end{aligned} \tag{A.3}$$

where $\mathcal{T}(\widetilde{\mathcal{T}})$ is the time ordering (anti-time ordering) operator and $G^{--}(G^{++})$ is the time ordered (anti-time ordered) Green's function, respectively. The remaining two Green's functions $G^{-+}(G^{+-})$ are called *lesser* (*greater*) Green's functions and are related to the quantum statistics of particles in the system. We note that these four Green's function are not independent:

$$G^{--}(1,1') + G^{++}(1,1') = G^{-+}(1,1') + G^{+-}(1,1'), \tag{A.4}$$

This property enables us to use a more advantageous representation of the Keldysh space Green's function $\underline{G}$, introduced by Larkin and Ovchinnikov [183]. The first step is to carry out a transformation in Keldysh space,

$$\underline{G} \to \tau_z \underline{G}, \tag{A.5}$$

and then we perform a rotation

$$\underline{G} \equiv L \underline{G}^{\dagger}, \tag{A.6}$$

where $L = 1/\sqrt{2}\,(\tau_0 - i\tau_y)$. Here τ_0 is the identity operator and τ_i are the Pauli matrices in Keldysh space. As a result, we obtain a representation of $\underline{G}$ such that there are three independent Green's functions, namely retarded, advanced and Keldysh Green's functions, G^R, G^A and G^K, respectively:

$$\begin{aligned} G^R(1,1') &= G^{--}(1,1') - G^{-+}(1,1') = G^{+-}(1,1') - G^{++}(1,1'), \\ G^A(1,1') &= G^{--}(1,1') - G^{+-}(1,1') = G^{-+}(1,1') - G^{++}(1,1'), \\ G^K(1,1') &= G^{--}(1,1') + G^{++}(1,1') = G^{-+}(1,1') + G^{+-}(1,1'). \end{aligned} \tag{A.7}$$

We can use the matrix representation of the nonequilibrium Green's function:

$$\underline{G} = \begin{bmatrix} G^R & G^K \\ 0 & G^A \end{bmatrix}. \tag{A.8}$$

The perturbation expansion for Keldysh space Green's function is structurally equivalent to the equilibrium theory, the only difference comes from the contour structure of the Keldysh space. Therefore, the diagrammatic formulation of the Keldysh technique is almost identical to the equilibrium diagrammatic formulation, except for the fact that the propagators and vertices contain contour indices. We refer the reader to Ref. [97] for a detailed calculation of the diagram rules for the Keldysh technique.

A.1.1 Dyson Equations

We now obtain the Dyson equation for the nonequilibrium Green's function, similar to the equilibrium theory [97]. The right-hand Dyson equation reads

$$\left(\underline{G}_0^{-1}(1,1') - \underline{\Sigma}\right) \otimes \underline{G} = \delta(1-1'), \tag{A.9}$$

where we use the shortened notation:

$$(A \otimes B)\,(1,1') = \int d\boldsymbol{x}_2 \int_{-\infty}^{+\infty} dt_2 A(1,2) B(2,1'). \tag{A.10}$$

In Eq. (A.9), $\underline{\Sigma}$ is the self energy matrix in Keldysh space, with the same structure as the Green's function given in Eq. (A.8):

$$\underline{\Sigma} = \begin{bmatrix} \Sigma^R & \Sigma^K \\ 0 & \Sigma^A \end{bmatrix}, \tag{A.11}$$

where $\Sigma^{R(A)}$ is the usual retarded (advanced) self energy from the equilibrium theory, whereas Σ^K is the Keldysh component of the self energy, characterizing the noneqilibrium aspect of the problem. The term $\underline{G}_0^{-1}(1,1')$ in Eq. (A.9) is given by:

$$\underline{G}_0^{-1}(1,1') = \left[i\partial_{t_1} - \epsilon(1)\right]\delta(1-1'). \tag{A.12}$$

The term $\epsilon(1)$ is the single-particle Hamiltonian, describing the dynamics of the system under consideration. For the nonequilibrium theory, there is also the conjugate or left-hand Dyson equation, which reads

$$\underline{G} \otimes \left(\underline{G}_0^{-1}(1,1') - \underline{\Sigma}\right) = \delta(1-1'). \tag{A.13}$$

A.1.2 Quantum Kinetic Equation

The equation of motion for the off-diagonal component of $\underline{G}$, namely the Keldysh Green's function G^K, is also known as the kinetic equation. This equation of motion for the Keldysh space Green's function can be obtained by subtracting the right hand Dyson equation (Eq. (A.9)) from its conjugate (Eq. (A.13)), which reads

$$\left[\underline{G}_0^{-1} - \underline{\Sigma} \overset{\otimes}{,} \underline{G}\right]_- = 0. \tag{A.14}$$

In principle, the Dyson equations specify the complete description of the system. The diagonal elements of $\underline{G}$ provide the available states, whereas the off-diagonal element, G^K, determines the occupation of the aforementioned states. Therefore, the kinetic equation is obtained by taking the Keldysh component of the equation of motion given in Eq. (A.14) into account, which is given as

$$\left[G_0^{-1} - \mathrm{Re}\Sigma \overset{\otimes}{,} G^K\right]_- - \left[\Sigma^K \overset{\otimes}{,} \mathrm{Re}G\right]_- = \frac{i}{2}\left[\Sigma^K \overset{\otimes}{,} A\right]_+ - \frac{i}{2}\left[\Gamma \overset{\otimes}{,} G^K\right]_+ . \tag{A.15}$$

We note that we introduce the spectral weight function $A = i\left(G^R - G^A\right)$, similar to the equilibrium theory, and also the following abbreviations, which shorten the equations:

$$\Gamma = i\left(\Sigma^R - \Sigma^A\right), \tag{A.16}$$

$$\mathrm{Re}\Sigma = \frac{1}{2}\left(\Sigma^R + \Sigma^A\right), \tag{A.17}$$

$$\mathrm{Re}G = \frac{1}{2}\left(G^R + G^A\right). \tag{A.18}$$

The kinetic equation given in Eq. (A.15) is the central equation describing the nonequilibrium dynamics of a system. However, in order to proceed, one usually needs to rely on further approximations,such as the gradient approximation.

We now introduce the gradient approximation, where we make use of the Wigner representation by switching to center-of-mass coordinates, given by $\boldsymbol{R} \equiv \frac{1}{2}\left(\boldsymbol{x}_1 + \boldsymbol{x}_{1'}\right)$ and $t \equiv \frac{1}{2}\left(t_1 + t_{1'}\right)$, and relative coordinates, $\boldsymbol{r} \equiv \left(\boldsymbol{x}_1 - \boldsymbol{x}_{1'}\right)$ and $\eta \equiv \left(t_1 - t_{1'}\right)$. In order to proceed, we Fourier transform the Keldysh space Green's function $\underline{G}$ with respect to $\boldsymbol{r}$

and t:

$$\underline{G}(X,p) = \int dx e^{-ipx} \underline{G}(X+x/2, X-x/2), \tag{A.19}$$

where we use the abbreviated 4-vector form $X \equiv (t, \boldsymbol{R})$, $x \equiv (\eta, \boldsymbol{r})$ and $p \equiv (E, \boldsymbol{p})$. In this notation, the inner product is defined as $px \equiv -E\eta + \boldsymbol{p}\cdot\boldsymbol{r}$.

In the gradient approximation scheme, the convolution $A \otimes B$ given in Eq. (A.10) can be expanded in a Taylor series when both A and B are slowly varying with respect to their coordinates, which reads

$$(A \otimes B)(X,p) = e^{i\left(\partial_X^A \partial_p^B - \partial_p^A \partial_X^B\right)/2} A(X,p) B(X,p). \tag{A.20}$$

It is then a straightforward task to evaluate the following identities within the gradient expansion:

$$[A \overset{\otimes}{,} B]_+ = 2AB, \tag{A.21}$$

$$\begin{aligned}[A \overset{\otimes}{,} B]_- &= i\left(\partial_E^A \partial_t^B - \partial_t^A \partial_E^B - \partial_{\boldsymbol{p}}^A \cdot \partial_{\boldsymbol{R}}^B + \partial_{\boldsymbol{R}}^A \cdot \partial_{\boldsymbol{p}}^B\right) AB, \\ &\equiv [A,B]_p,\end{aligned} \tag{A.22}$$

where in the last line, we define the generalized Poisson bracket. We now exemplify the kinetic equation for the case of a free electron model and demonstrate that the Boltzmann transport equation can be obtained for the nonmagnetic scattering problem. In this case, we find the inverse Green's function matrix using the Wigner representation as:

$$\underline{G}_0^{-1} = E - \xi_{\boldsymbol{p}} - U(\boldsymbol{R}, t), \tag{A.23}$$

where $\xi_{\boldsymbol{p}} = \boldsymbol{p}^2/2m - \mu$, and $U(\boldsymbol{R}, t)$ is the external potential. The self energy associated with the nonmagnetic scattering problem can be found within the self-consistent Born approximation, which reads

$$\underline{\Sigma}(E, \boldsymbol{p}, \boldsymbol{R}, t) = n_{\text{imp}} \int \frac{d\boldsymbol{p}'}{(2\pi)^3} |\mathcal{V}(\boldsymbol{p} - \boldsymbol{p}')|^2 \underline{G}(E, \boldsymbol{p}, \boldsymbol{R}, t), \tag{A.24}$$

where n_{imp} is the impurity density and $\mathcal{V}(\boldsymbol{p})$ is the Fourier transform of the nonmagnetic disorder potential. We next evaluate the left hand side of Eq. (A.15) within the gradient approximation. We assume the impurity concentration is low and the external perturbations specified by $U(\boldsymbol{R}, t)$ are slowly varying and hence approximate the self energy to be constant in time. Therefore, we obtain

$$[G_0^{-1}, G^K]_p = \Sigma^K A - \Gamma G^K. \tag{A.25}$$

The spectral function A can be obtained from the diagonal part of the Dyson equations given in Eq. (A.14). The spectral function in the low impurity concentration limit is obtained as

$$A = 2\pi\delta(E - \xi_{\boldsymbol{p}} - U). \tag{A.26}$$

The presence of the delta function due to the spectral weight on the right hand side of

Eq. (A.25) allows us to simplify the equation by integrating over the energy. It is customary to define the distribution function:

$$h_{\boldsymbol{p}} \equiv -\int \frac{dE}{2\pi i} G^K, \tag{A.27}$$

where $h_{\boldsymbol{p}} \equiv 1 - 2f_{\boldsymbol{p}}$ is related to the Fermi-Dirac distribution function in equilibrium. Using this, we obtain the Boltzmann equation for the nonmagnetic impurity problem:

$$\left(\partial_t + \nabla_{\boldsymbol{p}}\xi_{\boldsymbol{p}} \cdot \nabla_{\boldsymbol{R}} - \nabla_{\boldsymbol{R}} U \cdot \nabla_{\boldsymbol{p}}\right) f = -2\pi n_{\text{imp}} \int \frac{d\boldsymbol{p}'}{(2\pi)^3} |\mathcal{V}(\boldsymbol{p} - \boldsymbol{p}')|^2 \delta\left(\xi_{\boldsymbol{p}} - \xi_{\boldsymbol{p}'}\right)\left(f_{\boldsymbol{p}} - f_{\boldsymbol{p}'}\right). \tag{A.28}$$

It is no coincidence that we obtain the classical Boltzmann transport equation given in Eq. (A.28) given the fact that our starting point is based on quantum mechanical Green's function. The approximations made in this section relieved the quantum mechanical nature of the problem. In the next section, we discuss the semiclassical transport theory, which can be derived from the nonequilibrium Green's function formalism.

A.2 Semiclassical Transport Theory

In this section, we provide the reader a review of semiclassical transport theory of electrons in mesoscopic structures [184]. A microscopic formulation and solution of transport equations rely on approximations. One such approximation is the semiclassical theory, which is valid when the size of the system is much longer than the Fermi wavelength λ_F. In semiclassical transport theory, it is possible to define a local equilibrium, described by local temperature $T(\mathbf{r}, t)$ and local chemical potential $\mu(\mathbf{r}, t)$ that can vary in space and time. However, it is preferable to take an approach on the scattering problem by focusing on the distribution function of the electrons and its time evolution first, and calculate the physical quantities such as charge, heat and spin currents afterwards.

A.2.1 Distribution Function

Semiclassical transport theory allows us to treat electrons as "wavepackets" of Bloch states that propagates in the system. The physical interpretation of the distribution function of electrons $f(\mathbf{r}, \mathbf{k}, t)$ is that the average number of electrons at time t within the coarse-grained differential volume element $d\mathbf{r}d\mathbf{k}$ of the six-dimensional phase space:

$$f_\sigma(\mathbf{r}, \mathbf{k}, t)\frac{d\mathbf{r}d\mathbf{k}}{(2\pi)^3} \equiv \text{\# of electrons with spin } \sigma \text{ with position } \mathbf{r} \text{ and momentum } \mathbf{k} \text{ within phase space volume } d\mathbf{r}d\mathbf{k} \text{ at time t.} \tag{A.29}$$

The volume element $d\mathbf{r}d\mathbf{k}$ is related to the size of the wavepacket of electrons, usually given by the Fermi wavelength λ_F. The definition of electron distribution function given in Eq. (A.29) can be generalized to include other degrees of freedom other than the spin,

such as the band index. Here, we focus on the spin degree of freedom only.

We now consider the time evolution of the distribution function, in the absence of scattering processes. The distribution function satisfies the continuity equation in the phase space:

$$\frac{\partial f_\sigma}{\partial t} + \dot{\mathbf{r}} \cdot \nabla_{\mathbf{r}} f_\sigma + \dot{\mathbf{k}} \cdot \nabla_{\mathbf{k}} f_\sigma = 0, \tag{A.30}$$

where the velocity $\dot{\mathbf{r}}$ and the rate of change of momentum $\dot{\mathbf{k}}$ is described by the semiclassical equations of motion:

$$\begin{aligned} \dot{\mathbf{r}} &= \frac{1}{\hbar}\frac{\partial \epsilon(\mathbf{k})}{\partial \mathbf{k}}, \\ \dot{\mathbf{k}} &= -\frac{e}{\hbar}\mathbf{E}(\mathbf{r},t) - \frac{e}{\hbar c}\dot{\mathbf{r}} \times \mathbf{B}(\mathbf{r},t). \end{aligned} \tag{A.31}$$

Here, $\epsilon(\mathbf{k})$ is the dispersion relation, $\mathbf{E}(\mathbf{r},t)$ and $\mathbf{B}(\mathbf{r},t)$ are external electric and magnetic fields, respectively.

Eq. (A.30) is a result of particle number conservation for a given spin σ. However, the scattering processes within the system alter this picture and the semiclassical dynamics is not enough to describe the effects of scattering, which is usually of quantum mechanical nature. Therefore, we include what is known as the collision integral to the continuity equation given by Eq. (A.30) and obtain the Boltzmann transport equation.

A.2.2 Boltzmann Transport Equation

The Boltzmann transport equation describes the time evolution of the distribution function while incorporating different scattering mechanisms. This approach allows us to evaluate the charge and heat current responses of the system in the presence of an applied bias. Furthermore, the Boltzmann transport equation successfully describes thermoelectric effects such as Seebeck and Peltier effects and also it can generalized to include spin-dependent transport. We start with the Boltzmann transport equation:

$$\frac{\partial f_\sigma}{\partial t} + \dot{\mathbf{r}} \cdot \nabla_{\mathbf{r}} f_\sigma + \dot{\mathbf{k}} \cdot \nabla_{\mathbf{k}} f_\sigma = \left(\frac{\partial f_\sigma}{\partial t}\right)_{\text{coll}}, \tag{A.32}$$

where the second term on the left hand side is related to the diffusion process and the third term on the left hand side is related to the drift of the electrons in response to external fields. The term of the right hand side is the collision integral that depends on the microscopic details of the scattering processes within the system. The collision integral is a functional of the distribution function and it is usually denoted as $\mathcal{I}_{\mathbf{k}}\{f_\sigma\}$. The general form of the collision integral due to elastic scattering from impurities is given as

$$\mathcal{I}_{\mathbf{k}}\{f_\sigma\} = \sum_{\mathbf{k}',\sigma} \Gamma_{\sigma'\sigma}(\mathbf{k}',\mathbf{k}) f_{\sigma'}(\mathbf{k}') \left(1 - f_\sigma(\mathbf{k})\right) - \Gamma_{\sigma\sigma'}(\mathbf{k},\mathbf{k}') f_\sigma(\mathbf{k}) \left(1 - f_{\sigma'}(\mathbf{k}')\right), \tag{A.33}$$

where the scattering rate $\Gamma_{\sigma\sigma'}(\mathbf{k}, \mathbf{k}')$ describes the transition from an initial state with spin σ and momentum $\mathbf{k}$ to a final state with spin σ' and momentum $\mathbf{k}'$. In general, different scattering mechanisms do not interfere with one another, hence the scattering rates may represent more than one source of scattering. The form of the collision integral is a result of the Pauli exclusion principle; factors f and $(1 - f)$ represent occupied incoming states and empty outgoing states, respectively.

The conventional method to obtain the scattering rates is based on the Fermi's golden rule, that is derived from the second-order perturbation theory:

$$\Gamma_{\sigma\sigma'}(\mathbf{k}, \mathbf{k}') = \frac{2\pi}{\hbar} |\langle \mathbf{k}, \sigma | \mathcal{V}_{\sigma\sigma'} | \mathbf{k}', \sigma' \rangle|^2 \delta\left(\epsilon_{\mathbf{k},\sigma} - \epsilon_{\mathbf{k}',\sigma'}\right), \tag{A.34}$$

where $\mathcal{V}$ is the perturbation potential, representing the source of scattering. The states $|\mathbf{k}, \sigma\rangle$ are solutions of the Schrödinger equation for the unperturbed Hamiltonian. We restrict the discussion to include static perturbations only, hence $\mathcal{V}$ is time independent.

In general, it is difficult to solve the Boltzmann transport equation given by Eq. (A.32) even if the scattering rates given by Eq. (A.34) are obtained, because it is a nonlinear integro-differential equation. Therefore, either numerical methods or analytical approximation schemes are applied to solve the Boltzmann transport equation.

A.2.3 Relaxation Time Approximation

The relaxation time approximation relies on the assumption that the collision rate does not depend on the electron distribution function. We then seek for a solution of the distribution function of the form $f = f_0 + \delta f$, where f_0 is an equilibrium distribution function given by Fermi-Dirac distribution function, and δf is the small deviation from the equilibrium distribution. In this case, we expand the collision integral as

$$\mathcal{I}_{\mathbf{k}}\{f_0 + \delta f\} \approx \left(\frac{\partial \mathcal{I}_{\mathbf{k}}}{\partial f}\right)\Big|_{f=f_0} \delta f \equiv -\frac{\delta_f}{\tau_{\mathbf{k}}}, \tag{A.35}$$

where the functional derivative $(\partial \mathcal{I}_{\mathbf{k}}/\partial f)^{-1}$ is the relaxation time $\tau_{\mathbf{k}}$ which quantifies the strength of the source of scattering in the system. Generally, the relaxation time is momentum and energy dependent.

Usually, the relaxation time τ for a given scattering mechanism yields a length scale ℓ, which is known as the relaxation length. Different types of scattering mechanisms result in different relaxation lengths, which is a measure of average distance a particle travels between successive scatterings. Most common scattering mechanisms in mesoscopic systems are (i) elastic scattering from impurities and dislocations that result in a relaxation length known as the elastic mean free path ℓ_{el}, (ii) the spin-flip scattering due to magnetic impurities and nuclear spins which yields the spin-flip length ℓ_{sf}, (iii) electron-electron and electron-phonon scattering with $\ell_{\mathrm{e-e}}$ and $\ell_{\mathrm{e-ph}}$, correspondingly and finally (iv) electron-photon interaction with $\ell_{\mathrm{e}-\gamma}$. The first two scattering mechanisms are elastic, while the remaining ones are inelastic, establishing a local equilibrium via energy-relaxation. In this thesis, we consider elastic scattering only, which is a good approxima-

tion for mesoscopic systems with size $L < \ell_{\mathrm{e-e}}, \ell_{\mathrm{e-ph}}, \ell_{\mathrm{e}-\gamma}$.The regimes of transport we are interested in are ballistic ($L \ll l_{\mathrm{el}}$), quasi-ballistic ($L \sim l_{\mathrm{el}}$) and diffusive ($L > l_{\mathrm{el}}$) regimes.

In the following, we exemplify the relaxation time approximation by considering the one of the most dominant source of scattering within mesoscopic systems, namely the random nonmagnetic impurity scattering. The impurity potential is described by the potential of localized scatterers $\mathcal{V}(\mathbf{r}) = U \sum_i^{N_{\mathrm{imp}}} \delta(\mathbf{r} - \mathbf{R}_i)$ where $\mathbf{R}_i$ denotes the position of the i^{th} scatterer, U is the strength of the scattering and N_{imp} is the total number of scatterers within the system. We then evaluate the scattering rates by insert this impurity potential into Eq. (A.34). We first obtain the matrix element in Eq. (A.34) as

$$|\langle \mathbf{k}| \mathcal{V} |\mathbf{k}'\rangle|^2 = \frac{U^2}{\Omega^2} \left| \sum_i^{N_{\mathrm{imp}}} e^{i(\mathbf{k}-\mathbf{k}')\cdot\mathbf{R}_i} \right|^2 , \tag{A.36}$$

where Ω is the volume of the system. Since we assume a random impurity configuration, we can average over possible impurity configurations and we obtain the configuration averaged matrix element as $\overline{|\langle \mathbf{k}| \mathcal{V} |\mathbf{k}'\rangle|^2} = U^2 \frac{N_{\mathrm{imp}}}{\Omega^2}$. It is then straightforward to obtain the scattering rates by inserting this into Eq. (A.34). Having obtained the scattering rates, we now write the collision integral for electrons at the Fermi surface

$$\mathcal{I} = \frac{2\pi}{\hbar} U^2 \frac{N_{\mathrm{imp}}}{\Omega^2} \sum_{\mathbf{k}'} \delta(\epsilon_{k_F} - \epsilon_{\mathbf{k}'}) \left(f(\mathbf{k}') - f(k_F)\right), \tag{A.37}$$

$$= \frac{2\pi}{\hbar} U^2 n_{\mathrm{imp}} \int \frac{d\mathbf{k}'}{(2\pi)^3} \delta(\epsilon_{k_F} - \epsilon_{\mathbf{k}'}) \left(f(\mathbf{k}') - f(k_F)\right), \tag{A.38}$$

$$\approx -\frac{2\pi}{\hbar} U^2 n_{\mathrm{imp}} \nu(E_F) \delta f, \tag{A.39}$$

where we identify the term $2\pi n_{\mathrm{imp}} U^2 \nu(E_F)/\hbar = \tau^{-1}$ as the inverse relaxation time. Here, n_{imp} is the volume density of scatterers and $\nu(E_F)$ is the density of states at the Fermi level E_F. We also note that the deviation δf from the equilibrium distribution function is due to the angle-dependent contribution from the scatterers, even though the equilibrium Fermi surface is assumed to spherical. Consequently, one can solve for the nonequilibrium part of the distribution function using Eq. (A.32) and derive the transport characteristics of the system under consideration.

A.3 Heat and Charge Transport

In this section, we review the basics of the various current responses of the mesoscopic systems in the presence of applied biases. The main approach we use while determining the current responses is to solve the Boltzmann transport equation given by Eq. (A.32) in order to obtain the nonequilibrium distribution function. In the remaining part of this section, we assume that we have the nonequilibrium distribution functions and we proceed with the calculations of the currents.

A.3.1 Charge and Heat Currents

We start with the semiclassical description for the charge current density $\mathbf{j}_e$, which is simply the flux of charge carriers in response to thermodynamic forces such as temperature gradient ∇T or chemical potential gradient $\nabla \mu$.

$$\mathbf{j}_e(\mathbf{r},t) = -\frac{e}{\Omega}\sum_{\mathbf{k},\sigma}\mathbf{v}_\sigma(\mathbf{k})f_\sigma(\mathbf{r},\mathbf{k},t), \tag{A.40}$$

$$= -e\sum_{\sigma}\int\frac{d\mathbf{k}}{(2\pi)^3}\mathbf{v}_\sigma(\mathbf{k})f_\sigma(\mathbf{r},\mathbf{k},t), \tag{A.41}$$

where $\mathbf{v}_\sigma(\mathbf{k}) = \hbar^{-1}\partial\epsilon_{\mathbf{k}\sigma}/\partial\mathbf{k}$ is the velocity of the carriers with spin σ and e is the elementary unit charge. We note that we highlight the contribution to the charge current from each spin species σ.

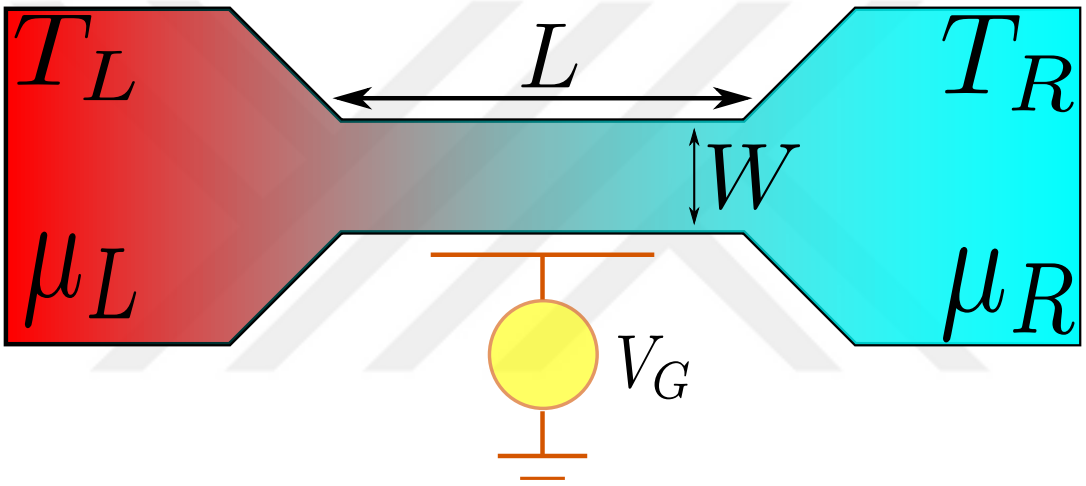

Figure A.3: A standard three terminal transport setup. A quasi 1D wire is connected to two reservoirs with different chemical potentials and/or temperatures. The third terminal, known as the gate terminal, is used to change the electron density within the wire, hence effect the transport properties.

As noted in the previous section, depending on the length of the system compared to the relaxation length scales, the transport regime changes. Nevertheless, Eq. (A.40) provides a general description for the charge current regardless of the scattering mechanism and transport regime. In a typical transport experiment, the system under consideration, say a quasi-one-dimensional wire shown in Fig. A.3, is connected to two reservoirs. These reservoirs are assumed to be large enough such that they can be described with $\mu_{L/R}$ and $T_{L/R}$, which serve as boundary conditions that are necessary to solve the Boltzmann transport equation.

As particles are transported between two reservoirs with different temperatures and/or chemical potentials, both charge and heat can be transported. In order to obtain the resultant heat current $\mathbf{j}_q$, we use the first law of thermodynamics for a system with fixed volume, $dQ = dU - \mu dN$, where dQ is the change in heat energy, dU is the change in internal energy and dN is the change in number of particles. Subsequently, we have the

following relations for the currents in the system:

$$\mathbf{j}_q = j_u - \frac{\mu}{e} j_e, \tag{A.42}$$

where j_u is the energy current, *i.e.* the flux of total energy. We then use Eq. (A.40) and obtain the heat current as

$$\mathbf{j}_q(\mathbf{r}, t) = \sum_\sigma \int \frac{d\mathbf{k}}{(2\pi)^3} (\epsilon - \mu) \mathbf{v}_\sigma(\mathbf{k}) f_\sigma(\mathbf{r}, \mathbf{k}, t). \tag{A.43}$$

In general, the sign of the currents determine whether the system in question can be used as an engine or a refrigerator.

Appendix B

PROJECTING THE HYPERFINE HAMILTONIAN TO THE EDGES

We first define the Fermi contact hyperfine interaction in 3D [63]:

$$\begin{aligned} H_{hf}(\boldsymbol{r}) &= \frac{\mu_0}{4\pi}\frac{8\pi}{3}\gamma_e\gamma_N\hbar^2\sum_n \boldsymbol{\sigma}\cdot\boldsymbol{I}_n\delta(\boldsymbol{r}-\boldsymbol{R}_n) \\ &= \frac{8}{3}\frac{\mu_0\mu_B\gamma_N\hbar}{v_0}v_0\sum_n \boldsymbol{\sigma}\cdot\boldsymbol{I}_n\delta(\boldsymbol{r}-\boldsymbol{R}_n), \end{aligned} \tag{B.1}$$

where $\boldsymbol{\sigma}$ is the vector of Pauli spin matrices in electron spin space, $\boldsymbol{I}_n$ is the vector of Pauli spin matrices for the n^{th} nuclear spin and correspondingly, $\boldsymbol{R}_n$ is its position. In the second line above, we use $\gamma_e = \frac{2\mu_B}{\hbar}$, where μ_B is the Bohr magneton. We further divide and multiple the right hand side with v_0 which is the unit cell volume. For clarity, we define $\alpha = \frac{8}{3}\frac{\mu_0\mu_B\gamma_N\hbar}{v_0}$.

We proceed with writing down the generic electron wavefunction:

$$\psi_{k\sigma}(\boldsymbol{r}) = \frac{1}{\sqrt{L_x}}e^{ikx}f_k(y,z)u_k(\boldsymbol{r})\left|\sigma\right\rangle, \tag{B.2}$$

where L_x is the length along the x direction which we choose to be the direction of propagation of the edge states and u_k is the Bloch's function (periodic in real space) with normalization $\int d^3r|u_k(\boldsymbol{r})|^2 = v_0$. $f_k(y,z)$ is the envelope of the electron wavefunction with normalization $\int dydz|f_k(y,z)|^2 = 1$.

We decompose $u(\boldsymbol{r})$ into x, y, z components and write as $u_x(x)u_y(y)u_z(z)$. Secondly, we integrate out the y and z of H_{hf} and obtain:

$$
\begin{aligned}
H_{hf}(x) &= \int dydz|u_y(y)|^2|u_z(z)|^2|f_k(y,z)|^2\alpha v_0 \sum_n \boldsymbol{\sigma}\cdot\boldsymbol{I}_n\delta(\boldsymbol{r}-\boldsymbol{R}_n) \\
&= \alpha v_0 \sum_n |u_y(y_n)|^2|u_z(z_n)|^2|f_k(y_n,z_n)|^2\boldsymbol{\sigma}\cdot\boldsymbol{I}_n\delta(x-x_n) \\
&= \tilde{\alpha} v_0 \sum_n |f_k(y_n,z_n)|^2\boldsymbol{\sigma}\cdot\boldsymbol{I}_n\delta(x-x_n),
\end{aligned}
\tag{B.3}
$$

where in the last line, we used the fact that $u_y(y_n) = u_y(0)$ and $u_z(z_n) = u_z(0)$ are due to periodicity and we define $\tilde{\alpha} \equiv \alpha|u_y(0)|^2|u_z(0)|^2$. We further approximate that the term $|f_k(y_n,z_n)|^2 \sim \frac{1}{L_yL_z}$, where L_y and L_z are the transverse lengths of the electron wave function occupies. We finally obtain the effective 1D hyperfine interaction Hamiltonian as:

$$
H_{hf}(x) = \tilde{\alpha}\frac{v_0}{L_yL_z}\sum_n \boldsymbol{\sigma}\cdot\boldsymbol{I}_n\delta(x-x_n). \tag{B.4}
$$

Here, we define $\lambda \equiv \tilde{\alpha}\frac{v_0}{L_yL_z}$. We note that $\tilde{\alpha}$ is almost A_{hf} but the factor $|u_x(0)|^2$ is missing (in other words $A_{hf} = \tilde{\alpha}|u_x(0)|^2 = \frac{8}{3}\frac{\mu_0\mu_B\gamma_N\hbar}{v_0}|u(0)|^2$ [185]. The reason for that is, the x components is not integrated out yet. Then, we write finally:

$$
H_{hf}(x) = \lambda\sum_n \boldsymbol{\sigma}\cdot\boldsymbol{I}_n\delta(x-x_n), \tag{B.5}
$$

where S is number of unit cells in the cross-section (on y-z plane) in units of a_0^2 and we define $\lambda \equiv A_{hf}\frac{a_0}{S}$.

Appendix C

MEAN POLARIZATION DYNAMICS AND ELECTRIC CURRENT

In this appendix, we focus on the time dependence of the nuclear mean polarization and later obtain electric current in the short edge limit. We first define the mean polarization at position x per edge,

$$m(x) \equiv \frac{N_\uparrow(x) - N_\downarrow(x)}{2N(x)},$$

where $N(x) = N_\uparrow(x) + N_\downarrow(x)$ is the number of nuclei at position x and $x + \Delta x$ per edge participating in the spin-flip interactions. With this definition fully polarized nuclear spins have $m = \pm 1/2$.

The dynamics of the mean polarization, given in Eq. (3.10) and repeated below, is obtained from Eq. (F.2) and (3.9):

$$\frac{dm(x)}{dt} = \gamma_0 \Gamma_B(x) - m(x)\gamma_0 \Gamma_T(x). \tag{3.10}$$

As mentioned in the main text, $\Gamma_B(x)$ and $\Gamma_T(x)$ is given as:

$$\begin{aligned} \Gamma_B(x) &= \int \frac{d\epsilon}{\hbar} \frac{f_+ - f_-}{2} \\ \Gamma_T(x) &= \int \frac{d\epsilon}{\hbar} \big(f_+ + f_- - 2f_+ f_-\big), \end{aligned} \tag{C.1}$$

where we suppressed the energy and position dependence of the distribution functions $f_\pm(\epsilon, x)$. Note that current conservation requires $\Gamma_B(x)$ to be x-independent.

For short edges we have $\Gamma[f_+, f_-]\, L \ll 1$, and $N_{\uparrow(\downarrow)}(x)$ and $m(x)$ have only a weak dependence on x. Performing a gradient expansion, we first approximate $N_{\uparrow(\downarrow)}(x)$ and $m(x)$ with their leading, x-independent, terms. We next approximate the distributions $f_\pm$ with the Fermi distributions of the reservoirs $f^0_{L(R)}$ from which they originate. We now evaluate the integrals in Eq. (C.1) and obtain

$$\Gamma_B = (\mu_L - \mu_R)/2\hbar,$$

$$\Gamma_T = \frac{(\mu_L - \mu_R)}{\hbar} \coth\left(\frac{\mu_L - \mu_R}{2kT}\right), \tag{C.2}$$

in agreement with Eq. (3.11). We note that in this approximation, Γ_B is proportional to the applied bias $\mu_L - \mu_R$, hence it vanishes for zero applied voltage. We also note that $\Gamma_T \geq 0$.

We now focus on the total current. In the short edge limit, the distribution functions of the right and left movers within the edge in question are given by Eq. (3.15). We then obtain the total current as

$$\begin{aligned} I_{tot} &= \frac{e}{h}\int d\epsilon \big(f_+ - f_-\big) \\ &= \frac{e}{h}\int d\epsilon \Big[\big(f_L^0 - f_R^0\big) - h\big(\Gamma_{-+}(\epsilon) - \Gamma_{+-}(\epsilon)\big)\Big] \\ &= \frac{e^2}{h}V - eN\frac{dm}{dt}, \end{aligned}$$

consistent with Eq. (3.16). Here, f_+ [f_-] are the (in general x-dependent) distribution functions of the right [left] movers in the given edge, and f_L^0 [f_R^0] are the (Fermi) distributions of the lead from which the right [left] movers originate. In the last line, we used Eq. (3.9) in the short edge limit. We identify the first term on the right hand side as the current due to the usual voltage bias (I_{bias}) and the second term as the induced current due to Maxwell's demon effect (I_{MD}).

In order to see the mean polarization dependence of the total current in the short edge limit, we substitute the explicit forms of Γ_B and Γ_T given in Eq. (3.11) into Eq. (3.16) to obtain:

$$I_{\text{tot}}(t) = \frac{e^2}{h}V\left[\left(1 - \frac{\zeta}{2}\right) + m(t)\,\zeta\,\coth\left(\frac{eV}{2kT}\right)\right], \tag{C.3}$$

where we defined a dimensionless quantity $\zeta = 2\pi N\gamma_0$, which is a rough measure of the interaction strength over the whole wire per edge. We see that in the limit of vanishing voltage bias, total current is not zero if $m(t)$ is nonzero. This behavior persists even if the temperature or the chemical potential of both of the reservoirs are equal, demonstrating the pure entropy-driven current.

Appendix D

WORK EXTRACTION AND HEAT DISSIPATION OF THE QUANTUM INFORMATION ENGINE

We calculate the power absorbed/generated by quantum information engine under fixed applied voltage bias as follows:

$$\begin{aligned} P(t) &= I_{\text{tot}}(t)\, V \\ &= \frac{eV}{h}\Big[eV(1-\frac{\zeta}{2}) + \zeta\, m(t)\, \hbar\Gamma_T\Big] \\ &= \frac{eV}{h}\Big[eV + \zeta(m_0-\bar{m})\mathrm{e}^{-t/\tau_m}\hbar\Gamma_T\Big], \end{aligned} \tag{D.1}$$

where in the last line we used Eq. (3.12) and $\bar{m}\hbar\Gamma_T = \frac{eV}{2}$.

Charging cycle. We would like to find the amount of heat dissipated while we charge the device. Starting from totally unpolarized nuclear spins ($m_0 = 0$) and using Eq. (3.12) and Eq. (D.1), we get:

$$\begin{aligned} P(t) &= \frac{eV_C}{h}\Big[eV_C - \zeta\bar{m}\mathrm{e}^{-t/\tau_m}\hbar\Gamma_T\Big], \\ &= \frac{eV_C}{h}\Big[eV_C - eV_C\frac{\zeta}{2}\mathrm{e}^{-t/\tau_m}\Big]. \end{aligned} \tag{D.2}$$

As shown in Eq. (3.12), the amount of time to reach the target mean polarization is infinitely long. Instead, we charge the device up to a fraction of full polarization $m = \frac{\kappa}{2}$ where κ is a value we later choose depending on the application and whether we intend to maximize power or efficiency. Using $\frac{\kappa}{2} = \bar{m}(1-e^{-\bar{t}/\tau_m})$, we obtain the following for the amount of time $\bar{t}$ to reach the specified target mean polarization:

$$\bar{t} = -\tau_m \ln\Big(1 - \frac{\kappa}{2\bar{m}}\Big). \tag{D.3}$$

We then get the dissipated heat by integrating the power up to $\bar{t}$:

$$\begin{aligned} W_C(V_C) &= \int_0^{\bar{t}} \frac{eV_C}{h}\Big[eV_C - \frac{\zeta}{2}\mathrm{e}^{-t/\tau_m}eV\Big] \\ &= \frac{e^2V_C^2}{h}\tau_m\Big[-\ln\Big(1-\frac{\kappa}{2\bar{m}}\Big) - \frac{\zeta}{2}\frac{\kappa}{2\bar{m}}\Big] \\ &= \frac{eV_C}{2\pi\gamma_0}\tanh\left(\frac{eV_C}{2k_BT}\right) \\ &\qquad \times \Big[\ln\left(\frac{2\bar{m}}{2\bar{m}-\kappa}\right) - \frac{\zeta}{2}\frac{\kappa}{2\bar{m}}\Big]. \end{aligned} \tag{D.4}$$

Note that $0 \leq 1 - \kappa/2\bar{m} < 1$. This condition gives us an lower bound on the applied voltage:

$$V_C \geq \frac{k_BT}{e}\ln\left(\frac{1+\kappa}{1-\kappa}\right). \tag{D.5}$$

Discharging cycle. For the next step in the engine cycle, we apply a reverse (discharging) bias, $V_D < 0$, and we would like to find the time t^* at which $P(t)$ changes sign. Using Eq. (D.1), we obtain:

$$t^* = \tau_m \ln\left[\zeta\left(\frac{1}{2} + m_0\coth\left(\frac{|eV_D|}{2k_BT}\right)\right)\right] \tag{D.6}$$

We then integrate the power up to $t = t^*$ to obtain the work done at fixed voltage:

$$\begin{aligned} W_D(V_D) &= \int_0^{t^*} \frac{|eV_D|}{h}\Big[|eV_D| - \zeta(m_0-\bar{m})\mathrm{e}^{-t/\tau_m}\hbar\Gamma_T\Big] \\ &= \frac{e^2V_D^2}{h}t^* \\ &\qquad + \frac{|eV_D|}{h}\tau_m\zeta(m_0-\bar{m})\hbar\Gamma_T(\mathrm{e}^{-t^*/\tau_m}-1). \end{aligned} \tag{D.7}$$

Inserting t^* into the equation above and and using the relation $\bar{m}\hbar\Gamma_T = -\frac{|eV_D|}{2}$, we get:

$$\begin{aligned} W_D(V_D) = \frac{e^2V_D^2}{h}\tau_m\Bigg[&\ln\left(\frac{\zeta}{2} + m_0\,\zeta\,\coth\left(\frac{|eV_D|}{2k_BT}\right)\right) \\ &+ 1 - \left(\frac{\zeta}{2} + m_0\,\zeta\,\coth\left(\frac{|eV_D|}{2k_BT}\right)\right)\Bigg]. \end{aligned} \tag{D.8}$$

We finally take the polarization reached at the end of the charging cycle, $m_0 = \frac{\kappa}{2}$, as the initial polarization for the discharging cycle to finally obtain

$$\begin{aligned} W_D(V_D) = \frac{|eV_D|}{2\pi\gamma_0}&\tanh\left(\frac{|eV_D|}{2k_BT}\right) \\ &\times \Bigg[\ln\left(\frac{\zeta}{2} + \frac{\kappa\,\zeta}{2}\,\coth\left(\frac{|eV_D|}{2k_BT}\right)\right) \end{aligned}$$

$$+1-\left(\frac{\zeta}{2}+\frac{\kappa\,\zeta}{2}\,\coth\left(\frac{|eV_D|}{2k_BT}\right)\right)\Bigg]. \tag{D.9}$$

In order to extract work from the nuclear spin polarization, one has to make sure that $t^* > 0$, which gives us an upper bound on the applied voltage:

$$|V_D| \leq \frac{k_BT}{e}\ln\left(\frac{2-\zeta(1-\kappa)}{2-\zeta(1+\kappa)}\right). \tag{D.10}$$

Maximum Work Extraction: Eq. (D.10) suggests that, in the short edge limit, work extraction is only possible when the applied reverse bias is smaller than the thermal energy. We therefore consider the $2k_BT \gg |eV_D|$ case and approximate Eq. (D.9) as follows:

$$W_D(V_D) \approx \frac{|eV_D|^2}{4k_BT\pi\gamma_0}\Bigg[\ln\left(\frac{\zeta}{2}\Big(1+\kappa\frac{2k_BT}{|eV_D|}\Big)\right) + 1-\frac{\zeta}{2}\left(1+\kappa\frac{2k_BT}{|eV_D|}\right)\Bigg]. \tag{D.11}$$

The maximum work that can be extracted from quantum information engine can be obtained by maximizing Eq. (D.9) with respect to applied reverse bias V_D. We neglect the logarithmic term in Eq. (D.9) and we find the applied reverse bias that maximizes the amount of extracted work:

$$|eV_D^*| = \frac{k_BT\zeta\kappa}{(2-\zeta)}. \tag{D.12}$$

Plugging V_D^* into Eq. (D.11) and choosing maximum initial polarization $\kappa = 1$, we get the maximum work that can be extracted under constant voltage bias in the short edge limit as:

$$W_{tot} \simeq \frac{\pi}{4}k_BTN^2\gamma_0. \tag{D.13}$$

Appendix E

QUANTUM INFORMATION ENGINE UNDER AC VOLTAGE BIAS

In this appendix, we demonstrate the method we employed while solving for the AC voltage bias characteristics of the quantum information engine. Firstly, we expand the mean polarization as a Fourier series, $m(t) = \sum_{n=-\infty}^{\infty} m_n e^{in\Omega t}$. Furthermore, we use the expansion $|\sin(\Omega t)| = \frac{2}{\pi} - \frac{4}{\pi}\sum_{n=1}^{\infty} \frac{1}{4n^2-1}\cos(2n\Omega t)$ and obtain the following equation:

$$\sum_{n=-\infty}^{\infty} in\Omega m_n e^{in\Omega t} = \frac{\gamma_0}{\hbar} eV_0 \left(\frac{e^{i\Omega t} - e^{-i\Omega t}}{4i} + \frac{2}{\pi} \sum_{n'=-\infty}^{\infty} m_{n'} e^{in'\Omega t} \sum_{k=-\infty}^{\infty} \frac{1}{4k^2-1} e^{i2k\Omega t} \right), \tag{E.1}$$

where m_n is the n^{th} Fourier coefficient of the mean polarization. We collect the Fourier coefficients m_n on one side of the equation and introducing $\tilde{\alpha} = \gamma_0 eV_0/\hbar\Omega$ and we obtain:

$$inm_n - \frac{2\tilde{\alpha}}{\pi} \sum_{k=-\infty}^{\infty} \frac{m_{n-2k}}{4k^2-1} = \frac{\tilde{\alpha}}{4i} \left(\delta_{n,1} - \delta_{n,-1}\right). \tag{E.2}$$

The form of Eq. (E.2) suggests that only the odd harmonics are present in the mean polarization dynamics. Furthermore, we notice that we have a recursive equation that needs to be solved. We assume that the initial conditions do not effect the long term dynamics. Consequently, we solve this recursive equation for m_n by converting it into a matrix equation as follows:

$$\begin{bmatrix} \ddots & \ddots & \ddots & \ddots & \ddots & \ddots \\ \ddots & i3 - \frac{2\tilde{\alpha}}{\pi} & \frac{2\tilde{\alpha}}{3\pi} & \frac{2\tilde{\alpha}}{15\pi} & \frac{2\tilde{\alpha}}{35\pi} & \ddots \\ \ddots & \frac{2\tilde{\alpha}}{3\pi} & i - \frac{2\tilde{\alpha}}{\pi} & \frac{2\tilde{\alpha}}{3\pi} & \frac{2\tilde{\alpha}}{15\pi} & \ddots \\ \ddots & \frac{2\tilde{\alpha}}{15\pi} & \frac{2\tilde{\alpha}}{3\pi} & -i - \frac{2\tilde{\alpha}}{\pi} & \frac{2\tilde{\alpha}}{3\pi} & \ddots \\ \ddots & \frac{2\tilde{\alpha}}{35\pi} & \frac{2\tilde{\alpha}}{15\pi} & \frac{2\tilde{\alpha}}{3\pi} & -i3 - \frac{2\tilde{\alpha}}{\pi} & \ddots \\ \ddots & \ddots & \ddots & \ddots & \ddots & \ddots \end{bmatrix} \begin{pmatrix} \vdots \\ m_3 \\ m_1 \\ m_{-1} \\ m_{-3} \\ \vdots \end{pmatrix} = \frac{\tilde{\alpha}}{4i} \begin{pmatrix} \vdots \\ 0 \\ 1 \\ -1 \\ 0 \\ \vdots \end{pmatrix} \tag{E.3}$$

We solve for the vector of Fourier coefficients, which we denote as $\boldsymbol{m_n}$, by truncating and inverting this matrix numerically. We plot the contribution of the mean polarization and the Maxwell's demon induced current in Fig. E.1. Subsequently, we reconstruct the mean polarization and plot its dynamics in Fig. 3.9.

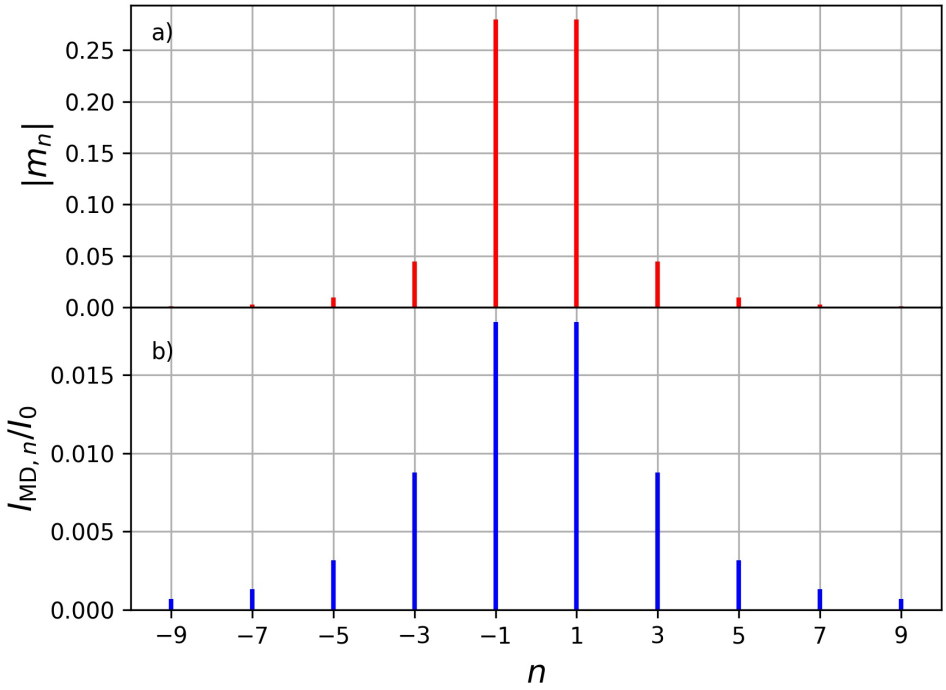

Figure E.1: The Fourier coefficients of a) the mean polarization m_n (given in absolute value) and b) the Maxwell's demon induced current $I_{\mathrm{MD},n}$ normalized to the ballistic current. The parameters used are $\gamma_0 = 10^{-9}$, $\zeta = 1$, $T = 0$ and $\Omega = 10\,\mathrm{Hz}$.

Appendix F

CAPACITIVE QUANTUM INFORMATION ENGINE CURRENT-VOLTAGE CHARACTERISTICS

In this appendix, we derive the Maxwell's demon induced current for the capacitive quantum information engine. We first write down Boltzmann transport equation for the bottom edge:

$$\partial_t f^{\text{bot}}_{\uparrow,\downarrow} = \pm(\Gamma^{\text{bot}}_{+-}(\epsilon,x) - \Gamma^{\text{bot}}_{-+}(\epsilon,x)\,)\,\nu(0)^{-1} \mp v_F \partial_x f^{B}_{\uparrow,\downarrow}, \tag{F.1}$$

where the superscript bot denotes the bottom edge. We obtain the collision terms for bottom edge as:

$$\begin{aligned}\Gamma^{\text{bot}}_{-+}(\epsilon,x) &= \frac{\gamma_0}{\hbar}\, N^{\text{bot}}_{\downarrow}(x)\, f^{\text{bot}}_{\uparrow}(\epsilon,x)(1 - f^{\text{bot}}_{\downarrow}(\epsilon,x)) \\ \Gamma^{\text{bot}}_{+-}(\epsilon,x) &= \frac{\gamma_0}{\hbar}\, N^{\text{bot}}_{\uparrow}(x)\, f^{\text{bot}}_{\downarrow}(\epsilon,x)(1 - f^{\text{bot}}_{\uparrow}(\epsilon,x)).\end{aligned} \tag{F.2}$$

We use separation of time scales by assuming that the nuclear spin polarization m is changing slowly and seeking a steady state solution. In that case, we find that the distribution functions obey:

$$\begin{aligned}\partial_x f^{\text{bot}}_{\uparrow,\downarrow} &= \left(\Gamma^{\text{bot}}_{+-}(\epsilon,x) - \Gamma^{\text{bot}}_{-+}(\epsilon,x)\right)\left(v_F\nu(0)\right)^{-1} \\ &\equiv \Gamma^{\text{bot}}[f^{\text{bot}}_{\uparrow}, f^{\text{bot}}_{\downarrow}].\end{aligned}$$

We expand in gradients of the distribution function and obtain a linear dependence in position as:

$$f^{\text{bot}}_{\uparrow,\downarrow}(x) = f^{0}_{L,R} + \Gamma^{\text{bot}}[f^{0}_{L}, f^{0}_{R}]\,(x \pm L/2). \tag{F.3}$$

where we use the boundary conditions $f^{\text{bot}}_{\uparrow}(x = -L/2) = f^{0}_{L}$ and $f^{\text{bot}}_{\downarrow}(x = L/2) = f^{0}_{R}$, where f^{0}_{L} and f^{0}_{R} are distributions of left and right reservoirs, respectively.

Similar to the bottom edge, we write down the Boltzmann transport equation for the top

edge:

$$\partial_t f^{\text{top}}_{\uparrow,\downarrow} = \mp(\Gamma^{\text{top}}_{+-}(\epsilon,x) - \Gamma^{\text{top}}_{-+}(\epsilon,x)\,)\,\nu(0)^{-1} \pm v_F \partial_x f^{\text{top}}_{\uparrow,\downarrow}, \tag{F.4}$$

where the superscript top denotes the top edge. Correspondingly, we obtain the collision terms for top edge as:

$$\begin{aligned}\Gamma^{\text{top}}_{-+}(\epsilon,x) &= \frac{\gamma_0}{\hbar}\, N^{\text{top}}_{\uparrow}(x)\, f^{\text{top}}_{\downarrow}(\epsilon,x)(1 - f^{\text{top}}_{\uparrow}(\epsilon,x)) \\ \Gamma^{\text{top}}_{+-}(\epsilon,x) &= \frac{\gamma_0}{\hbar}\, N^{\text{top}}_{\downarrow}(x)\, f^{\text{top}}_{\uparrow}(\epsilon,x)(1 - f^{\text{top}}_{\downarrow}(\epsilon,x)).\end{aligned} \tag{F.5}$$

In steady state, the distribution functions at the top edge obey:

$$\begin{aligned}\partial_x f^{\text{top}}_{\uparrow,\downarrow} &= \left(\Gamma^{\text{top}}_{+-}(\epsilon,x) - \Gamma^{top}_{-+}(\epsilon,x)\right)\left(v_F\nu(0)\right)^{-1} \\ &\equiv \Gamma^{top}[f^{\text{top}}_{\uparrow}, f^{\text{top}}_{\downarrow}].\end{aligned}$$

Before we make use of the same expansion to obtain the distribution functions, we now describe the property of capacitive quantum information engine. As only one spin species is present in each of the leads, there is no available state within the lead for the edge states with the opposite spin to occupy. Hence, the edge state with the opposite spin is extended from bottom edge to the top edge. We describe this case as a set of boundary conditions that links the distribution functions of the top and bottom edges as:

$$\begin{aligned}f^{\text{bot}}_{\uparrow}(x = L/2) &= f^{\text{top}}_{\uparrow}(x = L/2) \\ f^{\text{bot}}_{\downarrow}(x = -L/2) &= f^{\text{top}}_{\downarrow}(x = -L/2)\end{aligned} \tag{F.6}$$

Using Eq. (F.6), we expand in gradients of the distribution functions at the top edge as:

$$f^{\text{top}}_{\uparrow,\downarrow}(x) = f^{\text{bot}}_{\uparrow,\downarrow}(\pm L/2) + \Gamma^{top}[f^{\text{bot}}_{\uparrow}(L/2), f^{\text{bot}}_{\downarrow}(-L/2)]\,(x \mp L/2). \tag{F.7}$$

We obtain the total current by integrating the difference of the distribution functions of right and left movers over energy:

$$I_{tot} = \frac{e}{h}\int d\epsilon \left[f^{\text{top}}_{\downarrow} + f^{\text{bot}}_{\uparrow} - f^{\text{bot}}_{\downarrow} - f^{\text{top}}_{\uparrow}\right]. \tag{F.8}$$

Using Eq. (F.3) and Eq. (F.7), we rewrite the equation above as:

$$\begin{aligned}I_{tot} &= \frac{e}{h}\int d\epsilon \left[\Gamma^{\text{top}}[f^{\text{bot}}_{\uparrow}(L/2), f^{\text{bot}}_{\downarrow}(-L/2)] - \Gamma^{\text{bot}}[f^0_L, f^0_R]\right] L \\ &= e\big(N^{\text{top}}\frac{dm^{\text{top}}}{dt} + N^{\text{bot}}\frac{dm^{\text{bot}}}{dt}\big).\end{aligned} \tag{F.9}$$

We see that the current through the system is only possible via nuclear spin flips. We now

rewrite Eq. (F.9) using the definitions of distribution functions and obtain:

$$\begin{aligned} I_{tot} = & \frac{e^2V}{h}\left(\frac{\xi^{\text{top}}}{2} + \frac{\xi^{\text{bot}}(1-\xi^{\text{top}})}{2}\right) \\ & - \frac{e^2V}{h}\coth\left(\frac{eV}{2k_BT}\right)\left(\frac{m^{\text{top}}\xi^{top}}{2} + \frac{m^{\text{bot}}\xi^{\text{bot}}(1-\xi^{\text{top}})}{2}\right) \\ & - \frac{e}{h}2m^{\text{top}}\xi^{\text{top}}\int d\epsilon\big(f_L^0 - f_R^0\big)\Gamma^{\text{bot}}L, \end{aligned} \tag{F.10}$$

where $\xi^{\text{bot(top)}} \equiv 2\pi N^{\text{bot(top)}}\gamma_0$. The form of Eq. (F.10) suggests that one can tailor the number of nuclear spins for both edges (i.e. $\xi^{\text{bot(top)}}$) to get the desired current characteristics. For the rest of the calculation, we omit the last term in Eq. (F.10) (valid in the limit of low bias or small $\xi^{\text{bot}}\xi^{\text{top}}$) and carry on to calculate the power:

$$\begin{aligned} P_{tot} = & \frac{e^2V^2}{h}\left(\frac{\xi^{\text{top}}}{2} + \frac{\xi^{\text{bot}}(1-\xi^{\text{top}})}{2}\right) \\ & - \frac{e^2V^2}{h}\coth\left(\frac{eV}{2k_BT}\right)\left(m^{\text{top}}\xi^{\text{top}} + m^{\text{bot}}\xi^{\text{bot}}(1-\xi^{\text{top}})\right), \end{aligned} \tag{F.11}$$

We assume that the overall interaction strength of the top edge is much smaller than the bottom edge edge ($\xi^{\text{top}} \ll \xi^{\text{bot}}$), hence we obtain the total power as:

$$P_{tot} = \frac{e^2V^2}{h}\xi\left[\frac{1}{2} - \coth\left(\frac{eV}{2k_BT}\right)m\right], \tag{F.12}$$

where we drop the bot superscripts for the sake of clarity. We now use the mean polarization dynamics formula [1]:

$$m(t) = (m_0 - \bar{m})e^{-t/\tau_m} + \bar{m}, \tag{F.13}$$

where $\bar{m} = \frac{1}{2}\tanh\left(\frac{eV}{2k_BT}\right)$ is the target mean polarization and $\tau_m = \hbar\tanh\left(\frac{eV}{2k_BT}\right)(\gamma_0 eV)^{-1}$ is the characteristic time scale for mean polarization dynamics. We insert Eq. (F.13) into Eq. (F.12) and obtain the total power:

$$P_{tot} = \frac{e^2V^2}{h}\xi\left[\frac{1}{2} - m_0\coth\left(\frac{eV}{2k_BT}\right)\right]e^{-t/\tau_m}. \tag{F.14}$$

Appendix G

CHARGING-DISCHARGING CYCLE OF THE CAPACITIVE QUANTUM INFORMATION ENGINE

Discharging Phase: We see from Eq. (F.14) that $P_{tot} \leq 0$ for $\frac{1}{2} - m_0 \coth\left(\frac{eV}{2k_BT}\right) \leq 0$. We now find the extracted work under constant voltage bias by integrating Eq. (F.14) over time:

$$\begin{aligned} W &= \int_0^\infty dt \frac{e^2V^2}{h}\xi\left[\frac{1}{2} - m_0 \coth\left(\frac{eV}{2k_BT}\right)\right]e^{-t/\tau_m} \\ &= \frac{eV}{2k_BT}\left(\tanh\left(\frac{eV}{2k_BT}\right) - 2m_0\right)Nk_BT \end{aligned} \tag{G.1}$$

If we now start from fully polarized nuclear spins ($m_0 = 0.5$), the maximum work can that can be extracted is found to be (by maximizing equation above with respect to applied voltage V):

$$W_{ext} \approx 0.4Nk_BT\ln(2),$$

for $eV \approx 1.28k_BT$. We calculate the mean target polarization for this voltage value and obtain $m(t >> \infty) = \frac{1}{2}\tanh(0.64) \approx 0.282$. This means that,using constant voltage bias, we can use approximately $\%40$ of the memory, we can extract work equivalent to $\%40$ of Landauer's bound. However, discharging phase usually involves a load connected to the battery. As we show in Chapter 4, with an appropriate choice of load resistance, we can extract work at the Landauer's limit.

Charging Phase: We now show how to erase the memory by applying a constant voltage bias and polarizing nuclear spins. We start from zero mean polarization, $m_0 = 0$, and polarize the nuclear spins up to $\kappa/2$, where κ is defined to be the fraction of nuclear spins we choose to polarize:

$$\frac{\kappa}{2} = \bar{m}(1 - e^{-\bar{t}/\tau_m}). \tag{G.2}$$

Here, $\bar{t} = -\tau_m \ln(1 - \kappa\coth(eV/2k_BT))$ is the time when we stop erasing the memory.

We obtain the heat dissipated by taking the integral of power over time:

$$\begin{aligned} W_C &= \int_0^{\bar{t}} dt \frac{e^2V^2}{h}\frac{\xi}{2}e^{-t/\tau_m} \\ &= \frac{eV}{2k_BT}\kappa N k_B T. \end{aligned} \tag{G.3}$$

We note that $0 \leq 1-\kappa/2\bar{m} < 1$ (see Eq. (G.2)). This condition gives us an lower bound on the applied voltage:

$$V \geq \frac{k_BT}{e}\ln\left(\frac{1+\kappa}{1-\kappa}\right). \tag{G.4}$$

Taking the lower bound value as the applied voltage bias, we obtain the minimum heat dissipated:

$$W_C = \frac{\kappa}{2}\ln\left(\frac{1+\kappa}{1-\kappa}\right)N k_B T. \tag{G.5}$$

Work Extraction via an External Load: We now calculate the power generated for an attached load with conductance G_L, which is simply

$$P = G_L V^2 = G_L\left[\frac{2k_BT}{e}\tanh^{-1}\big(\alpha m(t)\big)\right]^2. \tag{G.6}$$

where we used the induced voltage $V = \frac{2k_BT}{e}\tanh^{-1}\big(\alpha m(t)\big)$ with $\alpha = \zeta/(G_L/G_0 + \zeta/2)$. The extracted work by the capacitive quantum information engine is given as

$$W = \int dt G_L\left[\frac{2k_BT}{e}\tanh^{-1}\big(\alpha m(t)\big)\right]^2. \tag{G.7}$$

We now use change of variables to reexpress Eq. (G.7) and obtain

$$W = \int dm \frac{dt}{dm} G_L\left[\frac{2k_BT}{e}\tanh^{-1}\big(\alpha m(t)\big)\right]^2, \tag{G.8}$$

$$= \frac{G_L}{G_0}\frac{4k_BT}{2\pi\gamma_0}\frac{1}{\alpha-2}\int_{\alpha/2}^{0} dx \tanh^{-1}\big(x\big), \tag{G.9}$$

where in the last line, we use Eq. (4.1) and later defined $x = \alpha m(t)$ for convenience. We assume that initially all nuclear spins were polarized $m = 0.5$ and finally all nuclear spins depolarize as we deduce from Eq. (3.28) and set the boundary conditions accordingly. Finally, we take the integral in Eq. (G.8) and arrive at the work extracted for a given load conductance G_L as given in Eq. (4.9):

$$W = N\frac{G_L}{G_0}\frac{4k_BT}{\zeta}\frac{1}{2-\alpha}\left(\frac{1}{2}\ln\big(1-\frac{\alpha^2}{4}\big) + \frac{\alpha}{2}\tanh^{-1}\big(\frac{\alpha}{2}\big)\right). \tag{G.10}$$

Appendix H

3D TOPOLOGICAL INSULATOR ELECTRON SPIN AND NUCLEAR SPIN DYNAMICS

Charge-spin coupled dynamics of the 3D topological insulator surface states

In Chapter 5, we present the quantum kinetic equation for the surface states of a 3D topological insulator. In this appendix, we present the spin sector of the quantum kinetic equation. We start by performing the spin traces $\boldsymbol{\sigma}$ and obtain:

$$\begin{aligned}\partial_t g_x + v_F \nabla_y g_0 + 2 v_F k_F \hat{k}_x g_z = &-\frac{1}{\tau_0}\left[g_x - \langle g_x\rangle - \hat{k}_y \langle g_0\rangle\right] \\ &- \frac{3}{\tau_{sf}}\left[g_x + \frac{1}{3}\langle g_x\rangle + \frac{2}{3}\langle \boldsymbol{g}\rangle \cdot \boldsymbol{m} g_x - \frac{2}{3}\langle g_0\rangle g_0 m_x + \frac{2}{3} m_x - \hat{k}_y \langle g_0\rangle\right],\end{aligned} \tag{H.1}$$

whereas the σ_y trace yields:

$$\begin{aligned}\partial_t g_y - v_F \nabla_x g_0 + 2 v_F k_F \hat{k}_y g_z = &-\frac{1}{\tau_0}\left[g_y - \langle g_y\rangle + \hat{k}_x \langle g_0\rangle\right] \\ &- \frac{3}{\tau_{sf}}\left[g_y + \frac{1}{3}\langle g_y\rangle + \frac{2}{3}\langle \boldsymbol{g}\rangle \cdot \boldsymbol{m} g_y - \frac{2}{3}\langle g_0\rangle g_0 m_y + \frac{2}{3} m_y + \hat{k}_x \langle g_0\rangle\right],\end{aligned} \tag{H.2}$$

and finally σ_z trace:

$$\begin{aligned}\partial_t g_z + 2 v_F k_F \left(\hat{k}_x g_x + \hat{k}_y g_y\right) = &-\frac{1}{\tau_0}\left[g_z - \langle g_z\rangle\right] \\ &- \frac{3}{\tau_{sf}}\left[g_z + \frac{1}{3}\langle g_z\rangle + \frac{2}{3}\langle \boldsymbol{g}\rangle \cdot \boldsymbol{m} g_z - \frac{2}{3}\langle g_0\rangle g_0 m_z + \frac{2}{3} m_z\right].\end{aligned} \tag{H.3}$$

Next, we assume that the quasiclassical Green's function is diagonal in the eigenstates of the 3D topological insulator Hamiltonian and insert the ansatz given in Eq. (5.40) and

Eq. (5.42) and obtain the spin sector for the quantum kinetic equation:

$$\partial_t\langle\hat{k}_y g_0\rangle + \frac{v_F}{2}\nabla_y\langle g_0\rangle + \frac{\langle\hat{k}_y g_0\rangle}{2\tau_0} = \\ -\frac{3}{\tau_{sf}}\left(\frac{4}{3}\langle\hat{k}_y g_0\rangle + \frac{2}{3}\left(\langle\hat{k}_y g_0\rangle\boldsymbol{m}\cdot\langle(\hat{k}\times\hat{z})g_0\rangle\right)\rangle - \frac{2}{3}\langle g_0\rangle^2 m_x + \frac{2}{3}m_x\right), \tag{H.4}$$

and

$$\partial_t\langle\hat{k}_x g_0\rangle + \frac{v_F}{2}\nabla_x\langle g_0\rangle + \frac{\langle\hat{k}_x g_0\rangle}{2\tau_0} = \\ -\frac{3}{\tau_{sf}}\left(\frac{4}{3}\langle\hat{k}_x g_0\rangle - \frac{2}{3}\left(\langle\hat{k}_x g_0\rangle\boldsymbol{m}\cdot\langle(\hat{k}\times\hat{z})g_0\rangle\right)\rangle + \frac{2}{3}\langle g_0\rangle^2 m_y - \frac{2}{3}m_y\right). \tag{H.5}$$

Here, we keep the discussion to the kinetic equation for the in-plane electron spin polarization only.

Nuclear spin polarization dynamics

In this section, we obtain the nuclear spin dynamics using the nonequilibrium Green's function method. We first obtain the self energy for the nuclear spin correlators as follows:

$$\Pi^{-+}_{\alpha\beta}(\boldsymbol{q},\Omega) = -i\frac{\lambda^2}{4}\int\frac{d^2\boldsymbol{k}}{(2\pi)^2}\int\frac{d\omega}{2\pi}\,\mathrm{Tr}\left[\sigma_\alpha G^{-+}(\boldsymbol{k},\omega)\sigma_\beta G^{+-}(\boldsymbol{k}-\boldsymbol{q},\omega-\Omega)\right]. \tag{H.6}$$

We then parametrize the electronic Green's function, namely $G \equiv G_\mu\sigma_\mu$ with $\mu = \{0,x,y,z\}$ and obtain:

$$\begin{aligned}\Pi^{-+}_{\alpha\beta} &= -i\frac{\lambda^2}{4}\,\mathrm{Tr}\left[\sigma_\alpha\sigma_\gamma\sigma_\beta\sigma_\mu\right]\int\frac{d^2\boldsymbol{k}}{(2\pi)^2}\int\frac{d\omega}{2\pi}G^{-+}_\mu G^{+-}_\gamma, \\ &= -i\frac{\lambda^2}{2}\int\frac{d^2\boldsymbol{k}}{(2\pi)^2}\int\frac{d\omega}{2\pi}\Big(\delta_{\alpha\beta}G^{-+}_0G^{+-}_0 + i\epsilon_{\alpha\beta\mu}\left(G^{-+}_\mu G^{+-}_0 - G^{-+}_0G^{+-}_\mu\right) \\ &\quad + G^{-+}_\beta G^{+-}_\alpha - \delta_{\alpha\beta}G^{-+}_\gamma G^{+-}_\gamma + G^{-+}_\alpha G^{+-}_\beta\Big),\end{aligned} \tag{H.7}$$

where we discard the momentum-energy variables $(\boldsymbol{q},\Omega)$ for clarity. Similarly, the greater component of the self energy is found to be:

$$\begin{aligned}\Pi^{+-}_{\alpha\beta} &= -i\frac{\lambda^2}{4}\,\mathrm{Tr}\left[\sigma_\alpha\sigma_\gamma\sigma_\beta\sigma_\mu\right]\int\frac{d^2\boldsymbol{k}}{(2\pi)^2}\int\frac{d\omega}{2\pi}G^{+-}_\mu G^{-+}_\gamma, \\ &= -i\frac{\lambda^2}{2}\int\frac{d^2\boldsymbol{k}}{(2\pi)^2}\int\frac{d\omega}{2\pi}\Big(\delta_{\alpha\beta}G^{+-}_0G^{-+}_0 + i\epsilon_{\alpha\beta\mu}\left(G^{+-}_\mu G^{-+}_0 - G^{+-}_0G^{-+}_\mu\right) \\ &\quad + G^{+-}_\beta G^{-+}_\alpha - \delta_{\alpha\beta}G^{+-}_\gamma G^{-+}_\gamma + G^{+-}_\alpha G^{-+}_\beta\Big).\end{aligned} \tag{H.8}$$

We can evaluate the nuclear spin self energy by associating the lesser and greater Green's functions in the nuclear spin self energy with the distribution functions of the electrons. Similar to the electron spin dynamics, we make use of the generalized distribution matrix $F = \frac{n}{2}\sigma_0 + \boldsymbol{s}\cdot\boldsymbol{\sigma}$. As an example, we focus on the first term in the integrand of Eq. (H.7), where we have:

$$\begin{aligned}&\int \frac{d^2\boldsymbol{k}}{(2\pi)^2}\int \frac{d\omega}{2\pi} n(\boldsymbol{k})(1-n(\boldsymbol{k}-\boldsymbol{q}))\delta(\omega-\hbar v_F k+\mu)\delta(\omega-\Omega-\hbar v_F|\boldsymbol{k}-\boldsymbol{q}|+E_F)\\ &=\int \frac{d^2\boldsymbol{k}}{(2\pi)^2} n(\boldsymbol{k})(1-n(\boldsymbol{k}-\boldsymbol{q}))\delta(\hbar v_F k-\Omega-\hbar v_F|\boldsymbol{k}-\boldsymbol{q}|),\end{aligned} \tag{H.9}$$

where the delta function ensures the energy conservation due to scattering. We note that other terms in the integrand of Eq. (H.7) can be obtained in a similar fashion.

After obtaining the nuclear spin self energy, we now focus on the nuclear spin dynamics. In order to describe the dynamics of the nuclear spins, we first write down the kinetic equation for the lesser component of the nuclear spin correlators in the Wigner representation:

$$\dot{D}^{-+}_{\alpha\beta}(\boldsymbol{q},\Omega) = -\frac{i}{\hbar}\Big[\Pi^{-+}_{\alpha\delta}(\boldsymbol{q},\Omega)D^{+-}_{\delta\beta}(\boldsymbol{q},\Omega) - D^{-+}_{\alpha\delta}(\boldsymbol{q},\Omega)\Pi^{+-}_{\delta\beta}(\boldsymbol{q},\Omega)\Big], \tag{H.10}$$

where we discard the position and time variables for clarity.

As Eq. (H.10) is given in the Wigner representation, we need to integrate it over momentum $\boldsymbol{q}$ and energy Ω in order to obtain the dynamics of the nuclear spins. In order to achieve this, we need to consider the equal time density matrix, which corresponds to integrating the overall quantum kinetic equation for the nuclear spins over Ω, which allows us to set $\Omega = 0$ for the equation above. In that case, we have:

$$\int \frac{d^2\boldsymbol{q}}{(2\pi)^2}\,\dot{D}^{-+}_{\alpha\beta}(\boldsymbol{q},0) = -\frac{i}{\hbar}\int \frac{d^2\boldsymbol{q}}{(2\pi)^2}\Big[\Pi^{-+}_{\alpha\delta}(\boldsymbol{q},0)D^{+-}_{\delta\beta}(\boldsymbol{q},0) - D^{-+}_{\alpha\delta}(\boldsymbol{q},0)\Pi^{+-}_{\delta\beta}(\boldsymbol{q},0)\Big]. \tag{H.11}$$

We then assume that there exists only on-site correlations between the nuclear spin, the momentum dependence of the nuclear spin correlators can be ignored. We define $d^{-+}_{\alpha\beta} \equiv \int \frac{d^2\boldsymbol{q}}{(2\pi)^2} D^{-+}_{\alpha\beta}(\boldsymbol{q},0)$ and approximate the right hand side of Eq. (H.11) as:

$$\int \frac{d^2\boldsymbol{q}}{(2\pi)^2}\Big[\Pi^{-+}_{\alpha\delta}(\boldsymbol{q})D^{+-}_{\delta\beta}(\boldsymbol{q}) - D^{-+}_{\alpha\delta}(\boldsymbol{q})\Pi^{+-}_{\delta\beta}(\boldsymbol{q})\Big] \approx \left(\pi^{-+}_{\alpha\delta}d^{+-}_{\delta\beta} - d^{-+}_{\alpha\delta}\pi^{+-}_{\delta\beta}\right) \tag{H.12}$$

where we define $\int \frac{d^2\boldsymbol{q}}{2(\pi)^2}\,\Pi^{-+}_{\alpha\delta}(\boldsymbol{q},0) \equiv \pi^{-+}_{\alpha\delta}$. In this case, we obtain:

$$\dot{d}^{-+}_{\alpha\beta}(\boldsymbol{r},t) = -\frac{i}{\hbar}\left(\pi^{-+}_{\alpha\delta}d^{+-}_{\delta\beta}(\boldsymbol{r},t) - d^{-+}_{\alpha\delta}(\boldsymbol{r},t)\pi^{+-}_{\delta\beta}\right), \tag{H.13}$$

as also given in Eq. (5.53). We note the self energy obeys the following relation, $\pi^{-+}_{\alpha\beta} = \pi^{+-}_{\beta\alpha}$. This proves that the kinetic equation (Eq. (5.53)) for all the diagonal components of the nuclear spins correlators is trivial, $\dot{d}_{\alpha\alpha} = 0$, as expected.

Owing to the assumption we use, we only need to integrate the nuclear spin self energy over the momentum. We again exemplify this for the first term in the self energy and integrate Eq. (H.9) over momentum $\boldsymbol{q}$ and we have:

$$
\begin{aligned}
&= \int \frac{dk}{2\pi} 2k^2 \int_0^{2\pi} \frac{d\theta_k}{2\pi} \int_{-\pi/2+\theta_k}^{\pi/2+\theta_k} \frac{d\theta_q}{2\pi} \cos(\theta_k - \theta_q) n(k, \theta_k)(1 - n(k, \theta_k - \theta_q)), \\
&= \int \frac{dk}{2\pi} 2k^2 \int_0^{2\pi} \frac{d\theta_k}{2\pi} n(k, \theta_k) \left[\frac{1}{\pi} - \int_{-\pi/2+\theta_k}^{\pi/2+\theta_k} \frac{d\theta_q}{2\pi} \cos(\theta_k - \theta_q) n(k, \theta_k - \theta_q)) \right] \\
&\approx \frac{2}{\pi} \int \frac{dk}{2\pi} k^2 \int_0^{2\pi} \frac{d\theta_k}{2\pi} n(k, \theta_k) \left(1 - \langle n(k) \rangle\right) \\
&\approx \frac{2}{\pi} \int \frac{dk}{2\pi} k^2 \langle n(k) \rangle \left(1 - \langle n(k) \rangle\right). \qquad \text{(H.14)}
\end{aligned}
$$

where $q = |\boldsymbol{q}|$ and $k = |\boldsymbol{k}|$. We note that we use the condition $q = 2k\cos(\theta_k - \theta_q)$ due to the energy conservation. The remaining terms in the nuclear spin self energy can be evaluated similarly.

Appendix I

NUMERICAL TIGHT-BINDING SIMULATIONS FOR THE MAJORANA BILLIARDS

In order to demonstrate our analytical results in Secs. 7.2.1 and 7.2.2 for average density of fermion parity crossings, we perform tight-binding simulations of fermion parity crossings in a p-wave and s-wave Majorana billiards using the Kwant toolbox for quantum transport [186].

For the p-wave numerical results, we start with the left hand side of Eq. (7.5), which is a non-Hermitian operator, as opposed to the p-wave Hamiltonian in Eq. (6.1). This non-Hermitian operator and the p-wave Hamiltonian in Eq. (6.1) are equivalent in the sense that no approximation was made in going from Eq. (6.1) to Eq. (7.5). We convert this non-Hermitian operator to its tight-binding form, which satisfies $\hat{O}^{\mathrm{PW}}_{\mathrm{TB}}\chi = \mu\chi$, using conventional methods (see, for example, Ref. [187]):

$$\begin{aligned}\hat{O}^{\mathrm{PW}}_{\mathrm{TB}} = &\big(2dt + V(x,y)\big)\,\tau_0\,|x,y\rangle\langle x,y| \\ &- t\tau_0\big[\,|x+a,y\rangle\langle x,y| + |x,y+a\rangle\langle x,y| + \mathrm{h.c.}\big] \\ &+ i\Delta'\Big[\frac{i}{2}\tau_y\,|x+a,y\rangle\langle x,y| \\ &\quad - \frac{i}{2}\tau_x\,|x,y+a\rangle\langle x,y| + \mathrm{h.c.}\Big],\end{aligned} \tag{I.1}$$

where $t = \hbar^2/2ma^2$ is the hopping parameter, a is the lattice constant for the tight-binding lattice and $V(x,y)$ is the onsite potential. For disordered systems, we take the disorder to be Gaussian, i.e. $\langle V(\mathbf{r})V(\mathbf{r}')\rangle = D\delta(\mathbf{r}-\mathbf{r}')$ for $\mathbf{r},\mathbf{r}'$ within the system, where $\langle\ldots\rangle$ represents averaging over disorder realizations, $D \equiv V_d^2 a^d$ with V_d being the disorder strength and d is the dimension of the system. (In most of our paper, $d = 2$; if $d = 1$, then the hoppings in the y direction are absent). In tight-binding simulations, this corresponds to choosing randomly the on-site potential from a Gaussian distribution. For ballistic cavity results, we set $V(x,y) = 0$ within the cavity. The boundaries of the system are defined by the lack of hopping to outside. We form the tight-binding sparse matrix of this

operator using the Kwant library [186] over the system shape described in Fig. 7.1 and the relevant plots. We then numerically obtain the eigenvalues of this (non-Hermitian) sparse matrix using LAPACK libraries present in the SciPy package [188]. We finally discard nonreal eigenvalues to obtain our results.

For the *s*-wave results, we go through the same procedure, except for utilizing the appropriate tight-binding-representation of the non-Hermitian operator derived from the Hamiltonian in Eq. (6.2). For $E = 0$, the tight-binding model for the *s*-wave equivalent of Eq. (7.5) reads $\hat{O}^{\mathrm{SW}}_{\mathrm{TB}}\chi = \mu\chi$, with the non-Hermitian operator $\hat{O}^{\mathrm{SW}}_{\mathrm{TB}}$ defined as:

$$\begin{aligned}\hat{O}^{\mathrm{SW}}_{\mathrm{TB}} = &\big[\big(2dt + V(x,y)\big)\,\sigma_0\tau_0 + B\,\sigma_x\tau_z\big]\ |x,y\rangle\langle x,y| \\ &- t\sigma_0\tau_0\big[\,|x+a,y\rangle\langle x,y| + |x,y+a\rangle\langle x,y| + \mathrm{h.c.}\big] \\ &- \sigma_y\tau_0\,\big[\frac{i\alpha}{2}\ |x+a,y\rangle\langle x,y| + \mathrm{h.c.}\big] \\ &+ \sigma_x\tau_0\,\big[\frac{i\alpha}{2}\ |x,y+a\rangle\langle x,y| + \mathrm{h.c.}\big] \\ &+ i\Delta\sigma_0\tau_y\,|x,y\rangle\langle x,y|\,. \end{aligned} \tag{I.2}$$

Again, in the plots where $d = 1$, the hoppings in the y direction are absent.

For disorder averaging, we create many realizations of the same disordered system and do statistics over the combined results of each realization. For shape averaging over chaotic cavities, we create many realizations of the same chaotic cavity, the difference between realizations being the positioning of a relevant geometrical feature of the cavity, without changing the size of the system volume or boundary. For the Lorentz cavity, for example, we slightly change the position of the central stopper for each realization (making sure the stopper never comes too close to a wall). We check that the change is large enough numerically to yield a completely different set of eigenvalues.

Appendix J

OSCILLATORY BEHAVIOR OF THE DENSITY OF FERMION PARITY CROSSINGS IN A DISK MAJORANA BILLIARD

In this appendix, we demonstrate the trace formula for ρ_{osc} [see Eq. (7.3)] for a p-wave disk Majorana billiard of radius R. As opposed to the calculation in Chapter 7, here we compare the trace formula to tight-binding simulations.

We note that the oscillatory part $\rho_{\text{osc}}(E)$ of the density of states $\rho(E)$ for a two dimensional disk billiard of radius R with quadratic dispersion is given by [158]:

$$\rho_{\text{osc}}(E) = \frac{1}{E_0}\sqrt{\frac{\hbar}{\pi p R}}\sum_{w=1}^{\infty}\sum_{v=2w}^{\infty} f_{vw}\frac{\sin^{3/2}(\varphi_{vw})}{\sqrt{v}} \times \operatorname{Im}\big[\exp\{i(S_{vw}/\hbar - 3v\pi/2 + 3\pi/4)\}\big], \tag{J.1}$$

with

$$f_{vw} = \begin{cases} 1 & \text{if } v = 2w \\ 2 & \text{if } v > 2w \end{cases} \tag{J.2}$$

and $E_0 \equiv \hbar^2/(2mR^2)$. For a quadratic Hamiltonian, $S_{vw} = p\,L_{vw}$ is the classical action of the orbit with $L_{vw} = 2vR\sin(\varphi_{vw})$ being the classical orbit length of 2D disk, $\varphi_{vw} \equiv \pi w/v$ is half of the polar angle and p is the momentum of the particle. As before, v, w are two integers that correspond to the number of vertices and windings of the classical periodic orbit, respectively.

However the tight binding dispersion breaks the rotational symmetry of the problem weakly. The orbits that belong to the families that have the same action for a quadratic dispersion have slightly different actions for the tight binding dispersion. This type of symmetry breaking can then be treated by the semiclassical perturbation theory as discussed in Ref. [158] (see p. 272). This would involve averaging the variation of the phases over

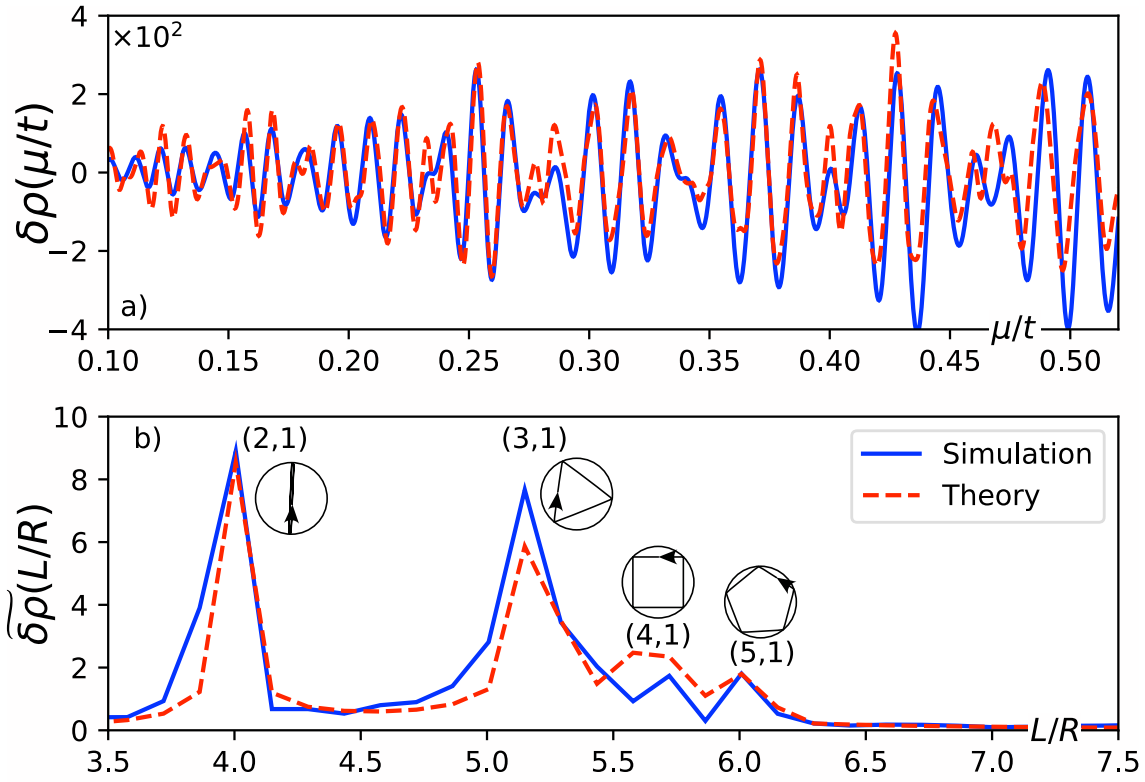

Figure J.1: (a) Density oscillations of fermion parity crossings ρ_{osc} for a clean p-wave disk Majorana billiard on a lattice with $R = 100a$, $\Delta' = 0.001ta$. (b) The Fourier transform of ρ_{osc}. The (v, w) pairs and corresponding classical orbits for the peaks are labeled. The smoothing parameter for both figures is $\gamma = 0.4/R$.

all the orientations of the orbits, resulting in an effective dispersion $E_{\text{eff}}(p)$ of a fictitious rotationally invariant problem. We find that the (one dimensional tight-binding–like) dispersion $E_{\text{eff}} = 2t\,(1 - \cos\,(pa/\hbar))$ produces a very good fit to the numerical simulations. We thus obtain the expression for momentum $p(\mu)$:

$$p(\mu) = \frac{\hbar}{a} \arccos\left(1 - \frac{\mu}{2t}\right). \tag{J.3}$$

The deviations from the quadratic dispersion lead to a correction $S_{vw} \to S_{vw} + \Delta S_{vw}$ in the action:

$$\Delta S_{vw} = \frac{\hbar}{a} \tan\left(\frac{p(\mu)a}{2\hbar}\right) L_{vw}. \tag{J.4}$$

We now obtain the oscillatory part of the density of fermion parity crossings corrected for tight-binding dispersion:

$$\begin{aligned}\rho_{\text{osc}}(\mu) = \frac{1}{E_0}\left(\frac{\hbar}{\pi R\, p(\mu)}\right)^{1/2} \sum_{w=1}^{\infty}\sum_{v=2w}^{\infty} f_{vw} \frac{\sin^{3/2}(\varphi_{vw})}{\sqrt{v}} \\ \times \operatorname{Im}\Bigg[\exp\Bigg\{iL_{vw} \\ \times \left(\frac{p(\mu+i\gamma)}{\hbar} - \frac{1}{a}\tan\frac{p(\mu+i\gamma)\,a}{2\hbar}\right)\end{aligned}$$

$$+ i\big(-3v\pi/2 + 3\pi/4\big)\Big\}\Big]. \tag{J.5}$$

Here, we combined Eq. (J.1), (J.3) and (J.4) at $\mu \to \mu + i\gamma$, with γ being the smoothing parameter.

The numerical results for ρ_{osc} and $\widetilde{\rho}_{\text{osc}}$ plotted in Fig. J.1 is obtained by solving a tight-binding p-wave system shaped as a disk using the Kwant toolbox as described in Appendix I. We then obtain ρ_{osc} as

$$\rho_{\text{osc}}(\mu/t) = \rho_\gamma(\mu/t) - \rho_{\text{w}}(\mu/t), \tag{J.6}$$

where ρ_{w} corresponds to the volume and surface terms of the Weyl expansion in Eq. (7.8) and ρ_γ is the smoothed density of fermion parity crossings

$$\rho_\gamma(\mu/t) = \int d\mu' \sum_{\mu_c} \delta(\mu' - \mu_c)\, F\left(\frac{\mu - \mu'}{\gamma}\right), \tag{J.7}$$

$F\big(\frac{\mu-\mu'}{\gamma}\big)$ is the Gaussian smoothing function with smoothing width γ. We then take the Fourier transform of $\rho_{\text{osc}}(k(\mu/t)\, a) \xrightarrow{\text{FT}} \widetilde{\rho}_{\text{osc}}(L/R)$ to identify the peaks corresponding to the lowest length L and the highest symmetry semiclassical periodic orbits [158] and plot the results in Fig. J.1b. We find good agreement with our analytical results.